The International Journal of Materials and Engineering Technology (TIJMET) (2023) 6(2)
http://dergipark.gov.tr/tijmet
ISSN: 2667-4033

RESEARCH ARTICLE

Optimization of the effects of process parameters on the tensile strength of developed aluminium roofing sheets using Taguchi method

Dickson David Olodu[*1] and Andrew Erameh[2]

[1]*Benson Idahosa University, Faculty of Engineering, Department of Mechanical Engineering, Benin City, Edo State, Nigeria*
[2]*Igbinedion University, Faculty of Engineering, Department of Mechanical Engineering, Edo State, Nigeria*

Article Info

Article history:
Received 07.05.2023
Revised: 14.06.2023
Accepted: 30.06.2023
Published Online: 30.09.2023

Keywords:
Aluminum roofing sheets
Design of experiments
Orthogonal array
S/N ratio
Taguchi method

Abstract

This study employed the Taguchi Method to optimize the impact of process factors on the tensile strength of newly designed aluminum roofing sheets. The Taguchi Method which is a statistical approach was utilized to improve the manufacturing quality of aluminum roofing sheets. The performance characteristics of process factors on the tensile strength of the generated aluminium roofing sheets were investigated using an orthogonal array, a signal-to-noise ratio, and an analysis of variance. Four variables such as production temperature, production pressure, cooling time, and the percentage of chromium in the aluminum roofing sheet were taken into account in this analysis. An appropriate orthogonal array was chosen, and tests were run. The process parameters were assessed following the experimentation, and the signal-to-noise ratio (S/N ratio) was computed. The best parameter values were found with the use of graphs, and confirmation trials were run to ascertain the adequacy of the tensile strength of the aluminum roofing sheets produced. The outcome demonstrated that a production temperature of 1610°C, a production pressure of 79 GPa, a cooling time of 85 seconds, and a chromium content of 2.0% gave an aluminum roofing sheet its optimum tensile strength of 592 MPa. The manufacturing temperature, followed by cooling time and the percentage of chromium, was shown to have the most significant impact on the tensile strength of aluminum roofing sheets. The least effective component was determined to be production pressure. Moreover, the metallographic examination of the grain refined aluminum alloy showed a lower level of porosity defect and higher tensile strength compared with the unrefined alloy (pure aluminum). Also, the refined alloy shows lower aquiaxed structure compared with the unrefined alloy (pure aluminum).

1. Introduction

The microstructure of commercial-pure aluminum (LXX Series), which contains more than 99% aluminium is mostly made up of pure aluminum FCC matrix. The non-metallic inclusions, which are caused by the presence of iron and silicon impurities, are the other current phases. Unalloyed aluminum can be strengthened by cold working but cannot be heat treated. Due to the face-centered cubic (FCC) crystal structure of aluminum and its alloys, they have outstanding formability characteristics, with the exception of the restriction caused by the level and kind of alloying. Some aluminum alloys can be heat-treated to a greater degree of strength than many structural steels [1]. The metal possesses a pleasing surface finish, good thermal and electrical conductivity, good reflectivity, and low density [1, 2]. These alloys are the main structural materials in the aircraft industry as a result of this last characteristic, which, when combined with the high strengths available, results in high strength-to-weight ratios. Aluminum's stiffness (elastic modulus) is only roughly one-third that of steel; therefore, this fact must be taken into account when designing components to avoid excessively significant deflections in use [3-5].

Moreover, grain refinement is the act of controlling the solidification process to produce more (and subsequently smaller) grains as well as grains of a particular shape. The phrase "refinement" typically refers to the addition of chemicals to the metal, but it can also refer to the regulation of cooling speed. Any substance added to a liquid metal to produce a finer grain size in the ensuing casting is known as a grain refiner [6]. AL-6Ti, AL-5Ti-l B, and AL-5Ti-1C are the master alloy additions for aluminum alloys that are most readily available [7]. The composition of the alloy, the pace of solidification, and the addition of grain refiners containing intermetallic phase particles serves as sites for heterogeneous grain nucleation which affect the type and size of grains that are produced. In order to increase casting soundness, a finer grain size reduces shrinkage, hot cracking, and hydrogen porosity. The feeding qualities, mechanical properties, thermal treatment response, pressure tightness, appearance after chemical, Electro-chemical, mechanical finishing, and higher wear resistance were all improved by grain refinement [8, 9, 10]. Adding particles to the melt that form new crystals during solidification is the most effective way to adjust grain size. In addition, the kind and weight percentage of grain refining additives have an impact on the grain size and tensile strength of aluminum alloys. TiB_2, Fe, and Cr can be used for refinement of aluminium.

Aluminum and composite materials are widely employed in a variety of industry sectors, including aerospace, automotive, and marine. Due to their frequent use,

Corresponding Author: Dickson David OLODU
E-mail: dolodu@biu.edu.ng

Olodu, D.D., and Erameh, A., Optimization of the Effects of Process Parameters on the Tensile Strength of Developed Aluminium Roofing Sheets Using Taguchi Method, The International Journal of Materials and Engineering Technology (TIJMET), 2023, 6(2): 31-40

experimental research is needed to develop these materials' strength and repair capabilities [11]. These materials need to be created through expensive and time-consuming experimental research. As a result, interest in numerical analysis has increased [11]. The main draw of numerical analysis is how closely it resembles experimental findings [11]. A statistical approach called the Taguchi method was developed by Taguchi and Konishi [12]. Initially, it was established to improve the quality of manufactured items (development of production processes), but later its application was extended to many other engineering disciplines, such as biotechnology [13]. The invention of the analysis of variance method was one of Taguchi's achievements that was particularly valued by statisticians in the field. To successfully obtain the desired outcomes, precise process parameter selection and their separation into control and noise components are essential [12, 14]. In this design of experiment, the control is selected in such a way as to eliminate the influence of the sound source in order to achieve the best process results. Taguchi's method involves determining the appropriate control parameters which entails that a number of orthogonal network (OA) tests is performed [15]. Data analysis and component quality prediction methods use the results of these studies [16]. Foster [7] looked into how five input characteristics affected the refined goods' surface quality. The input parameters were mold temperature, melting temperature, packing pressure, packing duration and injection time. To reduce the shrinkage of polypropylene (PP) and polystyrene (PS), the Taguchi process was used. In addition, he also used neural networks to simulate the process and reduced PP and PS by 0.937% and 1.224% respectively. Vaatanen et al. [18, 19] used the Taguchi method to analyze the effect of injection molding parameters on the aesthetic quality of cast parts; weight, welding, and kiln marks were three other quality attributes targeted for reduction. With very little experience, they are able to optimize various quality features that can lead to cost savings.

The discovery of new materials through research and design is the driving force behind economic development [20]. That is, modern technology is highly dependent on material research, which contributes to the progress of the economy of each country. Kok [21] studied the mechanical properties of vortex produced composites of 2024 aluminum alloy enriched with Al_2O_3 particles. The hardness and toughness of MMC A359/Al_2O_3 increased with rising temperature, according to Kumar et al. [22]. In addition, their research showed that the use of electromagnetic agitation during production leads to smaller particles and better adhesion from the interface of the particles to the matrix. Al/SiC composites produced by powder metallurgy were studied by Venkatesh and Harish [23] to obtain the required properties and improve the mechanical properties of aluminum. Nie and Chelman [24] and Friends [25] reported that aluminum strength, fatigue strength, modulus, wear resistance and creep are improved by reinforcement. Yao et al., [26] reported the study of aluminum trimodal metal matrix and the parameters affecting their strength; Tensile strength, which is significant in many applications, is the most useful and commonly referenced assessment of these characteristics [26]. For composites reinforced with TiB_2 particles, Saravanan et al. [27] found a 30% increase in stiffness and almost a doubling of tensile strength compared to the base aluminum alloy. The impact of mixing duration and speed on particle dispersion in SiCAMC was studied by Prabu et al. [28]. Nie et al. [24] reported that the aluminum material's strength, durability, and stability all declined. Early processing observations showed that porosity and an unequal distribution of reinforcement in the form of groups or clusters of reinforcement persisted [24]. Additionally, for a particular matrix alloy, decreasing the volume fraction reduces the break duration [20, 22]. Joardar et al. [29] analysed the deformation behavior of solid aluminum matrix cylinders under dry conditions. According to Romanova et al. [30], technical parameters such as the aspect ratio (ratio of height and diameter) of the specimens and the test temperature have a significant effect on the compressive strength and performance of aluminum. According to Domnita et al.'s [31] investigation into the effects of reinforcing particle shape and interface strength on the deformation and fracture behavior of an Al/Al_2O_3 composite, two pathways for particle failure are cracking and separation at the interface. Adin and şcan [32, 33] used the Taguchi approach to optimize the process parameters of medium-carbon steel joints connected by MIG welding. According to their findings, groove angle was shown to be the characteristic that had the greatest impact on both average tensile strength and elongation. For a particular 6061-T6 Al alloy, Yildiz [34] investigates the relationships between the Charpy V-notch test and fracture toughness. To ascertain the deformation behavior of the investigated alloys, tensile tests were used. Additionally, Charpy V-notch experiments were conducted to measure absorbed energy under mild impact conditions; the results of these tests are consistent with prior literature. A numerical analysis of the fatigue behavior of unpatched and patched aluminum and composite plates is conducted by Hamit et al. [11]. They used mathematics to investigate the fatigue behavior of composite patched and unpatched Al 5083 aluminum plates. The numerical research used the Finite Element Method. The Ansys version 15.0 Workbench Package application was used to perform numerical analyses for this work. The "V" notched and patched specimens with a 30° angle show the highest fatigue life (1593.2 N), respectively.

The goal of this study was to employ the Taguchi Method to optimize the impacts of process factors on the tensile strength of newly created aluminum roofing sheets. Before choosing this aluminum alloy, the 5052 aluminum alloy's durability and adaptability in applications were taken into account.

2. Materials and methods

2.1 Materials

The strongest non-heat-treated sheet and plate in widespread use, aluminum 5052 alloy sheet, was used in this study. It is one of the most useful alloys due to its versatility and excellent value. The Differential Aluminum Company in Benin City, Edo State, Nigeria, provided the aluminum 5052 sheet. In order to regulate the grain structure, limit grain growth, and avoid recrystallization following heat treatment in aluminum roofing sheets or aluminum-magnesium-zinc alloys, chromium (Cr) was added at different percentage to the aluminum. The percentage of Cr ratios used in this study were chosen and ranges from 0.5% to 3.0% respectively. The Chromium added was used to improve toughness and reduces susceptibility to stress corrosion. After cooling, the mechanical properties of these materials, which were created at different pressures and temperatures were evaluated. This material was exposed to a range of pressures and temperatures ranges from

40 GPa to 82 GPa and 670°C to 2400°C respectively during production.

Additionally, a 5025 aluminum alloy including chromium had its tensile strength evaluated. X-ray microanalysis and energy dispersive spectroscopy were used to evaluate the microstructure. The investigated specimens displayed complex phases based on the addition chromium. It was discovered that alloys with a larger quantity of chromium had fewer precipitation-hardening effects.

2.2. Measurement of temperature and pressure

A stationary non-contact infrared pyrometer was used to measure the temperature of aluminum alloys during the manufacturing process. This instrument has higher measurement accuracy than other temperature measuring instruments. It is applied in machine maintenance, process control and quality control. Infrared pyrometers can accurately measure in hazardous and hard-to reach areas that could pose a danger to workers. Infrared pyrometers with sensitivity of 88.7% (within ± 0.3 °C) can measure temperatures above 2500°C. In addition, a pressure sensor was also used to measure the pressure of the molten aluminum alloy during production. The equipment is integrated into the aluminum production plant.

2.3. Data collection method

Various samples of designed aluminum roofing sheets manufactured at different temperatures and pressures were tested with strain gauge testing machines according to the requirements of the Tensile test specimens for the American Society for Testing and Materials (ASTM) were made to the required design length. Tensile standard specimens according to ASTM E8-09 were ready for testing. The mean values were calculated after testing a total of thirty-six (36) samples. Before the tensile test, the ASTM E8M-compliant samples were thoroughly cleaned once again to remove any remaining contaminants like rust, oil, and dirt. A 250 kN Shimadzu universal tester was used to conduct tensile testing at room temperature, 50–5% humidity, and 2 mm/min crosshead speed [11]. Figure 3 depicts the experimental study's tensile testing apparatus. The stock was cut into three separate discarded test pieces, each measuring 45 mm in gauge length and 9 mm in diameter. Figure 1 illustrates the tensile specimens' dimensions. The universal lathe machine was used to machine the tensile test specimens to the necessary specifications.

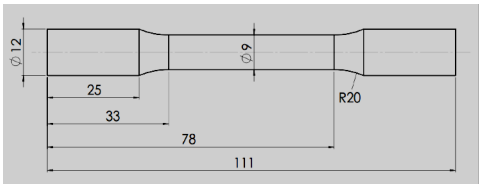

Figure 1. The dimensions of the tensile testing specimen in relation to ASTM E8-09 [1]

2.4. Evaluation of engineered aluminum roof sheets for tensile strength

The aluminum roofing sheet samples developed were evaluated for their mechanical strength (tensile strength) according to Equation 1 [14].

$$Tensile\ Strength = \frac{\text{Maximum Load}}{\text{Original Cross–Sectional Area}} \qquad (1)$$

2.5. Preparation of specimens for metallographic investigation

In this investigation, samples of aluminum with and without a grain refiner (addition of Chromium) were prepared in a way that virtually eliminates all flaws. For metallographic and mechanical tests, specimens of pure aluminum and aluminum with refinements were developed. The length of the samples used for metallographic analysis is 15 mm. For metallographic analysis, specimens of pure aluminum and aluminum with Chromium were produced to analyze the structural configuration. For tensile strength tests, specimens with and without grain refinement were produced. Homogenization was used to treat the Al-pure, and the T4 technique was used to anneal the refined specimens.

Figure 2. The tensile test specimen

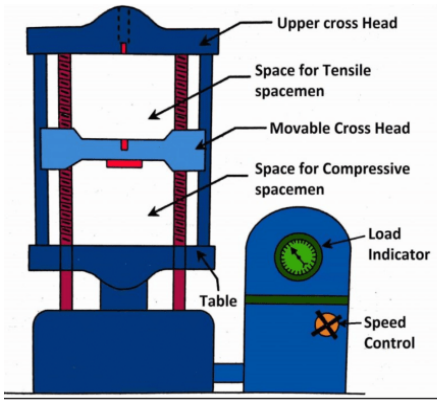

Figure 3. Universal testing machine

2.6 Metallographic investigation

The aluminum samples were examined and photographed. The samples were cleaned in water and alcohol before being dried in a warm air stream. All of the metallographic studies conducted for this study employed a Nikon AFX-11 optical microscope equipped with a 35mm camera. To see the grain, all samples with or without grain refinement were examined under the Nikon AFX-11 optical microscope.

2.7. Optimization of aluminium roofing sheets process parameters using Taguchi method

2.7.1. Experimental plan

This is one of the most thorough methods for developing a product or process is experimental design. Through a number of experiments, this statistical approach seeks to provide predictive knowledge about a challenging, multivariate process. The main design of experiments (DOE) strategy is as follows:

2.7.2. Taguchi method

A full factorial design necessitates a great deal of testing. As the number of parameters rises, this takes more time and becomes more complicated. Taguchi developed an innovative method employing an orthogonal array to explore the whole parameter space with fewer experiments to address this issue. In order to measure performance that deviates from the ideal target value, Taguchi advises employing a loss function [12].

A signal-to-noise (S/N) ratio is then created from the value of this loss function. The Taguchi method uses a signal-to-noise (S/N) ratio that reflects both the mean and variability of quality characteristics. It is a metric of effectiveness for creating systems and procedures that are resistant to noise influences.

2.8. Types of S/N Ratio

(i) *Smaller-the-better*: In Smaller-the-better,

$$Signal\ to\ noise\ ratio, \eta\left(\frac{S}{N}\right) = -10Log_{10}\{\frac{1}{n}\sum_{i=1}^{n} y_i^2\} \quad (2)$$

When a characteristic's minimization is desired, it is utilized.

(ii) *Larger-the-better*: In Larger-the-better

$$Signal\ to\ noise\ ratio, \eta\left(\frac{S}{N}\right) = -10Log_{10}\{\frac{1}{n}\sum_{i=1}^{n} \frac{1}{y_i^2}\} \quad (3)$$

Where i ranges from 1 to n, and n is the number of iterations used to complete tasks that call for optimizing the quality traits of interest with S/N (signal-to-noise ratio), n (number of observations), and yi (i-th number of observations).

(iii) *Nominal-the-best*: Equation 4 is used to determine the signal ratio for Norminal-the-best:

$$Nominal - the - best\left(\frac{S}{N}\right) = -10Log_{10}\{\frac{\mu^2}{\sigma^2}\} \quad (4)$$

when the mean, μ and standard deviation, σ are given. It is applied while attempting to reduce the RMS error near a particular target value. Matching the mean to the objective transforms the issue into a constrained optimization problem, regardless of the approach.

2.8.1. Selected signal ratio

In this study, the smaller-the-better was used. This is because production temperature (°C), production pressure (GPa), cooling time (second) and percentage of chromiun in aluminium roofing sheet (%) are intended to be lower in order to produce aluminium roofing sheets with good tensile strength.

2.9. Identifying the control factors and their levels

L9 orthogonal array and three processing parameter levels were chosen. Table 1 displays the process parameters and levels, while Table 2 displays the L9 orthogonal array.

3. Results and discussion

3.1. Microstructure examination of pure aluminum and aluminum with chromium (cr)

Figure 4a to 4e shows the microstructures of pure aluminum and aluminum alloys with different additives of (Cr) percentages.

3.2. Discussion of microstructure pure aluminium and aluminium with different additives of chromium (Cr)

3.2.1 Metallographic investigation

Compared to the unprocessed alloy (pure aluminum), the grain-refined alloys had a lower level of porosity defects, according to metallographic analysis. Additionally, as illustrated in Figure 4, the refined alloy has a less aquiaxed structure than the unprocessed alloy (pure aluminum). A finer grain was produced when grain refinement was added to the examined alloy. For the addition of 2.0% Cr, the addition of a grain refiner provides effective refining. Moreover, less refinement was obtained by the other percentages of chromium refiners. Figures 4a to 4e demonstrate that there is a somewhat notable difference between the crude and polished structure. This may be due to the fact that the initial raw material (commercial pure aluminum) contains several impurities like Ti, Zn, and B that serve as advantageous sites for nucleation when oxygen or sulfur are included.

Table 1. The process parameters and their levels

Serial Number	Factors	Level 1	Level 2	Level 3
1	Production Temperature (°C)	1022	1610	2001
2	Production Pressure (GPa)	40	65	79
3	Cooling Time (second)	44	60	85
4	Percentage of Chromiun in Aluminium Sheet (%)	0.5	2.0	3.0

Table 2. The orthogonal array for L9

Experiment Number	Control Factors			
	Production Temperature (°C)	Production Pressure (GPa)	Cooling Time (second)	Percentage of Chromium in Aluminium Sheet (%)
1	1	1	1	1
2	1	2	2	2
3	1	3	3	3
4	2	1	2	3
5	2	2	3	1
6	2	3	1	2
7	3	1	3	2
8	3	2	1	3
9	3	3	2	1

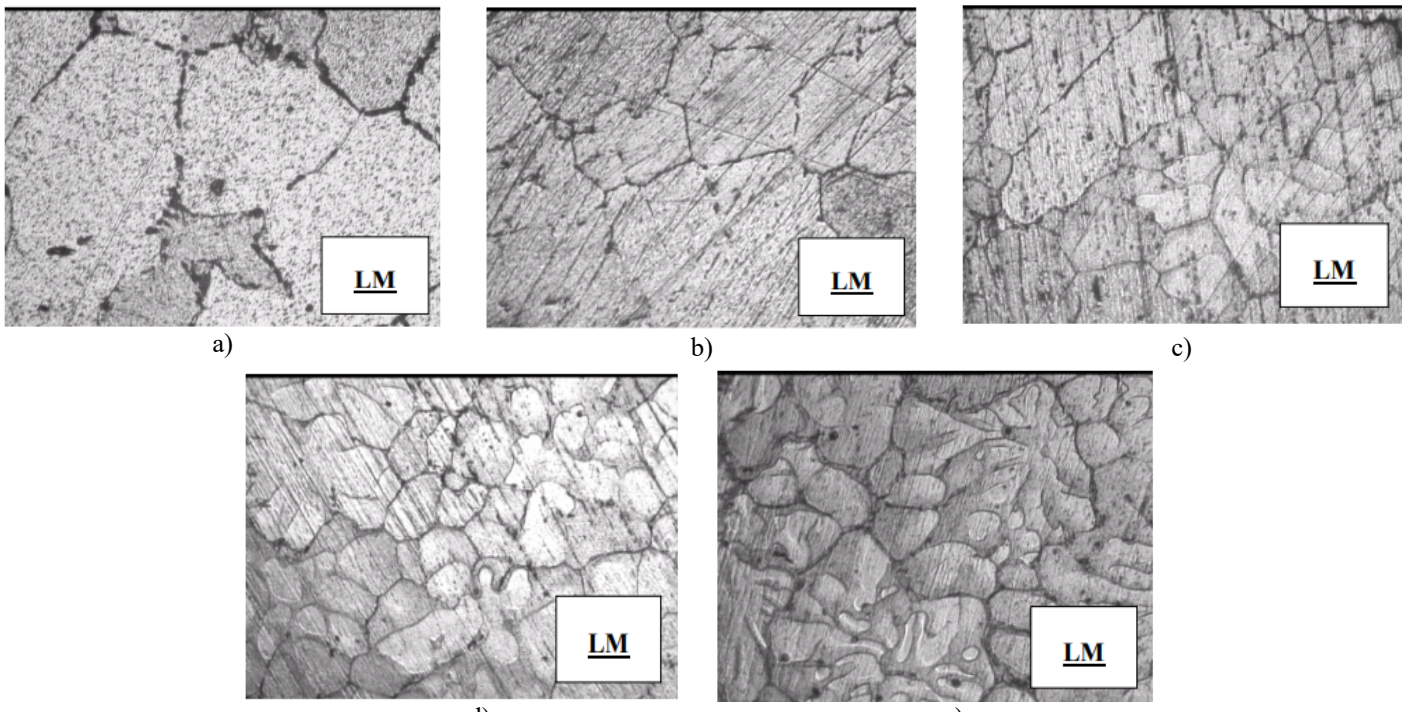

Figure 4. Microstructures of samples; a) pure aluminum, b) Al ± 0.5% Cr, c) Al ± 1.0% Cr, d) Al ± 1.5% Cr and e) Al ± 2.0% Cr

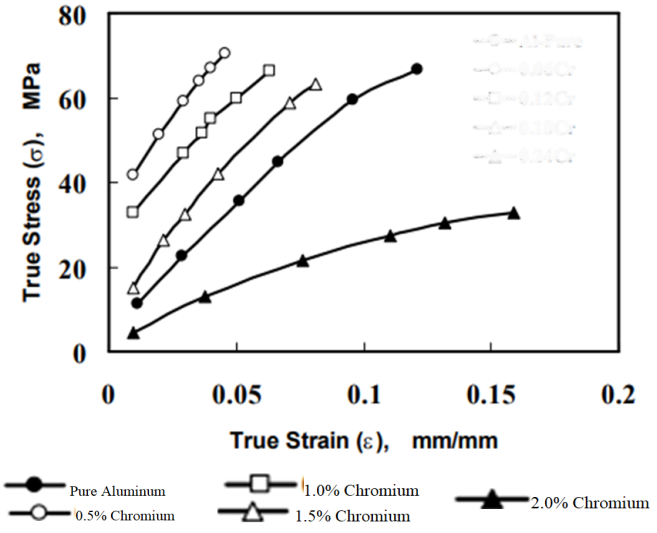

Figure 5. Pure aluminium (Al-Pure) with different Additives of chromium

3.2.2 Effect of Grain Refining Additions

The casting process was used to study the effects of grain refining additives, such as Cr, on increasing the mechanical characteristics and grain refining of pure aluminum. Optical microscopy was used to examine the effects of grain refining during the material production process following casting. Tensile strength tests and experimental findings for aluminum produced with and without additions of grain refininer were investigated. It was observed that the presence of Cr as a master alloy affect the tensile strength of the various refinements of aluminum.

3.2.3. Grain Refining Effect on the Flow Stress

When compared to the ductility of pure aluminum (Al-pure), the tensile behavior of all refined specimens shows high ductility. According to Figure 5, all of the tensile specimens with various additive addition percentages exhibit an increase in flow stress when compared to pure aluminum. Except for the specimens with 2.0% Cr, which recorded the lowest flow stress as shown in Figure 5. The effect of grain refining with various grain refining additives is noticeable in general. Figure 5 illustrates how the flow stress value for the alloy with the addition of 0.5% Cr is greater than that for pure aluminum by roughly 50% and greater than that for all other additions combined.

3.3. Optimization results using Taguchi method

The components and levels listed in Table 1 were used in the studies, per the orthogonal table (OA) above. Table 3 presents the experimental configuration with the chosen factor values. Each of the nine aforementioned experiments was carried out. 36 trials were conducted a total of four times to account for potential changes brought on by noise sources. The measured values of the process parameters acquired from various tests are displayed in Tables 4 through 7.

3.1 Determining the Experimental Matrix

The orthogonal table (OA) above indicates that the components and levels used in the trials were those listed in Table 1. Table 3 displays the experimental configuration with the chosen values for the factors. Each of the nine aforementioned experiments was carried out. Four (4) times (that is, a total of 36 experiments) to account for potential changes brought on by noise elements. The measured values of the process parameters derived from several tests are displayed in Tables 4 to 7.

Table 3. Orthogonal array with control factors and tensile strength for aluminium roofing sheets

Experiment Number	Control Factors				Tensile Strength (MPa)
	Production Temperature (°C)	Production Pressure (GPa)	Cooling Time (second)	Percentage of Chromium in Aluminium Sheet (%)	
1	1022	40	44	0.5	342
2	1022	65	60	2.0	469
3	1022	79	85	3.0	543
4	1610	40	60	3.0	452
5	1610	65	85	0.5	600
6	1610	79	44	2.0	621
7	2001	40	85	2.0	612
8	2001	65	44	3.0	602
9	2001	79	60	0.5	594

Table 4. Measured values of production temperature for aluminium roofing sheets

Experiment Number	Production Temperature (°C)				
	1	2	3	4	Mean
1	1023	1020	1025	1020	1021.50
2	1190	1200	1198	1196	1196.00
3	1372	1442	1432	1439	1421.25
4	1600	1610	1601	1596	160.175
5	1792	1800	1788	1790	1792.50
6	1921	1921	1920	1930	1923.00
7	1991	2001	1990	1985	1991.75
8	1023	1024	1034	1030	1027.75
9	1189	1200	1190	1196	1193.75

Table 5. Measured values of production pressure for aluminium roofing sheets

Experiment Number	Production Pressure (GPa)				
	1	2	3	4	Mean
1	38	43	40	42	40.75
2	54	53	56	56	54.75
3	61	60	62	62	61.25
4	66	68	65	63	65.50
5	69	68	69.5	70	69.125
6	72	71	72	73	72.00
7	73	75	74	76	74.50
8	76.5	77	76	78	76.875
9	80	77	78	79	78.50

Table 6. Measured values of cooling time for aluminium roofing sheet production

Experiment Number	Cooling Time (second)				
	1	2	3	4	Mean
1	41	42	44	43	42.50
2	45	44	47	48	46.00
3	48	54	51	50	50.75
4	56	58	57	59	57.50
5	58	62	58	61	59.75
6	60	65	66	63	63.50
7	72	73	74	71	72.50
8	74	76	77	75	75.50
9	81	80	82	85	82.00

Table 7. Measured values of percentage of chromium in aluminium roofing sheets (%)

Experiment Number.	Percentage of Chromium in Aluminium Roofing Sheet (%)				
	1	2	3	4	Mean
1	3.0	0.5	3.0	2.0	2.125
2	0.5	1.2	1.3	1.2	1.050
3	0.8	2.0	0.8	2.3	1.475
4	1.0	1.6	1.0	0.8	1.100
5	2.0	2.2	2.0	0.6	1.700
6	1.5	3.0	1.5	0.5	1.625
7	2.5	2.1	2.5	2.3	2.400
8	1.8	1.7	1.8	2.8	2.025
9	1.2	1.2	1.2	1.9	1.375

Table 8. Tabulated signal-to-noise ratios for of aluminium roofing sheets

Experiment Number	S/N Ratio (dB) for Production Temperature (°C)	S/N Ratio (dB) for Pressure (GPa)	S/N Ratio (dB) for Cooling Time	S/N Ratio (dB) for Percentage of Chromium in Aluminium Sheet (%)
1	-60.1890	-32.2122	-32.5708	-7.4527
2	-61.5550	-34.7701	-32.1445	-0.8099
3	-63.0550	-35.7429	-34.1166	-4.2202
4	-64.0919	-36.3281	-35.1950	-11.3943
5	-65.0692	-36.7932	-35.5306	-5.1851
6	-65.6796	-37.1471	-36.0611	-5.3624
7	-65.9847	-36.2185	-37.2078	-7.4429
8	-60.2378	-36.4741	-37.5599	-6.3372
9	-61.5383	-37.8982	-38.2785	-2.9721

For each of the different control parameters, the S/N ratio (η) is determined as shown below:

Sum of Squares for production temperature from 1 to 3;

$$S_{T1}=(\eta_1+\eta_2+\eta_3) \quad (5)$$

Sum of Squares for production temperature from 4 to 6;

$$S_{T2}=(\eta_4+\eta_5+\eta_6) \quad (6)$$

Sum of Squares for production temperature from 7 to 9;

$$S_{T3}=(\eta_7+\eta_8+\eta_9) \quad (7)$$

Sum of Squares for production pressure from 1 to 3;

$$S_{P1}=(\eta_1+\eta_4+\eta_7) \quad (8)$$

Sum of Squares for production pressure from 4 to 6;

$$S_{P2}=(\eta_2+\eta_5+\eta_8) \quad (9)$$

Sum of Squares for production pressure from 7 to 9;

$$S_{P3}=(\eta_3+\eta_6+\eta_9) \quad (10)$$

Sum of Squares for cooling time from 1 to 3;

$$S_{T1}=(\eta_1+\eta_5+\eta_9), \quad (11)$$

Sum of Squares for cooling time from 4 to 6;

$$S_{T2}=(\eta_2+\eta_6+\eta_7) \quad (12)$$

Sum of Squares for cooling time from 7 to 9;

$$S_{T3}=(\eta_3+\eta_4+\eta_8) \quad (13)$$

Sum of Squares for percentage of chromium from 1 to 3;

$$S_{C1}=(\eta_1+\eta_4+\eta_7) \quad (14)$$

Sum of Squares for percentage of chromium from 4 to 6;

$$S_{C1}=(\eta_2+\eta_5+\eta_8) \quad (15)$$

Sum of Squares for percentage of chromium from 7 to 9;

$$S_{C1}=(\eta_3+\eta_6+\eta_9) \quad (16)$$

See Table 9 to choose values for η_1, η_2, η_3, etc., and to calculate S_1, S_2, and S_3. The S/N ratio for this experiment, ηjk, is denoted by the symbol k. For level 1 production temperatures, the typical S/N ratio is $\frac{ST_1}{3}$. For level 2 production temperatures, the typical S/N ratio is $\frac{ST_2}{3}$. The typical S/N ratio for level 3 production temperatures is $\frac{ST_3}{3}$.

Every factor's comparable level is j. The production pressure, cooling time, and chromium content of aluminum roofing sheets are each calculated using comparable formulae. The average signal-to-noise ratio is shown in Table 9.

Table 9. The response table for s/n ratio for aluminium process parameters

Serial Number	Production Temperature (°C)	Production Pressure (GPa)	Cooling Time	Percentage of Chromium in Aluminium Sheet (%)
Level 1	-61.5997	-34.2417	-32.9440	-4.1609
Level 2	-64.9469	-36.7561	-35.5956	-7.3139
Level 3	-62.5869	-36.8636	-37.6821	-5.5841
DELTA	3.3472	2.6219	4.7381	3.1530
RANK	2	4	1	3

*DELTA= Absolute highest signal Noise ratio - Absolute Lowest signal Noise ratio

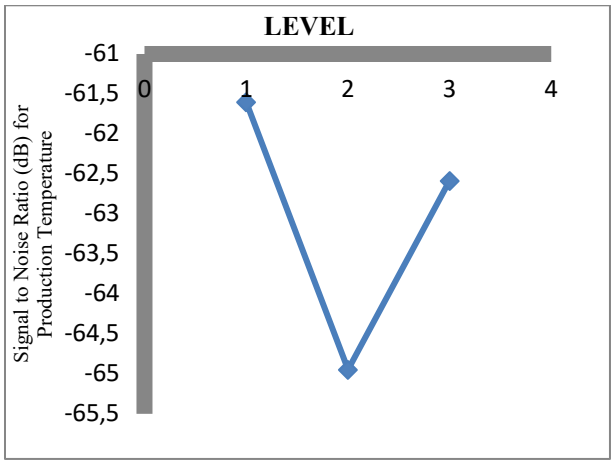

Figure 6. Signal to noise ratio for production temperature

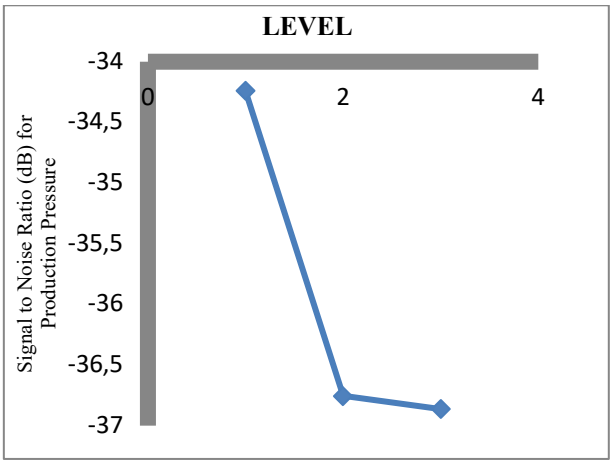

Figure 7. Signal to noise ratio for production pressure

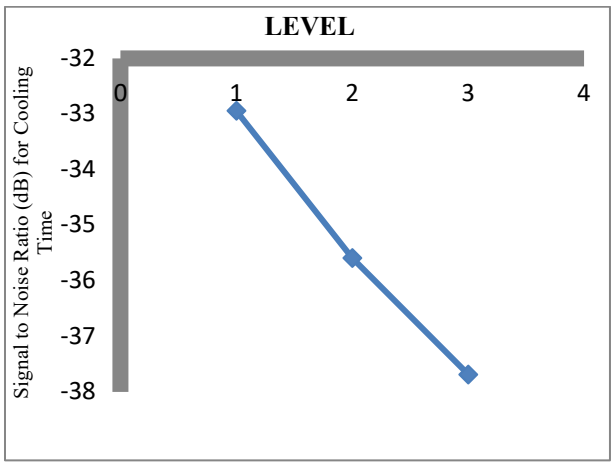

Figure 8. Signal to noise ratio for cooling time

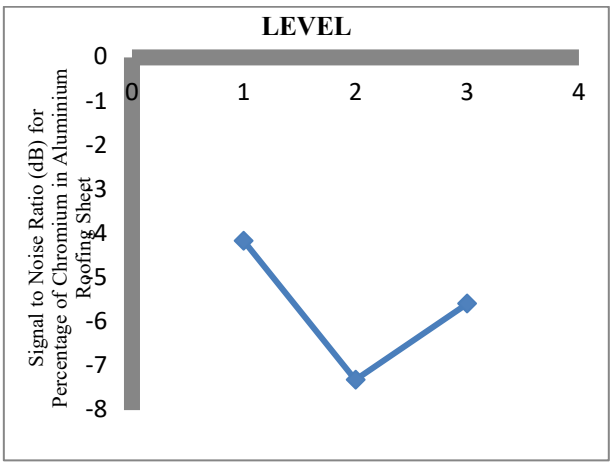

Figure 9. Signal to noise ratio for percentage of chromium in aluminium roofing sheet (%)

3.2. Confirmation experiment

The confirmation experiment, which was performed using manufacturing parameters of 1610 ºC, 79 MPa, 85 s of cooling time, and 2.0% chromium in aluminum roofing sheets, is shown in Table 11. A total of five sets of experiments were run in the confirmation experiment, and their tensile strength was assessed. It is evident that the outcomes were reliable.

Table 10. Optimum values of factors of developed aluminium roofing sheets

Process Parameter	Optimum Value
Production Temperature (ºC)	1610°C
Production Pressure (MPa)	79 GPa
Cooling Time (second)	85 seconds
Percentage of Chromium in Aluminium Roofing Sheets (%)	2.0%

Table 11.: Confirmation experiment

Serial Number	Process Parameters				Tensile Strength (Mpa)
	Production Temperature (ºC)	Production Pressure (MPa)	Cooling Time (second)	Percentage of Chromium in Aluminium Roofing Sheets (%)	
1	1610	79	85	2.0	592.0
2	1610	79	85	2.0	592.5
3	1610	79	85	2.0	591.5
4	1610	79	85	2.0	591.0
5	1610	79	85	2.0	593.0
Mean Tensile Strength					592

3.3 Discussion of Results from Optimization using Taguchi method

The response table for the S/N ratio is shown in Table 9. The best set of combination parameters was determined to be the one with the highest value for each factor. The ideal process parameter combinations for aluminum roofing sheets are LEVEL 2 for production temperature, LEVEL 3 for production pressure, LEVEL 3 for cooling time, and LEVEL 2 for chromium content. The delta value in Table 9 illustrates the variable that has the largest influence on the tensile strength of aluminum roofing sheets. The factor with the biggest effect on the tensile strength of aluminum roofing sheets was found to have a delta value for cooling time of 4.7381. Production temperature, with a Delta value of 3.3472, production pressure, with a Delta value of 2.6219, and the percentage of chromium all came after that (Table 9). A response diagram for the generated S/N ratio is shown in Figure 6-9. The greatest S/N ratio for each factor was used to calculate the optimal process condition, which corresponds to a production temperature of 1610 °C, a production pressure of 79 GPa, a cooling time of 85 seconds, and a chromium percentage of 2.0% (Table 10). The factor levels with the highest S/N ratio were chosen to help the problem. The confirmation experiment further demonstrates that a mean tensile strength of 592.0 MPa was achieved. The mechanical characteristics of vortex-produced composites of 2024 aluminum alloy enhanced with Al_2O_3 particles were investigated by Kok [21]. For the production process, 700°C for casting, 550°C for mold preheating, 900 rpm for mixing speed, and 5 g/min for particle addition speed are the ideal melting temperatures, mold preheating temperatures, mixing speeds, particle addition speeds, mixing times, and contact pressure. The mixing period is 105 seconds, and the contact pressure is 6 MPa. The obtained production temperature is consistent with this investigation. Adin and Şcan [32] used the Taguchi approach to optimize the process parameters of medium-carbon steel joints connected by MIG welding. The results revealed that the groove angle of 90°, the current of 120 A, and the voltage of 30 V produced the greatest tensile strength of 597.963 MPa and the lowest tensile strength of 395.125 MPa. The optimal tensile strength value of 592 MPa found in this investigation agrees with the highest tensile strength of 597.963 MPa. A numerical analysis of the fatigue

behavior of unpatched and patched aluminum and composite plates is conducted by Hamit et al. [11]. They used mathematics to investigate the fatigue behavior of composite patched and unpatched Al 5083 aluminum plates. The toughness results obtained in their study serves as a basis for the tensile strength obtained in this study. The obtained values in this study were used to improve the material property (tensile strength) of aluminum roofing sheet in aluminum production industries.

4. Conclusion

Chromium (Cr) additives in varying concentrations, ranging from 0.5% Cr to 2.0% Cr was added to pure aluminium. It was used to refine grains of commercially pure aluminum. The grain size reduces as the percentage of additives increases. As the ratio of chrome grows in Cr additions, so does the refined alloy's tensile strength increases. The best combinations of manufacturing conditions for the tensile strength of aluminum roofing sheets were found using the Taguchi method. According to the results, the optimum mean tensile strength of 592Mpa was obtained at manufacturing temperatures of 1610 °C, production pressure of 79 GPa, cooling time of 85 seconds and percentage of chromium of 2.0%. The most important aspect was discovered to be cooling time, which was followed by manufacturing temperature and chromium content. The least effective component was determined to be production pressure. This study is intended to help researchers and manufacturers of aluminum develop high-quality, defect-free aluminum roofing sheets, which would ultimately boost productivity in the aluminum industries.

Author Contributions

The percentages of author(s) contributions are presented below. All authors reviewed and approved final version of the manuscript.

%	D.D.O.	A.E
C	60	40
D	60	40
S	50	50
DCP	50	50
DAI	60	40
L	50	50
W	50	50
CR	60	40
SR	60	40
PM	50	50
FA	50	50

C= concept, D= design, S= supervision, DCP= data collection and/or processing, DAI= data analysis and/or interpretation, L= literature search, W= writing, CR= critical review, SR= submission and revision, PM= project management, FA= funding acquisition.

Conflict of Interest

In this project, there was no conflict of interest in the review, collection of data, analysis of data, in the writing of the manuscript, or in the decision to publish the results.

Acknowledgments

The authors acknowledged the Department of Mechanical Engineering, Faculty of Engineering, Benson Idahosa University and Igbinedion University respectively for the using some of their facilities during the fabrication process.

References

1. Elmas, S., Ageing behaviour of Spray Coot Al-Zn-Mg-Cu Alloys, Turk journal of Engineering Environmental Science, **2022**, 25: 681-686
2. Song, W., The Effect of Thermal Ageing on the Alorasive Wear Behavior of Age Hardening A1/Sic and 6061 A1/Sic Composite. Wear Journal, **2023**, 185: 125-130
3. Lee, W., The Strain Rate and Temperature Dependence of the Dynamic İmpact Properties of 7075 Aluminum Alloy, Journal of Materials Processing Technology, **2020**, 100: 116-122
4. Kagawa, Y., Temperature Dependence of Tensile Machanical Properties in SiC Fiber Reinforced Ti Matrix composite, Journal of Engineering, **1994**, 2 (9): 3019-3026
5. Jingyu, L., Tingqi, Q., Zhanli, C., Wanze, Z., Minglong W., Chuanzhi Du., Study of vibration frequency-fatigue strength action of 6061-T6 aluminum alloy during fillet welding, Journal of Vibroengineering, **2021**, 8: 1-16
6. El-Nasser, G.A., Nassef, A.E., and El-Soeudy, R.I., Modification of AA7075 Alloy by Addition of Al-5Ti-1B Alloy, 5th International Engineering Conference, **2006**, 27-3
7. Sofyan, B., Absevations of the Effect of Zn on Precipitation Processes in an Al-Cu-Mg-Ag Base Alloy, Journa of Material Science, **2020**, 337: 977-982
8. Yoshımı, W., Noboru, Y., Yasuyoshı, F., Wear Behaviour of Al-Al3Ti Composite Manufactured by a Centrifugal Method,´ Metallurgıcal and Materıals Transactıons A, **1999**, 30: 3253-3261
9. Lee, K., Fabrication of Al-3Wt PCT Mg Matrix Composites Reinforced with Al_2O_3 and SiC Particulates by the Pressureless Infiltration Technique, Metallurgical and Materials Transactions, 1998, 29: 3087-3094
10. Song, N., Shi, G.T., Gray III & Roberts, J. A., Reinforcement Shape Effect on the Fracture Behavior and Ductility of Particulate Reinforced 6061Al Matrix composite, Metallurgical and Materials Transactions A, **1996**, 27:3739-3355
11. Hamit, A., Sağlam, Z., & Adin, M.Ş., Numerical Investigation of Fatigue Behavior of Non-Patched and Patched Aluminum/Composite Plates, European Mechanical Science, **2021**, 5(4):168-176
12. Taguchi, G., and Konishi, S., Taguchi Methods, Orthogonal Arrays and Linear Graphs, Tools for Quality American Supplier institute, **1987**: 8-35
13. Osarenmwinda, J.O., Olodu, D.D., Optimization of Injection Moulding Process Parameters in the Moulding of High Density Polyethylene (HDPE), Journal of

Applied Science and Environmetal Management, **2018**, 22(2): 203-206
14. Srinivas, A., Venkatesh, Y.D., Application of Taguchi Method for Optimization of Process Parameters in Improving the Surface Roughness of Lathe Facing Operation, International Refereed Journal of Engineering and Science (IRJES), **2012**, 1(3):13-19
15. Olodu, D.D., Optimization and Analysis of Cutting Tool Geometrical Parameters using Taguchi Method, Journal of Applied Science and Environmetal Management, **2018**, 22 (3): 346-349
16. Rao, R.S., Ganesh K, C., Shetty Prakasham, R., Phil J.H., The Taguchi Methodology as a Statistical Tool for Biotechnological Applications: A Critical Appraisal, Biotechnology Journal, **2019**, 3 (4): 510–523
17. Foster, W.T., Basic Taguchi Design of Experiments. National Association of Industrial Technology Conference, Pittsburgh,PA, **2000**
18. Altan, M., Reducing Shrinkage in Injection Moldings through the Taguchi, ANOVA and Neural Network Methods, Journal of Material Design, **2010**, 31, 599–604
19. Vaatainen, O, Pentti, J., Effect of Processing Parameters on the Quality of Injection Moulded Parts by Using the Taguchi Parameter Design Method, Journal of Plastic Rubber Composite, **2016**, 1: 21-217
20. Olodu D. D., Modelling and Validation of the Production Parameters of Unalloyed Aluminium Sheets, Gazi University Journal of Science Part A: Engineering and Innovation, **2021**, 8(1): 94-108
21. Kok, M., Production and Mechanical Properties of Al_2O_3 Particle-Reinforced 2024 Aluminium Alloy Composites, Materials Processing Technology Journal, **2005**, 161(3): 381-387
22. Kumar, A., Lal, S., & Kumar, S., Fabrication and Characterization of A359/Al_2O_3 Metal Matrix Composite using Electromagnetic Stir Casting Method, Journal of Materials Research and Technology, **2013**, 2(3): 250-254
23. Venkatesh, B., & Harish, B., Mechanical Properties of Metal Matrix Composites (Al/SiCp) Particles Produced by Powder Metallurgy, International Journal of Engineering Research and General Science. **2015**, 3(1): 1277-1284
24. Nieh, T. G., & Chellman, D. J., Modulus Measurements in Discontinuous Reinforced Aluminum Composites, Scripta Metallurgica, **1984**, 18: 925-938
25. Friend, C.M., The Effect of Matrix Properties on Reinforcement is Short Al_2O_3 Fiber-Al MMCs, Journal of Materials Science, **1987**, 22(8): 3005-3010
26. Yao, B., Hofmeister, C., Patterson, T., Sohn, Y., van den Bergh, M., Delahanty, T., & Cho, K., Microstructural Features Influencing the Strength of Trimodal Aluminum Metal-matrix-Composites, Composites Part A: Applied Science and Manufacturing, **2010**, 41(8): 933-941
27. Saravanan, C., Subramanian, K., Ananda Krishnan, V., & Sankara N.R., Effect of Particulate Reinforced Aluminium Metal Matrix Composite, Mechanics and Mechanical Engineering, **2015**, 19(1): 23-30
28. Prabu, S. B., Karunamoorthy, L., Kathiresan, S., & Mohan, B., Influence of Stirring Speed and Stirring Time on Distribution of Particles in Cast Metal Matrix Composite, Journal of Materials Processing Technology, **2006**, 171(2): 268-73
29. Joardar, H., Sutradhar, G., & Das, N. S., FEM Simulation and Experimental Validation of Cold Forging Behavior of LM6 Base Metal Matrix Composites, Journal of Minerals and Materials Characterization and Engineering, **2012**, 11(10): 989-994
30. Romanova, V. A., Balokhonov, R. R., & Schmauder, S., The Influence of the Reinforcing Particle Shape and Interface Strength on the Fracture Behavior of a Metal Matrix Composite, Acta Materialia, **2009**, 57(1): 97-107
31. Domnita, F., and Cristian, C., Application of Taguchi Method to Selection of Optimal Lubrication and Cutting Conditions in Face Milling of $AlMg_3$, Journal of Cleaner Production, **2011**, 19:640-645
32. Osarenmwinda, J.O., Olodu, D.D., Effect of Barrel Temperature on the Mechanical Properties of Injection Moulded Products. Nigeria Journal of Technology (NIJOTECH), **2015**, 34(2): 292-296
33. Adin, M., Ş., and İşcan, B., Optimization of Process Parameters of Medium Carbon Steel Joints Joined by MIG Welding using Taguchi Method. European Mechanical Science, **2022**, 6(1): 17-26
34. Yildiz, R. A., Evaluation of Fracture Toughness and Charpy V-notch Test Correlations for Selected Al alloys. European Mechanical Science, **2022**, 6(1): 1-8

The International Journal of Materials and Engineering Technology (TIJMET) (2023) 6(2)
http://dergipark.gov.tr/tijmet
ISSN: 2667-4033

RESEARCH ARTICLE

Impact of subzero heat treatment on some mechanical properties of bimetals

Zafer Özdemir*

Haliç University, Engineering Faculty, Mechanical Engineering Department, İstanbul, Türkiye

Article Info
Article history:
Received 07.06.2023
Revised: 08.08.2023
Accepted: 06.09.2023
Published Online: 30.09.2023
Keywords:
Bimetal
Hardness
Impact test
High alloy cast iron (HCCI)
Low alloy steel (LCCS)
Deep cryogenic treatment

Abstract

Deep cryogenic (subzero) treatment (DCT) influence on the mechanical properties of bimetals used in the crushing industry has been examined and analyzed in the current study. Examinations include annealing at 800°C, DCT, tempering at 250°C, charpy impact test, optic microscope (OM) images analysis, scanning electron microscope (SEM) images analysis, X-RAY images analysis and hardness measurement as Rockwell C. Bimetals (2 set each, 1 set is 5 sample) are put to annealing at 800°C for 5 hours, then DCT is executed at -180°C for 24 hours. Tempering is followed out out at 250°C for 3 hours for 1 set. The impact toughness rates after DCT/Tempering and after DCT are found with the help of charpy impact tests. Hardness rates and metallography of test pieces are examined and compared. Noteworthy hardness and toughness rates are observed after DCT. It was also observed that after DCT/Tempering, hardness is reduced, but impact energy/toughness is increased. A clean microstructure has been observed after DCT in OMs and SEMs. X-RAY analysis also reveals a pure and clean chemical composition. The impact toughness rates of samples after DCT+Tempering are determined %20 more compared with the rates after DCT. Hardness rates decreases %10 after DCT+Tempering compared with the rates after DCT.

1. Introduction

Bimetals are promising structural metallic materials used in crushing industries owing to their noteworthy mechanical properties (1). They are developed in nearly last 4 decades, and became a serious alternative to high manganese steel alloys, esp. to the Hadfield steel (2). Because of their high wear resistance properties and impact strength, they are extensively used in recent years. In comparison to classical high-Mn (Hadfield Steel Mn: %12, hardness Rockwell C:48) steel, bimetals' advantages are being harder and tougher, and having longer life (3,4). They can be manufactured by two methods; in the first method is liquid–liquid casting (gravity method; conducted in this study) and second method is liquid–solid (mold-cavity preparation) configuration (5,6). Details are given in materials and method section.

To improve the mechanical properties and eliminate residual stresses, conventional heat treatment methods are applied after casting process (8). However, when high toughness and impact resistance is needed, an alternative but overcosting method, Deep Cryogenic Treatment (DCT) can be applied as well as conventional heat treatment. In DCT process; the metals have been brought down to almost -180°C from high temperatures (800-900°C), applying liquid Nitrogen for approximately 24 hours, then they can be subjected to tempering at approximately at 250°C and finally quenched in still air until room temperature (9,10).

Thanks to this method, high toughness and hardness values can be obtained. These properties are very significant for wear resistance and impact strength (11).

Conventional heat treatment process, shallow cryogenic treatment and mechanical properties of bimetals have been investigated previously by Z.Özdemir in his previous studies (12,13).

In cryogenic treatment (CT), ultra-cold temperatures are applied to materials to change the microstructure. A highly cost reduction and performance increase can be obtained. Down to -184°C temperatures can be used. The cryogenic process is an extension of heat treatment, and can improve specifications of the material. The basic CT process consists of a gradual cooling of the component until the defined temperature, holding it for a given time (freezing time), and then progressively leading it back to the room temperature. Shallow cryogenic treatment is to gradually cool the workpiece at about - 84°C and deep cryogenic treatment (DCT) is to cool the workpiece at about -184°C (8,10).

Significant studies have been made on the cryogenic treatment of metals and dissimilar metals up till now. Some of the considerable ones have been mentioned below.

M.Ş. Adin and M.Okumuş investigated the microstructure and mechanical Properties of dissimilar metal weld between AISI 420 and AISI 1018 steels, conducted tensile tests and measured the hardness values and achieved remarkable results (14). M.Ş.Adin studied the effect of cryogenic treatment on cutting tools in machining of AA7075 aerospace aluminium alloy (15) and mechanical properties of MIG and TIG welded dissimilar steel joints (16) in his recent investigations.

The scientific purpose of our study is to investigate the HCCI and LCCS bimetallic castings in terms of toughness, hardness and metallography, comparison after DCT and DCT+Tempering. The effect of DCT and DCT+Tempering process are compared and analyzed with regards to toughness and hardness.

2. Materials and methods

High alloy cast iron (17) and low alloy steel (18) are chosen for examinations (Table 1 and 2).

Corresponding Author: Zafer Özdemir
E-mail: ozdemirzafer@yahoo.com

How to cite this article:
Özdemir, Z., Impact of Subzero Heat Treatment on Some Mechanical Properties of Bimetals, The International Journal of Materials and Engineering Technology (TIJMET), 2023, 6(2): 41-45

Process consists of 5 steps:

a. Casting
b. HT/DCT/Tempering
c. Impact Tests,
d. OM/SEM/X-RAYs
e. Hardness Test.

Table 1. Chemical composition of low carbon cast steel grade (%)

C	Si	Mn	P	Al	Cu	Cr
0,17	0,20	1,40	0,045	0,005	0,15	0,13
Ni	Mo	W	S	V	Fe	
0,06	0,01	0,001	0,042	0,05	rest	

Table 2. Chemical composition of high alloy cast iron grade G-X300CrMo27 (%)

C	Si	Mn	P	Al	Cu	Cr
3,10	0,398	0,822	0,002	-	0,135	21,8
Ni	Mo	W	S	V	Fe	
0,47	1,60	-	0,059	-	rest	

Chemical composition is shown in Tables 1 and 2. OM is carried out by Nikon Eclipse LV 150, SEM/X-RAY analysis has been carried out by FEI/Quanta 450 FEG, chemical analysis with BAIRD-DVG Spectrometer. Hardness rates are tested as Rockwell C (19).

2.1. Casting process

Gravity casting is conducted (high Cr-white cast iron Metal 2, low alloyed steel Metal 1) for casting of bimetal composite as shown in Fig.1. Liquid metal 1 (LAS) at 1580°C were poured into metal receiver 1 (fig. 1). The interface temperature has been measured by using thermocouple Pt-PtRh13. After appropriate temperature has been get, an activator boron and sodium mixture were dropped into metal 1 melt to prevent oxidation and get a permanent joint between 2 metals; right after that liquid metal 2 (high Cr white cast iron) at 1420°C were poured 2 (fig. 1).

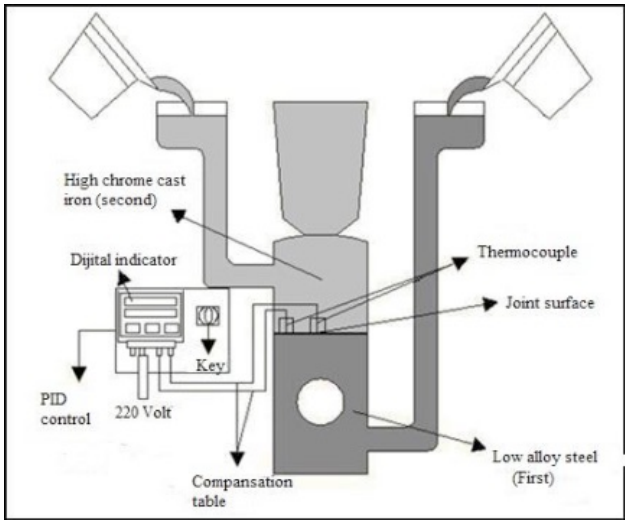

Figure 1. A schematic view of bimetal gravity casting process

All the samples have been prepared as Charpy Impact Test specimens in accordance with standard (20) before processes begin.

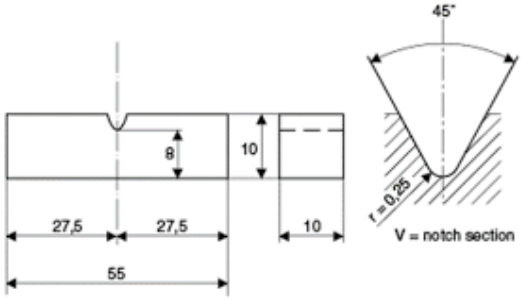

Figure 2. Charpy Impact Test Sample (20)

The velocity of pendulum is 5,2 m/s. and the beginning angle of pendulum is 150° in charpy impact tests (fig.3).

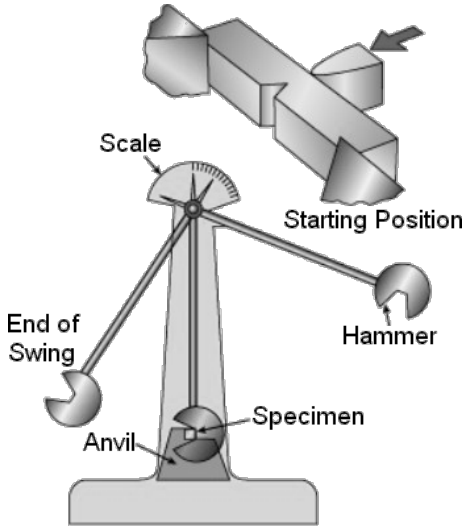

Figure 3. Charpy Impact Test Machine (20)

2.2. HT/DCT/Tempering Process

Annealing is executed to bimetals (2 layers, one of high alloy cast iron and the other layer low alloy steel) which are shown in figure 2 at 800°C for 5 hours (21).

After annealing, DCT is carried out at -180°C for 24 hours. After DCT, tempering is executed for 1 group (5 samples) at 250°C for 5 hours and the second group (5 samples) have been restored to room temperature (Fig.4). (22).

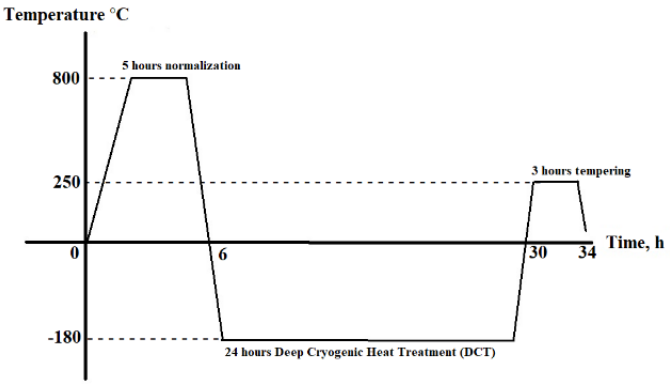

Figure 4. Overall HT/DCT/Tempering Process

2.3. Charpy Impact Tests

Impact tests are executed in accordance with the ASTM E23-02 “Standart Test Methods For Notched Bar Impact Testing Of Metallic Materials” (20). Test pieces are taken from bimetal castings and set before DCT/Tempering and DCT separately as seen in figure 5.

The results at table 3 and 4 have been obtained and the samples are observed as in figure 6 after tests.

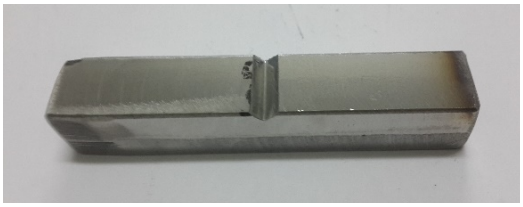

Figure 5. Charpy Impact Test Sample

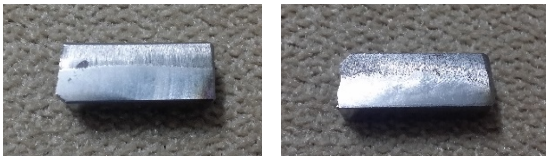

Figure 6. Charpy Impact Test Sample (after test)

Table 3. Charpy Impact Test Results (after DCT)

Energy (J.)	Sample 1	Sample 2	Sample 3	Sample 4	Sample 5
LCS	4,6	4,9	5,4	5,3	5,4
HCCI	9,5	9,1	9,2	8,7	8,5

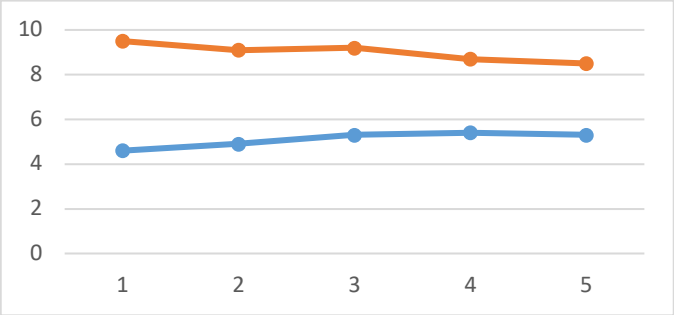

Figure 7. Charpy Impact Tests Fracture Energy as Joule, Orange is High Cr Cast Iron, Blue is Low Alloy Steel (after DCT)

Table 4. Charpy Impact Test Results (after DCT/Tempering)

Energy (J.)	Sample 1	Sample 2	Sample 3	Sample 4	Sample 5
LCS	5,4	6,2	6,4	6,8	6,0
HCCI	12,3	11,8	12,4	12,7	11,5

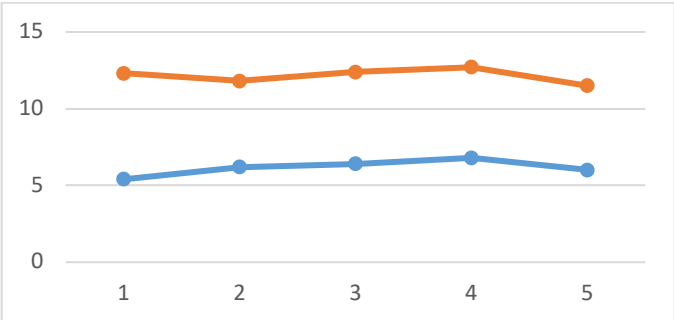

Figure 8. Charpy Impact Tests Fracture Energy as Joule, Orange is High Alloy Cast Iron, Blue is Low Alloy Steel (after DCT/Tempering)

The toughness rates are increased 20 % after DCT+Tempering as seen in figure 8 and 9.

2.4. Microstructure after DCT and after DCT/Tempering (OM/SEM/X-RAYs)

The microstructural examination of all the specimens has been carried out for validating the transformations occurred in the surface of the specimens after DCT and DCT/Tempering.

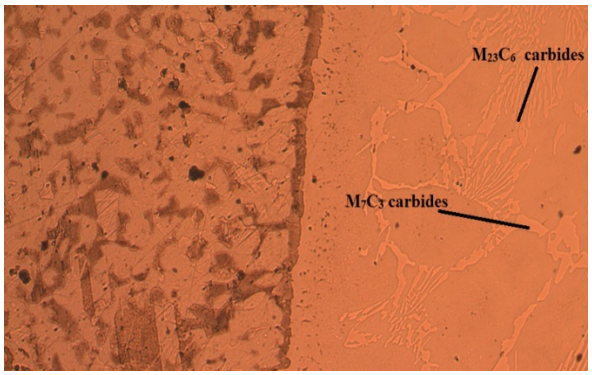

Figure 9. OM After DCT/Tempering (400 X)

Carbides affect the toughness and hardness in bimetals (Fig.9).

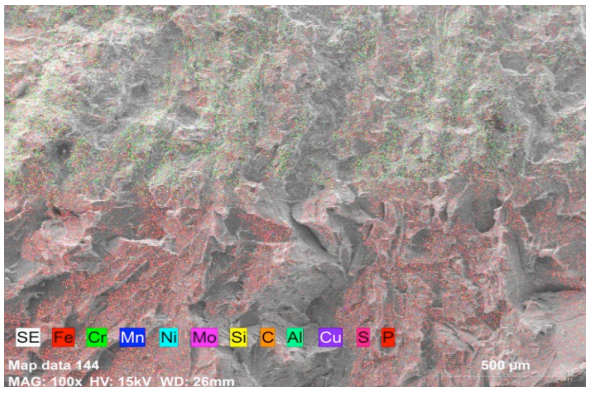

Figure 10. X-Ray After DCT/Tempering (full structure)

A successful casting of bimetal is obtained as seen in figure 10.

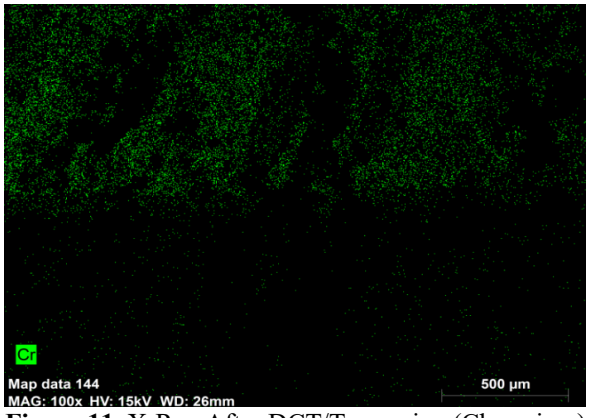

Figure 11. X-Ray After DCT/Tempering (Chromium)

Chromium content is dispersed equally and homogeneous in the high Cr cast iron side of bimetal (fig.11).

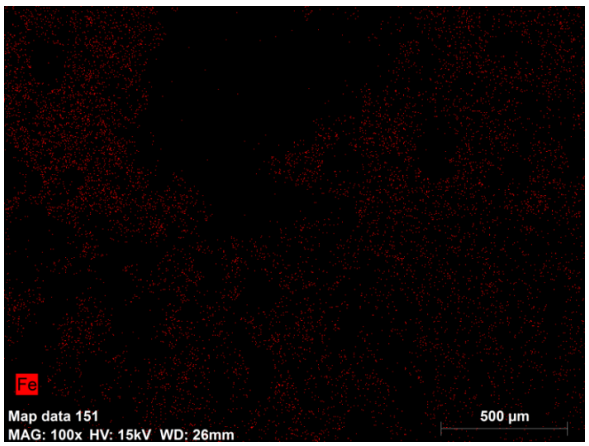

Figure 12. X-Ray After DCT/Tempering (Ferrite)

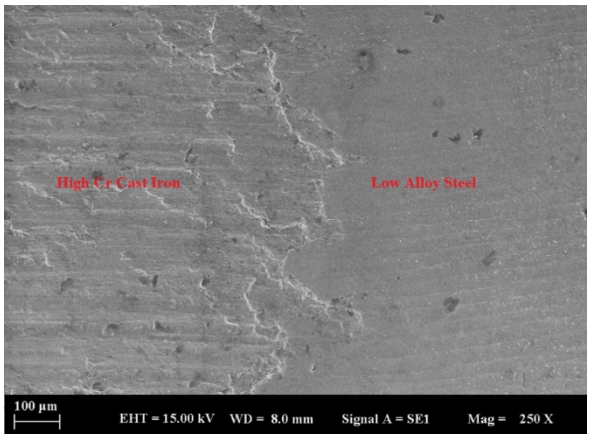

Figure 13. SEM After DCT/Tempering 250 X

A stable and homogeneous microstructure have been obtained after DCT/Tempering. The findings in SEM/X-Ray pictures also reveals a clean and homogeneous microstructure generally (fig. 9-13).

2.5. Hardness

Hardness rates are taken as Rockwell C from 3 different points of samples (19).

Table 5. Hardness Values

Hardness rates of bimetal after DCT		
Low Alloy Steel (HRc)	Interface (HRc)	High Alloy Cast Iron (HRc)
36.6, 37.4, 38.2	49.2, 53.2, 46.7	54.2, 56.5, 55.6
Hardness rates of bimetal after DCT/Tempering		
Low Alloy Steel (HRc)	Interface (HRc)	High Alloy Cast Iron (HRc)
32.3, 31.5, 31.2	42.1, 43.5, 43.3	52.5, 51.3, 50.7

3. Results and discussion

A remarkable and simultaneous grow in the hardness and toughness of the samples subjected to DCT when compared with the previous studies of writer (12,13). Neverthless, after tempering a small fall in hardness is observed. At the same time, a rise in the toughness values is seen obviously.

The SEM and OM images reveals a clear and perfect composition of bimetals (fig.6,10). X-Ray analyse shows also a perfect match and composition of high alloy cast iron and low alloy steel component (fig.7).

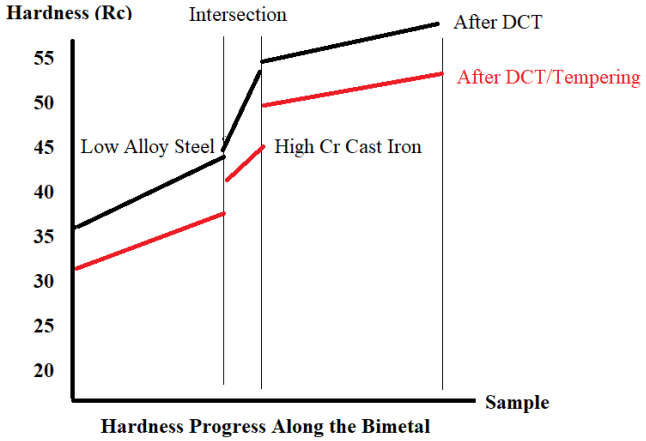

Figure 11. Hardness Progress

It has been observed that the hardness values and toughness values are increased simultaneously after DCT and DCT+Tempering compared with previous results (12,13).

After DCT; hardness rates and impact toughness of the bimetal increase at the same time. We can explain this phenomenon is affected greatly by the uniform distribution of components of the bimetal as seen in X-Ray images (fig.7,8,9).

No defects and casting faults has been observed, so the processes obtained noteworthy results. We can explain this feature is caused by the effect of carbon diffusion and the precipication of eutectic carbides esp. M_7C_3 and $M_{23}C_6$ carbides (fig.9).

In practice, there is a contradiction, that is; hard materials are resistant to abrasion, these materials are, at the same time, not resistant to impacts. This problem is overcome by bimetallic casting; the base part is tough enough to absorb impacts and the working layer is hard and also tough to resist wear and abrasion.

This result is obtained by eutectic carbides esp. M_7C_3 and $M_{23}C_6$ in high chromium cast iron microstructure (fig.9).

4. Conclusions

The study reveals below results in terms of DCT and DCT+Tempering:

1. A good joint and interface is obtained after casting process.
2. A homogeneous combination of two metals have been achieved.
3. It can be observed obviously that microstructure is stable and free from casting defects after DCT+Tempering.
4. Simultaneous increase in hardness and tuoghness after DCT
5. Tempering increases the toughness, sacrificing hardness.
6. A homogeneous distribution of elements is observed as seen in X-Ray analysis
7. Carbides provides a high toughness as well as high hardness related with the Cr amount in bimetal hard side.
8. The potentiality of deep cryogenic treatment of bimetallic castings is conducted and as a result increased toughness and hardness values are obtained as observed in impact tests and hardness rates.

9. The impact toughness values after DCT+Tempering is determined approximately %20 more compared with the rates after DCT.
10. Hardness values decreases appriximately %10 after DCT+Tempering compared with the rates after DCT.

References

1. Zic, S., Dzambas, I., and Ikonic M., Possibilities of Implementing Bimetallic Hammer Castings in Crushing Industries, Metalurgija, **2009**, 48(1):51–54
2. Xiaofeng, X., Shengping, Y., Xiaoguang, Z. and Qiong, X., High Cr White Cast Iron/Carbon Steel Bimetal Liner by Lost Foam Casting with Liquid-liquid Composite Process, China Foundry, **2012**, 9(2):136–142
3. Xiao-Feng, X., Sheng-Ping, Y., Wei-Xin, Y., and Qiong X., HCWCI/Carbon Steel Bimetal Liner by Liquid-Liquid Compound Lost Foam Casting, **2012**, Journal of Iron and Steel Research, International, 19(0):13-19
4. Marukovich, E., Branovitsky, A., Na, Y., Lee J., Choi, K., Study on the possibility of continuous-casting of bimetallic components in condition of direct connection of metals in a liquid state, **2006**, Mater. Des. 27(10):1016–1026
5. Heijkoop, T., Sare, I., Cast-bonding—a new process for manufacturing composite wear products, **1989**, Cast Metals 2(3):160–168
6. Wrobel, T., Ni and Cr base layers in bimetallic castings. In: METAL, 20th Anniversary International Conference on Metallurgy and Materials, May 18–20, (Brno, Czech Republic), Tanger, **2011**: 758–764
7. Wrobel, T., Characterization of bimetallic castings with an austenitic working surface layer and an unalloyed cast steel base, J. Mater. Eng. Perform, **2014**, 23:1711–1717
8. ASM Handbook Volume 4, Heat Treating ASM Handbook, Volume 4A, Steel Heat Treating Fundamentals and Processes. ASM International, ISBN 978-1-62708-011-8, **2013**:382–386
9. Reddy, I., Rao, Dr. Y. S., Seshank, A.S.P and Inturi, V., Characterization and Performance Evaluation of HSS Cutting Tools under Deep Cryogenic Treatment, International Journal of Engineering and Science, **2015**,5(10):13-19
10. Prudhvi, K., and Lakshmi, V.V., Cryogenic Tool Treatment, Imperial Journal of Interdisciplinary Research (IJIR), **2016**
11. Yugandhar, T., Krishnan, P.K. Rao, C.V.B. and Kalidas, R., Cryogenic Treatment and Its Effect on Tool Steel, 6th International Tooling Conference, **2002**, 2:672-683
12. Özdemir, Z., Effect of Heat Treatment on the Impact Toughness of 'High-Chromıum Cast Iron – Low-Carbon Cast Steel' Bi-Metal Components, Metal Science and Heat Treatment, **2017**, 58: 738-741
13. Özdemir, Z., Shallow cryogenic treatment (SCT) effects on the mechanical properties of high Cr cast iron – low-carbon cast steel bimetallic casting, Int. J. Metalcast. **2020**
14. Adin M.Ş., Okumuş M., Investigation of Microstructural and Mechanical Properties of Dissimilar Metal Weld Between AISI 420 and AISI 1018 Steels, Arabian Journal for Science and Engineering, **2022**, 47:8341–8350
15. Adin, M.Ş., Performances of cryo-treated and untreated cutting tools in machining of AA7075 aerospace aluminium alloy, European Mechanical Science, **2023**, 7(2): 70-81
16. Adin, M.Ş., A parametric study on the mechanical properties of MIG and TIG welded dissimilar steel joints, Journal of Adhesion Science and Technology, 202
17. DIN EN 12513:2001, Abrasion Resistant Cast Irons, English Version of DIN EN 12513 (Foreign Standard) **2001**
18. ASTM A27M, Standard Specification for Steel Castings, Carbon, For General Application, **2006**
19. ASTM E18-02, Standard Test Methods for Rockwell Hardness and Rockwell Superficial Hardness of Metallic Materials, **2004**
20. ASTM E23-02, Standart Test Methods for Notched Bar Impact Testing of Metallic Materials, **1982**
21. Totten, G.H., Steel Heat Treatment Metallurgy and Technologies, Second Edition, Portland State University of Portland, **2006**: 148-150
22. Jawahir, I.S., Attia, H., Biermann, D., Duflou, J., Klocke, F., Meyer, D., ... & Umbrello, D., Cryogenic manufacturing processes. CIRP annals, **2016**, 65(2): 713-736

The International Journal of Materials and Engineering Technology (TIJMET) (2023) 6(2)
http://dergipark.gov.tr/tijmet
ISSN: 2667-4033

RESEARCH ARTICLE

The effects of soldering flux type on corrosion properties of electrical wires

Aziz Barış Başyiğit[1], Murat Serdar Ilıcan[2]

[1]Kırıkkale University, Faculty of Engineering and Natural Sciences, Department of Metallurgical and Materials Engineering, Kırıkkale, Türkiye
[2]Kırıkkale University, Faculty of Engineering and Natural Sciences, Department of Mechanical Engineering, Kırıkkale, Türkiye

Article Info

Article history:
Received 24.06.2023
Revised: 17.08.2023
Accepted: 17.08.2023
Published Online: 30.12.2023

Keywords:
UNS C11040
Electrical copper wires
Soldering
Soldering flux
Corrosion resistance

Abstract

Electrical wires are used in many applications with increasing amounts especially in constructions and buildings. These electrical conductive wires are mainly manufactured from 99.9% (by weight) electrolytic copper with restricted minor amounts of other alloying elements. Copper wires are joined by soldering operations for high electrical conducting efficiency. Soldering flux usage is a must in soldering operations where higher corrosion resistance with satisfactory adhesion property is in concern for increasing joining quality. Soldering flux exhibits an important role related with adhesion and corrosion properties of the joints. In this study, three different types of soldering fluxes were used in soldering operation of electrical copper wire. Corrosion test is applied on soldered wires with also unsoldered raw copper wire by immersing in 20%NaOH solution by 96 hours of duration time. Comparison of corrosion resistance of samples is investigated by weight loss principle according to ASTM G1 standard document. The highest corrosion resistance was observed on samples joined with a solder flux of having majorly zinc and ammonium chloride while the least corrosion resistance was observed on samples joined with flux containing halides.

1. Introduction

Electrical wires are composed mainly of electrolytic copper with various elements in limited amounts. They have been used for electrical conductivity purposes in many construction areas [1-5]. These efficient electrical conductor materials are joined by numerous types of soldering and brazing techniques for increasing joining ability and improving electrical conducting performance. Soldering or soft soldering is especially preferred mainly for ensuring electrical conductivity while brazing or hard soldering is applied for also increasing the joint strength as needed.

Solders are mainly composed of lead and tin alloys reacting with the substrates. The most widespread type of solders for soft soldering is approximately %63Sn and remaining amounts of Pb element. This is an eutectic composition as the melting point is too low (≈183°C) for these alloy series between lead and tin letting easier melting in soldering. The products of solder-substrate reactions are composed of inter-metallic compounds such as Cu_3Sn (ε) and Cu_6Sn_5 (η) that can also provide strengthening effect on the joint but letting them responsible for cracks in soldered regions. There are also other types of inter-metallic compounds but they behave less harmful to joint performance as compared with Cu-Sn types.

In soldering, a suitable flux is used for cleaning surfaces from oxides, various dirt and tarnishes etc. The reactions between the solder and the substrate material play an important role on soldering quality.

Non-metallic layers such as oxides originating from atmospheric oxygen, sulfides or other types of contaminations on substrate materials prevents this reaction and obstacles the joining stage. Whether the contaminations are completely removed by using soldering fluxes, the joining reactions between solder and substrate can occur safely. When the flux could not remove all of the surface contamination from the joint faces, the solder will not be able to penetrate fully into the joint and the joint will get weaker. Flux reduces the solid oxide skin and transforms it into a soluble salt. When more amounts of cleaning action are required in some surfaces due to the substrate material, the flux must have more acidic character to accomplish it. Besides the wetting capability of a flux has to be adequate for effective cleaning action, the flux must be at the liquid phase at the soldering temperature for perfect wetting and covering property. Fluxes should retain their mobility during the soldering operation and can be easily removed from the substrate material after cooling when the soldering is completed.

Some fluxes may contain organic and inorganic compounds, resins and halides (as chlorine ions) etc. Natural resin is a distillation product of the sap of pine trees. Chemically, it is a mixture of several organic acids and their close relatives. Halides are composed basically of salts as they can cause corrosion damage in soldering operations so that the joint must be carefully cleaned [6,7].

Table 1. Chemical composition of UNS C 11040 electrical copper wire [1,2]

Elements (%by wt.)							
Cu	Pb	Fe	Ag	As	O	Sb	Te
99.90 (min)	0.0005	0.0010	0.0025	0.0005	0.0650 (max)	0.0004	0.0002

Corresponding Author: Aziz Barış Başyiğit
E-mail: abbasyigit@kku.edu.tr

How to cite this article:
Başyiğit, A.B., Ilıcan, M.S., The effects of soldering flux type on corrosion properties of electrical wires , The International Journal of Materials and Engineering Technology (TIJMET), 2023, 6(2): 46-49

Figure 2. Soldered samples in 20%NaOH corrosion test solution

Hence corrosion is a serious problem in soldering operations arising mainly from fluxes. In this study, samples obtained from UNS C 11040 quality copper electrical wire were soldered by three different types of soldering fluxes. Soldered samples corrosion resistance was tested by immersing in 20%NaOH solution for 96 hours of duration time. Samples weights were observed by a precision scale before and after the corrosion test for determining the weight losses related with corrosion resistance values [8]. A comparison is made for the corrosion rates of samples soldered by 3 different fluxes.

2. Materials and Methods

UNS C11040 type electrolytic copper wire is used in experimental studies. Copper wire samples have the dimensions of Ø3.5x10mm and given in Figure 1.

The copper wire chemical composition data obtained from the manufacturer according to the UNS C11040 document is given in Table 1. The outer plastic cover of the copper wire is removed and finally cleaned before the experimental operations.

Soldering method is applied by a hand soldering iron gun with an operating peak temperature of approximately 250°C. Solders chemical composition according to manufacturer data within ISO 9453 standard document is given in Table 2.

Three types of soldering fluxes were used in soldering operations. Soldering flux is applied before the melting operation of solder for efficient cleaning purposes. Soldering flux technical data are given in Table 3 according to the ISO 9454-1 standard [10]. Soldering fluxes are coded by 1, 2 and 3 instead of their original trade names.

Table 2. Chemical composition of solder wire [9]

Elements (by wt. %)		
Sn	Sb	Pb
62.5-63.5	0.20<	Balance

Table 3. Properties of soldering fluxes used in experimental studies.

	ISO 9454-1	
Flux Code	Ingredients	Condition
1	Zinc and Ammonium chlorides	Pasty
2	Amines and/or ammonia	Semi-solid
3	Resin with Halide activated	Pasty

Figure 1. Experimental electrical copper wire

After the soldering operation, all samples were soft brushed and finally cleaned by pure water. Corrosion test is applied according to ASTM G1 standard document. All soldered samples including the unsoldered raw copper wire were subjected to 20% NaOH test solution with a duration time of 96 hours by holding separately in glasses. All of the samples were weighted by a precision electronic scale having accuracy of 0.0001g before and after the corrosion tests. Soldered samples in 20% NaOH corrosion test solution is given in Figure 2.

Corrosion rates of the samples were estimated by the Equation (1) as indicated in ASTM G1 Standard.

$$Corrosion\ Rate = [K \times W]/[A \times T \times D] \quad (1)$$

K: 8.76×10^4 (constant for mm.year^{-1}),
W: weight loss (g),
A: total surface area of samples (cm^2),
T: time (96 hours),
D: density (8.96 g/cm^3) in Equation 1.

Familiar types of corrosion testing methods such as potentiodynamic polarization, potentiostatic polarization and electrochemical impedance spectroscopy related with soldering have been reported [11]. Corrosion resistance of soldered samples can also be discussed by Energy dispersive spectrometry (EDS) and X-ray diffraction (XRD) methods [12-15]. Salt spray corrosion testing is also reported in soldering [16]. Testing at various corrosive ambient are announced [17]. But in this study corrosion resistance of soldered samples were determined by immersion into the test solution with weight loss principle.

3. Results and Discussion

3.1. Corrosion test results

Weights of soldered samples with raw copper wire before the corrosion test are given in Table 4. Weights of soldered samples with raw copper wire after the corrosion test are given in Table 5. Corrosion rates were estimated according to the weight losses via the Equation 1 and are given in Table 6.

Corrosion test results are graphically summarized in Figure 3. The highest corrosion rate (the least corrosion resistance) was determined on samples joined with Flux 3 while the least corrosion rate (the highest corrosion resistance) was detected on samples joined by Flux 1 as a result of Flux 3 containing halides. Raw copper electrical wire has also exhibited satisfactory corrosion resistance close to samples that joined with Flux 1 among the other types of joined samples. Samples soldered with Flux 2 exhibited also unsatisfactory corrosion resistance among all samples in consequence of having amines. These types of amine containing soldering fluxes have H, C, N, chlorides and bromides owing to make corrosion resistance become worse [6,7].

Table 4. Weights of soldered samples before the corrosion test.

Sample No.	Raw copper wire	Soldered sample with soldering Flux 1	Soldered sample with soldering Flux 2	Soldered sample with soldering Flux 3
1	0,5214	1,5593	2,0838	1,4387
2	0,5213	1,5593	2,0836	1,4385
3	0,5214	1,5592	2,0837	1,4386
Mean Values	*0,52136*	*1,55926*	*2,0837*	*1,4386*

Table 5. Weights of soldered samples after the corrosion test.

Sample No.	Raw copper wire	Soldered sample with soldering Flux 1	Soldered sample with soldering Flux 2	Soldered sample with soldering Flux 3
1	0,5208	1,5590	2,0754	1,4277
2	0,5209	1,5590	2,0753	1,4277
3	0,5208	1,5589	2,0754	1,4276
Mean Values	*0,52083*	*1,55896*	*2,07536*	*1,42766*

Table 6. Corrosion rates of samples

Solder Flux	Mean weights before the corrosion test (g)	Mean weights after the corrosion test (g)	Weight Loss (g)	Surface areas of samples (cm^2)	Corrosion rates ($mm.year^{-1}$)
1	1.55930	1.55896	0.00034	1.290	$3.1x10^{-5}$
2	2.08370	2.07536	0.00834	1.290	$76.2x10^{-5}$
3	1.43860	1.42766	0.01094	1.290	$99.96x10^{-5}$
Raw Wire	0.52136	0.52083	0.00053	1.290	$4.84x10^{-5}$

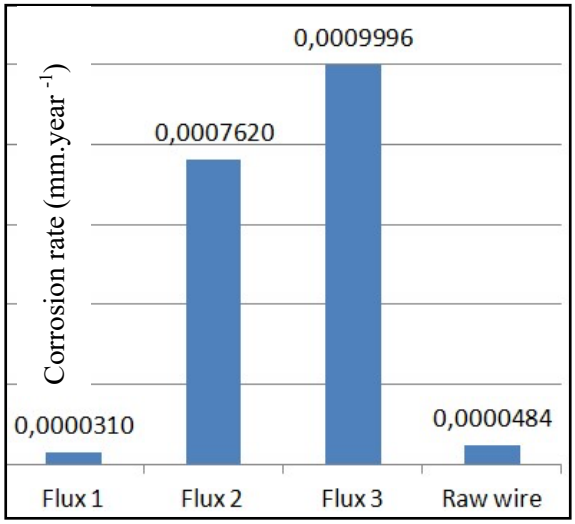

Figure 3. Corrosion test results

4. Conclusions

Corrosion test results revealed that corrosion resistance of copper based samples soldered with Flux types having halides exhibited the highest corrosion rate among all other two types of soldering fluxes. As halides are composed of salts the corrosion resistance is decreased.

The least corrosion rate is observed in samples soldered with zinc and ammonium chloride containing type Flux 1 soldering flux.

Whether corrosion resistance is a must in some copper bearing sensitive electronic or electrical component soldering operations, Flux 1 type zinc and ammonium chloride containing soldering fluxes can be preferred for safer joints.

Author contributions

A. B. Başyiğit: Conceptualization, Data curation, Formal analysis, Investigation, Methodology, Project administration, Resources, Supervision, Writing - original draft, Writing - review & editing

M. S. Ilıcan: Data curation, Formal analysis, Investigation, Resources, Supervision

References

1. Standard Classification of Coppers, ASTM B224, ASTM International. USA, **2022**
2. Standard Specification for Copper Rod for Electrical Purposes, ASTM B49, ASTM International, USA, **2020**
3. Standard Specification for General Requirements for Wrought Copper Alloy Wire, ASTM B250, ASTM International, USA, **2019**
4. Standard Specification for Copper Flat Products with Finished (Rolled or Drawn) Edges (Flat Wire and Strip), ASTM B272, ASTM International, USA, **2019**
5. Standard Specification for Tough-Pitch Fire-Refined Copper, Refinery Shapes, ASTM B 216, ASTM International, USA, **2022**
6. Rudolf S, SMT Soldering Handbook, 2nd Edition, ISBN: 0-7506-35894, Newnes, Butterworth Heinemann, Elsevier, **1998:** 20-60
7. ASM Handbook Committee, Welding Brazing and Soldering, ASM Metals Handbook Volume 6, Electronic Version, ISBN: 0-87170-382-3 USA, **1993**: 270, 453-480,
8. Standard practice for preparing cleaning and evaluation for corrosion test specimens, ASTM G1, ASTM International, USA, **2017**

9. Soft solder alloys-chemical compositions and forms, ISO 9453, International Standards Organization, **2020**
10. Soft soldering fluxes, classification and requirements, Part one, classification, labeling and packaging, ISO 9454-1, International Standards Organization, **2016**
11. Nazeri, F.H.M., et.al., Corrosion characterization of Sn-Zn solder, A Review, Soldering and Surface Mount Technology, **2019,** 31(1): 52-67
12. Asri, A.K., and Hamzah, E., Corrosion behavior of lead free and Sn-Pb solders in 3.5wt% NaCl, Green Technologies for Sustainable and Innovation in Materials, **2013,** 686: 250-260
13. Hu, J, et.al., Electrochemical Corrosion Behaviors of Sn-9Zn-3Bi-xCr Solder in 3.5% NaCl Solution, Journal of Electronic Materials, **2011,** 40(7):1556-1562
14. Grobelny, M., Sobczak, N., Corrosion processes of lead-free solders Sn-Zn type, Ochrona Przed Korozja, **2012,** 55(11):488-490
15. Ning, X., et.al., Effect of some N-heterocyclic inhibitors in the soldering flux on the corrosion behavior of eutectic Sn-58Bi alloy and its solder paste, 19th International Conference on Electronic Packaging Technology, Shangai, China, **2018**
16. Dan, H., Jian, Z., Pei L.P., Corrosion Performance of Pb-free Sn-Zn Solders in Salt Spray, International Conference on Electronic Packaging Technology and High Density Packaging, Proceeding Paper. Shangai, China, **2008**, 2: 713-716
17. Yang, F., Wang, L.H., Li, X.G., Zhao, J., Comparison of corrosion behavior of soldering alloys and joints, Transferability and Applicability of Current Mechanics Approaches, 7th Fracture Mechanics Symposium, Chengdu, China, Proceedings Paper, **2009**:501-506

The International Journal of Materials and Engineering Technology (TIJMET) (2023) 6(2)
http://dergipark.gov.tr/tijmet
ISSN: 2667-4033

RESEARCH ARTICLE

A comparative study on data pre-processing techniques for remaining useful life prediction of turbofan engines

Meryem Erdoğan[1], Muharrem Mercimek[2]

[1]Yildiz Technical University, Department of Avionics Engineering, Istanbul, Türkiye
[2]Yildiz Technical University, Department of Control and Automation Engineering, Istanbul, Türkiye

Article Info

Article history:
Received: 14.11.2023
Revised: 24.12.2023
Accepted: 26.12.2023
Published Online: 31.12.2023

Keywords:
C-MAPSS
LSTM
Wavelet transforms
Savitzky-Golay
EMA
Min-Max
Z-score

Abstract

This study delves into the application of Long Short-Term Memory (LSTM) for predicting Remaining Useful Life (RUL) in Turbofan Engines using the Jet Engine Simulated Dataset (C-MAPSS), systematically examining the combined impact of diverse data pre-processing techniques on RUL prediction, with a particular focus on the application of filtering and normalization. The initial filtering of the dataset employs Savitzky-Golay (SG), wavelet transform, and exponential moving average (EMA) techniques to effectively mitigate noise. Subsequently, minimum-maximum and z-score normalization techniques are implemented. Each filtering method, paired with distinct normalization approaches, is meticulously evaluated, and the performance of LSTM models in RUL prediction is assessed for each combination. The quantitative analysis of experimental outcomes indicates that normalization and filtering contribute to the improvement of the training phase in LSTM models, ultimately enhancing the accuracy of RUL prediction. The study emphasizes that the selection of an optimal data pre-processing structure plays a crucial role in influencing the efficiency of network training, underscoring the potential for optimizing RUL prediction through the application of the LSTM model.

1. Introduction

Today, deep learning and data analytics techniques are widely used to monitor the health status of equipment and optimize predictive maintenance (PdM) in aviation industry. PdM is a maintenance method based on the condition data of the equipment. Based on historical equipment condition data, it predicts when equipment may be damaged in the future. PdM is used to monitor the past health data of equipment and make timely adjustments to the equipment. This is quite a different approach from the routine maintenance methods of the past. PdM saves unnecessary costs, allows for early repairs when equipment reaches the stage of breakdown and increases operational availability of the aircraft. It can prevent unforeseen equipment downtime caused by unexpected failures and improper operation. There are three primary approaches employed for predicting RUL of an equipment: data-driven, physics-based, and hybrid-based. While physics-based and hybrid-based approaches [1, 2] are widely utilized to enhance prediction accuracy, their complexity and demand for in-depth knowledge of aircraft systems render them less cost-effective and less preferable for adoption by airlines and aircraft manufacturers. In the aviation industry, particularly among airlines and aircraft manufacturing companies, a clear inclination exists towards cost-effective methodologies. Specifically, there is a preference for data-driven prognostic approaches over physics-based or hybrid-based alternatives. This preference is grounded in the inherent complexities and knowledge-intensive nature of aircraft systems. In aviation industry prioritizing operational efficiency and cost-effectiveness, the preference is for cost-efficient methodologies such as data-driven prognostic approaches. These strategies leverage data and advanced deep learning models, to deliver precise predictions regarding health of equipment and RUL. Aligned with the industry's commitment to real-time monitoring, predictive maintenance, and cost optimization, the data-driven approach not only tackles challenges associated with overfitting, limited data, and model complexity but also significantly elevates operational reliability.

Various data-driven deep learning models, such as Long Short-Term Memory (LSTM), Convolutional Neural Network (CNN), Feed Forward Neural Network (FNN), Deep Belief Network (DBN), and Graphical Neural Network (GNN), have proven effective in predicting RUL [3-5]. To further optimize model performance and tailor them to specific tasks, various LSTM variants, such as BiLSTM, GRU, Peephole LSTM, and Vanilla LSTM, have also been developed [6]. Ensemble models, such as CNN-LSTM, are also used in RUL prediction, aiming to provide more comprehensive and reliable predictions by leveraging the strengths of different deep learning architectures [1, 6].

To monitor the health of equipment or systems, physical sensors measure various physical parameters, such as temperature, pressure, vibration, power, acoustic wave and speed. Virtual sensors, on the other hand, combine and calculate parameters to provide insights into the equipment or system's health. These parameters can be valuable indicators of equipment or system’s health. For instance, a sudden surge in engine temperature can alert us to a potential issue with the engine's cooling system. Time-series data, collected at regular intervals, captures this valuable information, enabling the monitoring of aircraft systems. Time-series data is especially beneficial because it allows us to identify trends and patterns that may not be evident from a single data point. For example, a

Corresponding Author: Meryem Erdoğan
E-mail: meryemilikosm@gmail.com

How to cite this article:

Erdoğan, M., Mercimek, M., A comparative study on data pre-processing techniques for remaining useful life prediction of turbofan engines, The International Journal of Materials and Engineering Technology (TIJMET), 2023, 6(2):50-58

gradual increase in engine vibration over time could signal wear and tear on the engine's components.

This study aims to enhance the accuracy of RUL estimation by employing sensor data processed through various normalization and filtering techniques as input for the LSTM model. The LSTM model was chosen based on the literature and its success in the field of RUL prediction. The study underscores the direct impact of selecting appropriate data pre-processing methods on the training efficiency of the LSTM model, emphasizing its potential to optimize RUL prediction. It also highlights the pivotal role played by machine learning and data analytics techniques in optimizing health monitoring and PdM for aviation industry. Furthermore, conducting additional investigations and comparisons with other deep learning models and ensemble methods can contribute to the progression of RUL prediction research.Enhancing the accuracy of RUL estimation hinges significantly on the pre-processing of sensor data. The normalization and filtering techniques employed in this stage play a pivotal role in refining the structure of the measured sensor data. These techniques are specifically designed to diminish noise and improve the overall quality of the data. In particular, normalization and filtering methods are extensively utilized to enhance the structure of the measured sensor data and minimize extraneous noise. The SG filtering technique, one among these methods, has found widespread application in various domains for noise reduction in time series data [7-9]. Another effective technique for reducing noise in time series data, such as sensor data or electrocardiogram (ECG) signals indicating heart rhythm, is the wavelet transform method [10-12]. In this method, sensor data is analysed at different scales and frequencies. Noise is usually concentrated in the high frequency components, while the actual sensor measurement data becomes more prominent in the low frequency components. By setting a threshold value, the noise components are detected and the components exceeding the threshold value are filtered out. This process reduces the noise in the sensor measurements while preserving the important components of the actual sensor data. As a result, cleaner and more meaningful data is obtained [13]. Finally, the EMA filtering technique is a method also used for time series data. This technique aims to obtain a smoother trend by reducing sudden fluctuations in the data. It is an effective filtering method to reduce the undesirable effects caused by sudden fluctuations, especially in noisy sensor data [14]. The EMA filtering technique has been successfully applied to sensor data in both the training and test datasets used in RUL prediction studies [15-18].

Normalization is used when sensor data are in different units or scales. Sensor measurement data used for RUL prediction often have different units or scales. For example, one sensor may represent temperature values while another sensor may represent vibration values. These different scales can make it difficult for the deep learning model to accurately learn patterns and relationships. Normalization transforms the data into a specific range or standard distribution, eliminating scale differences and enabling models to produce more consistent and comparable results [19]. In general, minimum-maximum normalization [20-22] and z-score normalization [23, 24] are widely used normalization techniques for RUL prediction. In this study, these widely used normalization and filtering techniques are applied separately and together on sensor data in test and training datasets and their effects on LSTM and RUL prediction performance are compared.

A review of the literature reveals that there are studies comparing only filtering techniques with each other [25, 26] and only normalization techniques with each other [27, 28]. However, this study, which compares normalization and filtering techniques in various combinations and investigates the most effective combined data pre-processing methods for use in LSTM. This study seeks to contribute to the aviation industry by offering practical insights into the prognostic approaches employed for aircraft systems.

2. Data set and methodology

2.1 C-MAPSS dataset

This study employs the C-MAPSS dataset, which comprises simulated data generated by NASA's model-based Turbofan engine degradation simulation program, C-MAPSS [29]. This dataset has subsets as training, test and validation data.

Figure 1 shows the maximum life cycles of 100 engines in the training dataset, along with the frequency of number of engines. Approximately three engines in the dataset were able to operate until the 350th cycle. Nearly 30 engines failed at the 200th cycle and stopped operating. Figure 2 presents the last operated cycles of 100 engines in the test dataset, showing the distribution of engine numbers. The engines are operated until specific cycles, and the NASA-provided test data does not include the exact end-of-life cycle for each engine. This information is provided in the validation dataset, which serves as the actual RUL values for the engines from the test set.

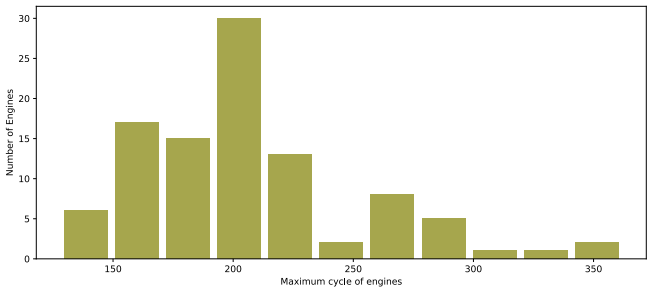

Figure 1 Frequency versus maximum life of engines in train dataset

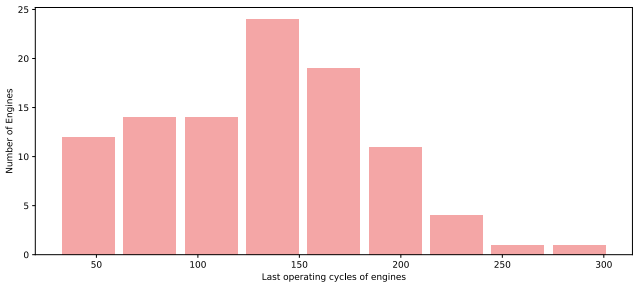

Figure 2 Last operating cycles of engines in test dataset

The size of the training data consists of 20631 rows and 26 columns, while the test data consists of 13096 rows and 26 columns. In both datasets, the column labels are defined as unit ID, cycles, operational setting {1-3} and sensor {1-21}. The unit IDs takes values between 1, 2, ..., 100. The cycle is a unit representing the operating time of each engine in steps. Each cycle contains the measurement values of the sensors used to monitor the health status of the engine. In the training data, there is an association between the cycles and the RUL, as the sensor data is provided until the last operated cycle of the engines'

lifetime, the maximum cycle. RUL values are calculated in this dataset as follows:

$$RUL(t) = Max(t)_{unitID} - t \quad (1)$$

For example, engine 1 or unit ID '1' stopped operating at cycle, *192*, in the training dataset. In this case, unit ID '1' has cycles, *t*, in the range 1, 2, 3, 4, ..., 192. Applying the formula used to calculate the RUL value of the engine at cycle, *t=1*, we obtain *RUL (1) =192-1=191*. A new column containing the calculated RUL values for each cycle has been added to the training dataset. In the training dataset, the RUL values were directly linked to the corresponding sensor values. The RUL values were then fed into the LSTM model as target input without undergoing any data pre-processing. This means that the RUL values were provided to the model in their original form, without any filtering or scaling. The LSTM model was trained on this data, along with the sensor data, to learn the relationship between sensor readings and RUL values. Since the maximum cycles of the engines in the test dataset were not known in advance, sensor data were provided up to a certain cycle and the RUL values at each cycle were attempted to be estimated and evaluated using the validation dataset which includes actual RUL values.

2.2 Filtering techniques

2.2.1 Savitzky-Golay filtering

SG filtering is utilized for smoothing and noise reduction in time-series data, with its parameters, polynomial degree (*l*) and window size (*n*), crucially influencing its performance. In the context of engine sensor data, such as sensor 7 over the initial 175 operating cycles of unit ID '1', a polynomial degree of *4* and a window size of *3* were chosen. The rationale behind these parameter choices is the need to balance noise reduction with responsiveness to changes in the sensor data. A lower polynomial degree and larger window size are preferred for smoother data, whereas data with rapid changes may require a higher degree and smaller window. Visual inspection of the filtered sensor data, as shown in Figure 3, is essential for fine-tuning these parameters to ensure optimal noise reduction without sacrificing important feature trends.

The SG filter estimates the values of a signal in a given range using an approximate polynomial function and then filters the signal using this function. The mathematical formula of the polynomials used in the SG filter is given below:

$$y_t = c_0 + c_1 x_t + c_2 {x_t}^2 + \cdots + c_n {x_t}^n \quad (2)$$

In this study, the SG filtering technique is consistently applied to the entire sensor data, including both the training and test data sets, in various comparison scenarios. For each of the 21 distinct sensors, the measured values at cycle *'t'* are represented as $x_{t1}, x_{t2}, \ldots, x_{t20}, x_{t21}$. Correspondingly, the filtered values for these sensors are designated as $y_{t1}, y_{t2}, \ldots, y_{t20}, y_{t21}$. In this context, y_t represents the processed sensor value predicted by the polynomial to serve as input to the deep learning model, while x_t denotes the raw sensor value. The coefficients of the polynomial, $c_0, c_1, c_2, c_3, \ldots, c_n$, are calculated within the SG filter by minimizing the sum of the squared errors [30].

2.2.2 Wavelet transform

In this investigation, filtering is implemented using the Daubechies wavelet type, incorporating two different parameters for the noise reduction function: the threshold value and the decomposition level. By iteratively adjusting both the decomposition level and threshold value in the wavelet-based noise reduction process, we can navigate the trade-off between removing noise and preserving the data trends. Opting for a higher decomposition level and a lower threshold value can yield a more detailed denoised data, potentially retaining more of the original data but at the risk of keeping more noise. Conversely, choosing a lower decomposition level and a higher threshold value can effectively eliminate noise but may introduce more distortion to the data [13, 31]. This iterative exploration allows for fine-tuning the transform parameters based on the specific characteristics of the data and the desired balance between noise reduction and data fidelity.

Specifically, a threshold of *0.1* and a level of *9* are applied to process all sensors within both the test and training datasets across relevant scenarios. The choice of a threshold value of *0.1* implies a gentle noise reduction process, suitable for data without excessively high noise levels. This cautious approach in thresholding helps avoid distorting the essential structure of the sensor data. Simultaneously, the decision to use a decomposition level of *9* indicates a detailed analysis of the sensor data. The wavelet decomposition breaks down the data into various frequency bands, and this higher decomposition level is motivated by the belief that the data carries valuable information in its high-frequency components. The combined use of a moderate threshold and a high decomposition level seeks a balanced approach, ensuring effective noise removal while preserving the granularity of the original data, a crucial aspect for subsequent analysis.

Illustrated in Figure 4, which showcases the filtering result for a sensor in the training dataset, the figure depicts the measured values of sensor 7 during the initial 175 operating cycles of unit ID '1' alongside the corresponding filtered values over the given cycles.

2.2.3 Exponential moving average (EMA)

EMA filtering is a method for smoothing and reducing noise in time-series data. It works by assigning exponentially decaying weights to past data points, with more recent data points receiving higher weights and older data points receiving lower weights. This approach allows the filter to effectively capture recent changes in the data while also incorporating information from older data.

The EMA filter is typically implemented using the following formula:

$$y_t = \alpha * x_t + (1 - \alpha) * y_{t-1} \quad (3)$$

where:

- y_t is the filtered value at cycle *t*
- x_t is the raw sensor value at cycle *t*
- y_{t-1} is the filtered value at the previous cycle *(t - 1)*
- α is the exponential weighting factor

The values which are belongs to each of the 21 different sensors at cycle *t* are represented as $x_{t1}, x_{t2}, \ldots, x_{t20}, x_{t21}$. Correspondingly, the filtered values for these sensors are designated as $y_{t1}, y_{t2}, \ldots, y_{t20}, y_{t21}$.

The exponential weighting factor α determines the relative importance of recent and historical data. A higher α value prioritizes more recent data, effectively capturing real-time

changes in the data. Conversely, a lower α value emphasizes older data, enabling the preservation of longer-term trends [32].

In this study, the exponential weighting factor α is set to *0.7*. This chosen value strikes a delicate balance, effectively blending recent and historical data. By setting α to *0.7*, the filter is designed to prioritize more recent information while still incorporating valuable insights from older cycles. This approach ensures an effective smoothing of the sensor data while preserving the data trends.

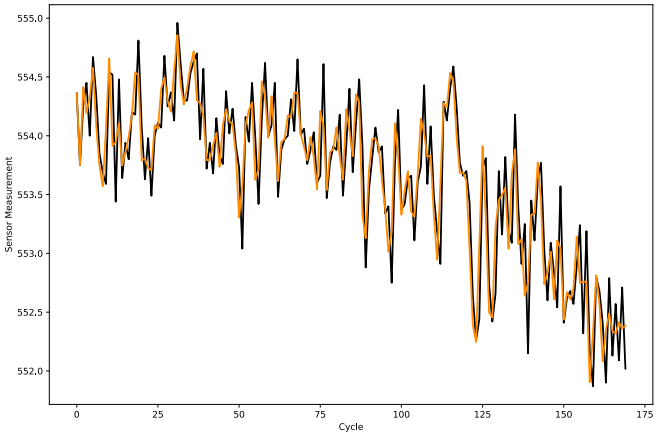

Figure 3 Noise reduction with Savitzky-Golay on Sensor 7

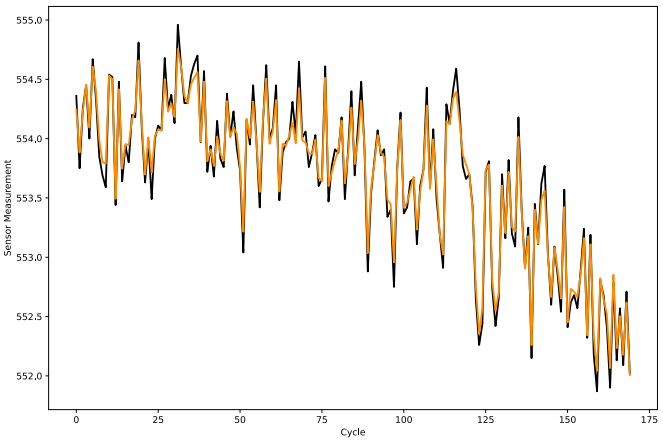

Figure 4 Noise reduction with wavelet transform on Sensor 7

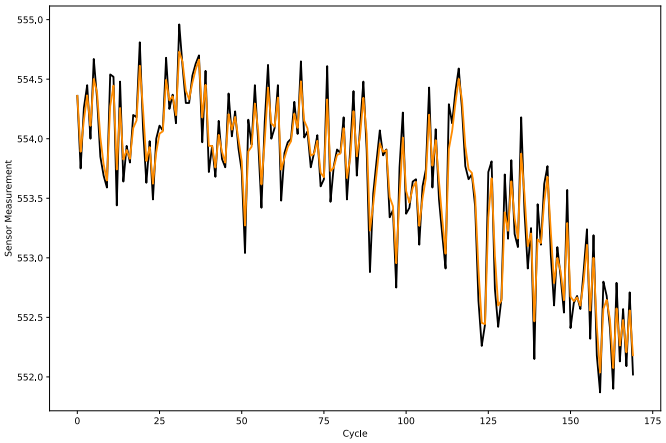

Figure 5 Noise reduction with EMA on Sensor 7

As an illustration, Figure 5 shows the filtering result for a sensor within the training data set. The figure shows the values of sensor 7 measured during the first 175 operating cycles of unit ID '1', alongside the filtered values over the cycles.

2.3 Normalization techniques

Minimum-maximum normalization is a method used to transform data into a specific range. This method compresses data values into a range of values between 0 and 1, independent of their original range. Its mathematical formula can be shown as follows [19]:

$$y_t = \frac{x_t - \min(x_t)}{max(x_t) - min(x_t)} \quad (4)$$

Where x_t is the sensor data and y_t is the normalized sensor data at cycle, *t*. $min(x_t)$ and $max(x_t)$ represent the minimum and maximum sensor values at cycle, *t*.

The z-score normalization involves subtracting the mean of sensor data at time cycle, *t* and dividing this difference by the standard deviation. This method normalizes the sensor data for each cycles using the following formula [19]:

$$y_t = \frac{(x_t - \mu)}{SD} \quad (5)$$

Where y_t is the normalized sensor data at cycle, *t and* x_t is the raw sensor data at cycle, *t*. μ is the mean of the sensor data over all time cycles and *SD* is the standard deviation of these values. For 21 different sensors, the measured values at cycle *t*, are denoted as $x_{t1}, x_{t2}, \ldots, x_{t20}, x_{t21}$. The normalized values of these sensors are also denoted as $y_{t1}, y_{t2}, \ldots, y_{t20}, y_{t21}$. In this study, all sensors in both the training and test datasets are normalized for the relevant scenarios using minimum-maximum with the range between {0, 1} and z-score normalization techniques.

2.4 Long-short-term memory networks (LSTM)

LSTM models are the most widely used choice for RUL prediction using time series data due to their ability to handle sequential data, capture long-term dependencies, resist noise, adapt to different RUL prediction scenarios and continuously improve through learning [35]. These characteristics make LSTM models powerful techniques for accurately predicting the RUL of equipment, enhancing its reliability, and optimizing PdM management.

When the LSTM is analysed structurally, the representation of the internal structure of the cell is given in Figure 6.

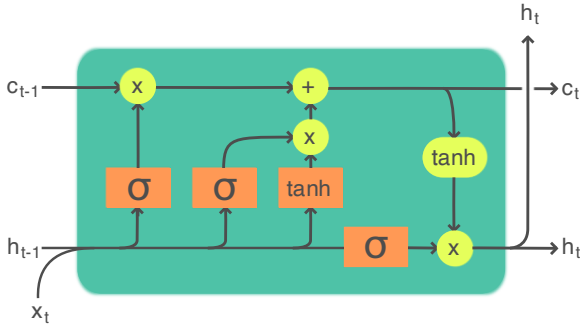

Figure 6 An illustration of the internal structure of the LSTM cell [33]

The LSTM network computes unit activations based on a given input across a time cycle. These activations are regulated

by the gates and cell states within the network. The following equations define the activations of the LSTM units;

$$\begin{aligned} g_t &= tanh(W_g * [h_{t-1}, x_t] + b_g) \\ i_t &= (W_i * [h_{t-1}, x_t] + b_i) \\ f_t &= \sigma(W_f * [h_{t-1}, x_t] + b_f) \\ o_t &= \sigma(W_o * [h_{t-1}, x_t] + b_o) \\ c_t &= f_t * c_{t-1} + i_t * g_t \\ h_t &= o_t * tanh(c_t) \end{aligned} \quad (6)$$

Within the LSTM algorithm, the arrays *i, f, o* and *c*, denoting the input gate, forget gate, output gate and cell activation, are central components of the cell. These arrays, of the same size as the hidden array *h*, carry essential information. The *W* terms correspond to the weight matrices governing the gate sequences within the cell structure.

Conventionally, an activation function such as *tanh* is applied in the output layer of the LSTM configuration. These equations describe the gating activations within the LSTM units that influence the cell state updates. Consequently, the LSTM network establishes connections by processing inputs across time cycles and using memory mechanisms to capture sequential data patterns [34].

In Equation (6), x_t is the input to the LSTM model and in this study, the raw sensor data is referred as x_t, and the processed sensor data is referred as y_t.

This study aims to investigate the effect of different filtering and normalisation techniques on the performance of the LSTM model using the C-MAPSS dataset. In order to compare the data pre-processing techniques in different scenarios, the hyper-parameters of the LSTM model were set to be the same for all scenarios. These hyper-parameters are given in Table 1.

Table 1. LSTM model hyper-parameters

Hyper-parameter	Value
Number of LSTM layers	3
Number of dense layers	3
Learning speed	0.01 & 0.001
Activation function	tanh
Number of trainings	10
Batch size	64
Optimizer	Adam

The root mean square error (RMSE) performance metric and Pearson correlation coefficient (PCC) were used to evaluate the performance of the LSTM models. The mathematical expressions of RMSE and PCC are given in Equation (7) and Equation (8) respectively.

$$RMSE = \sqrt{\frac{1}{N}\sum_{i=1}^{N}(y_i - \hat{y}_i)^2} \quad (7)$$

$$PCC = \frac{\sum_{i=1}^{N}\left(y_i - \mu_{y_i}\right)\left(\hat{y}_i - \mu_{\hat{y}_i}\right)}{\sqrt{\sum_{i=1}^{N}\left(y_i - \mu_{y_i}\right)^2}\sqrt{\sum_{i=1}^{N}\left(\hat{y}_i - \mu_{\hat{y}_i}\right)^2}} \quad (8)$$

In Equation (7) and Equation (8), y_i represents the actual RUL value for observation *i*, $\hat{y}_i$ represents the predicted RUL value and *N* represents the number of observations. The RMSE is commonly used to calculate the error between the actual and predicted values and to evaluate the predictive performance of the model. Lower RMSE values indicate that the model makes better predictions and fewer errors. Higher values indicate poor performance of the model.

The PCC value is between -1 and 1 and represents the similarity between the actual and predicted values. Its interpretation is as follows;

- If PCC is close to -1: There is a strong negative relationship. It indicates an inverse relationship between actual and predicted values. One variable increases while the other decreases.
- If the PCC is close to 1: There is a strong positive relationship. Indicates a direct relationship between actual and predicted values. When one variable increases, the other also increases.
- When PCC outputs NaN (invalid number): This indicates that there are not enough predicted values for the PCC to be calculated or that the predicted values have the same value.

3. Findings and discussion

In this study, different scenarios with different combinations of data pre-processing techniques were developed and applied to a same LSTM model. The aim of the experiments was to carefully investigate and evaluate the effectiveness of different data pre-processing combinations in improving the accuracy of RUL predictions using a LSTM model, ultimately identifying the optimal pre-processing strategies that lead to the most accurate RUL estimates. The labels for the scenarios are provided in Table 2, while the defined combinations of scenarios being compared and labels are listed in Table 3.

Table 2. Labels for scenarios

Script Label	Techniques
SN1	Raw data + LSTM
SN2	Raw data + SG filter + LSTM
SN3	Raw data + wavelet transform + LSTM
SN4	Raw data + EMA + LSTM
SN5	Min-max normalization + LSTM
SN6	SG filter + Min-max normalization + LSTM
SN7	Wavelet transform + Min-max normalization + LSTM
SN8	EMA + Min-max normalization + LSTM
SN9	Z-score normalization + LSTM
SN10	SG filter + Z-score normalization + LSTM
SN11	Wavelet transform + Z-score normalization + LSTM
SN12	Z-score normalization + EMA + LSTM

Table 3. Comparative scenarios and labels

Comparative Scenario Label	Scenarios
comparativeSN_1	SN2, SN3, SN4
comparativeSN_2	SN6, SN7, SN8
comparativeSN_3	SN10, SN11, SN12
comparativeSN_4	SN1, SN5, SN9
comparativeSN_5	SN2, SN6, SN10
comparativeSN_6	SN3, SN7, SN11
comparativeSN_7	SN4, SN8, SN12

While defining the comparative scenarios, we wanted to determine the best filtering technique (comparativeSN_1) applied to the raw sensor data. In addition, the best filtering technique when applied with the minimum-maximum normalization method (comparativeSN_2) and the best filtering

technique when applied with the z-score normalization technique (comparativeSN_3) were investigated. In addition, the impact of the normalization technique on the performance of the LSTM model is investigated in the comparative scenarios, comparativeSN_4, comparativeSN_5, comparativeSN_6 and comparativeSN_7.

3.1 Impact of normalization techniques on the performance of the LSTM model

In order to evaluate the performance of normalization techniques on the LSTM model, different comparative scenarios were determined and the results were compared (Table 4, Table 5, Table 6 and Table 7). In the comparative scenarios, LSTM models are trained using raw sensor data, minimum-maximum and z-score normalized sensor data with different filtering techniques and model performances are compared with RMSE and PCC metrics.

According to the results obtained and the prediction-actual RUL value graphs, in scenarios where no normalization technique is applied (e.g., Figure 7) the model outputs have high RMSE values and there is no correlation between actual and predicted RUL values in the graphs.

When the LSTM model is trained using processed data through normalization techniques and raw data without any filtering methods, insights from Table 4 and Figure 10 reveal the following: the most efficient scenario emerges when normalized data is employed with the z-score normalization method.

When the best normalization technique was investigated in combination with the SG filtering technique, it was observed that the z-score normalization technique had a more positive effect on the performance of the LSTM model compared to minimum-maximum normalization (Figure 9 and Table 5).

When the best normalization technique was investigated in combination with the wavelet transform technique, it was observed that the minimum-maximum normalization technique had a more positive effect on the performance of the LSTM model compared to z-score normalization (Figure 11 and Table 6).

When the best normalization technique was investigated to be applied together with EMA, it was observed that the z-score normalization technique had a more positive effect on the performance of the LSTM model compared to minimum-maximum normalization (Figure 12 and Table 7).

According to the results of all comparative scenarios, the technique with the most positive effect on the performance of the LSTM model was observed as the z-score normalization method.

In a study, investigation of normalization techniques across various time series datasets was conducted to explore alternatives to the commonly favoured z-score normalization method [28]. Z-score normalization is typically the preferred [23, 24] choice over minimum-maximum normalization for most applications due to its greater robustness, versatility, and overall effectiveness. Z-score normalization's ability to handle outliers, preserve distribution shape, and ensure equal scaling across features makes it suitable for a wide range of analytical tasks. However, min-max normalization remains useful when there is a specific need to preserve the original data range, and its simplicity and faster application make it a viable option in certain scenarios. The choice between the two methods ultimately depends on the specific requirements and characteristics of the data in a given application.

Table 4. comparativeSN_4 result

Scenarios	RMSE	PCC
SN1	41.78	NaN
SN5	15.80	0.9314
SN9	14.81	0.9223
	The best scenario, SN9	The best scenario, SN9

Table 5. comparativeSN_5 result

Scenarios	RMSE	PCC
SN2	42.03	NaN
SN6	15.45	0.9201
SN10	13.57	0.9466
	The best scenario, SN10	The best scenario, SN10

Table 6. comparativeSN_6 result

Scenarios	RMSE	PCC
SN3	42.10	NaN
SN7	22.70	0.8503
SN11	24.18	0.8374
	The best scenario, SN7	The best scenario, SN7

Table 7. comparativeSN_7 result

Scenarios	RMSE	PCC
SN4	42.04	NaN
SN8	15.32	0.9301
SN12	14.28	0.9393
	The best scenario, SN12	The best scenario, SN12

Table 8. comperativeSN_1 result

Scenarios	RMSE	PCC
SN2	42.03	NaN
SN3	42.10	NaN
SN4	42.04	NaN
	The best scenario, SN2	

3.2 Effect of filtering techniques on the performance of the LSTM model

In order to evaluate the performance of the filtering techniques on the LSTM model, several comparative scenarios were defined and the results were compared (Table 8, Table 9 and Table 10). In the comparison scenarios with defined combinations, the raw sensor data and normalised sensor data were filtered using SG, wavelet transform and EMA techniques. The performance of the LSTM models trained on these filtered data is compared using the RMSE and PCC metrics.

The performance of the LSTM model with raw sensor data, as depicted in Table 8 and Figure 7, demonstrates poor results. Elevated RMSE values indicate significant predictive errors, while the stark dissimilarity between the actual and predicted graphs underscores the model's inability to effectively capture the underlying patterns within the sensor data.

Examining the scenarios using SG, wavelet transform, and EMA filtering on the minimum-maximum normalized sensor data, it became evident from Table 9 that SN8 stood out as the most effective approach. Specifically, applying EMA filtering with the minimum-maximum normalization technique produced the most favourable results, as evidenced in Figure 8. Furthermore, SN6 and SN7, employing different filtering techniques, demonstrated relatively low RMSE values and notably strong correlations in their respective plots.

Upon reviewing Table 10, it became evident that among the scenarios applying SG, wavelet transform, and EMA filtering techniques to sensor data, normalized using the z-score method, SN10 emerged as the most effective (as shown in Figure 9). Specifically, utilizing the SG filter on the sensor data normalized with the z-score method yielded the most optimal outcome. Additionally, it's worth noting that EMA filtering technique, as seen in SN12, showcased comparable result.

After assessing how filtering and normalization techniques impacted the LSTM model's performance, we can now contrast the scenarios that yielded the best results. Table 11 presents a comparison of these top-performing scenarios.

Upon analysis in Table 11, SN8, SN9, SN10, and SN12 displayed remarkably close RMSE and PCC values, indicating successful outcomes. Notably, the LSTM model trained using the SG technique in tandem with z-score normalization method emerged as the optimal scenario, showcasing the lowest RMSE and the highest PCC. Nevertheless, the results derived from implementing the wavelet transform and EMA filtering also showed a positive influence on the LSTM model's performance. This observation suggests that optimizing the LSTM model, fine-tuning filtering techniques, as well as employing wavelet transform or EMA techniques, can lead to optimal performance results, proving to be viable methods.

Table 9. comperativeSN_2 results

Scenarios	RMSE	PCC
SN6	15.45	0.9201
SN7	22.70	0.8503
SN8	15.32	0.9301
	The best scenario, SN8	The best scenario, SN8

Table 10. comparativeSN_3 results

Scenarios	RMSE	PCC
SN10	13.57	0.9466
SN11	24.18	0.8374
SN12	14.28	0.9393
	The best scenario, SN10	The best scenario, SN10

Table 11. Comparing the most effective scenarios

Scenarios	RMSE	PCC
SN7	22.70	0.8503
SN8	15.32	0.9301
SN9	14.81	0.9223
SN10	13.57	0.9466
SN12	14.28	0.9393
	The best scenario, SN10	The best scenario, SN10

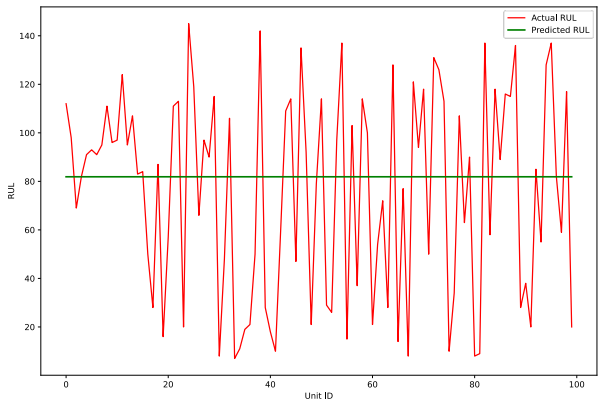

Figure 7 The most effective scenario, denoted as SN2, evaluated within the context of the comparativeSN_1

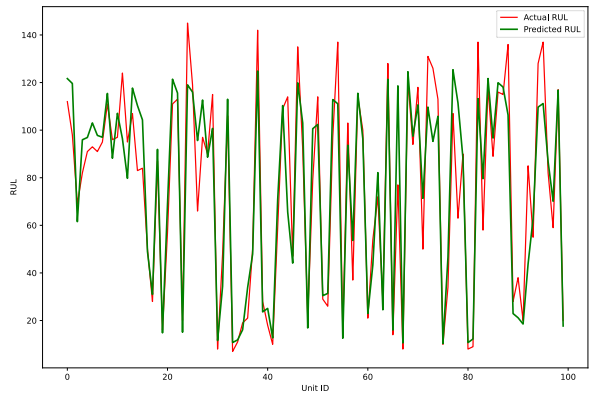

Figure 8 The most effective scenario, denoted as SN8, evaluated within the context of the comparativeSN_2

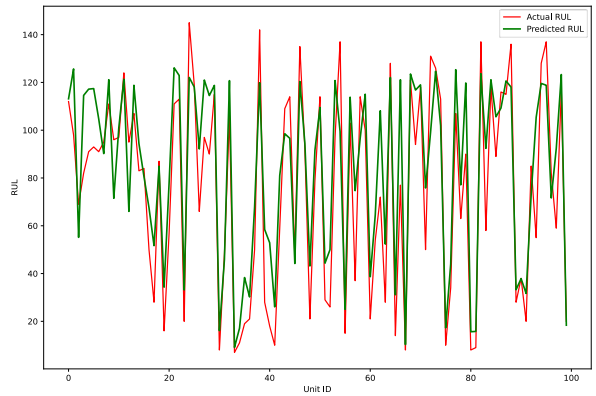

Figure 9 The most effective scenario, denoted as SN10, evaluated within the context of the comparativeSN_3 and comparativeSN_5

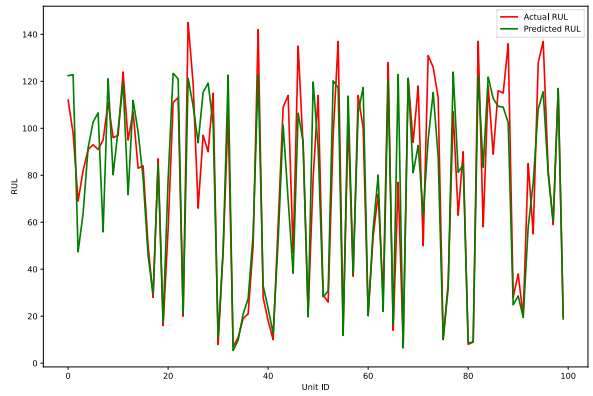

Figure 10 The most effective scenario, denoted as SN9, evaluated within the context of the comparativeSN_4

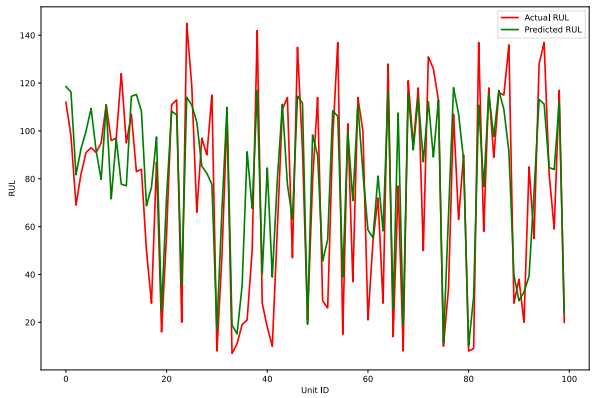

Figure 11 The most effective scenario, denoted as SN7, evaluated within the context of the comparativeSN_6

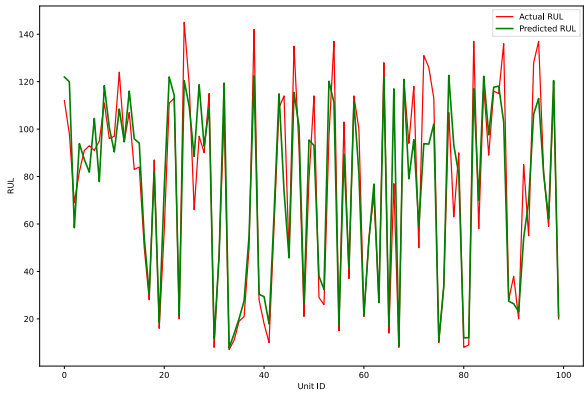

Figure 12 The most effective scenario, denoted as SN12, evaluated within the context of the comparativeSN_7

4. Results

The ability to accurately predict the RUL of equipment is crucial for PdM maintenance and asset management strategies. LSTM networks have emerged as powerful tools for RUL prediction, but their performance can be significantly impacted by the quality of the input data. This study delved into the impact of different data pre-processing techniques on the performance of LSTM model for RUL prediction, focusing on the C-MAPSS dataset, a benchmark for prognostics research.

Raw sensor data often exhibits inherent noise, non-stationarity, and various scales, which can hinder the LSTM model's ability to learn meaningful patterns and make accurate predictions. Data pre-processing techniques, such as normalization and filtering, play a critical role in preparing the data for effective model training and prediction. Normalization techniques like z-score normalization standardize the data within a specific range, ensuring that all features contribute equally to the model's learning process. Filtering techniques, on the other hand, aim to reduce noise and smooth out the data, allowing the LSTM model to focus on the underlying patterns rather than spurious fluctuations.

The study systematically evaluated the impact of various data pre-processing combinations on the LSTM model's performance. The results indicated that directly using raw data yielded suboptimal performance, with higher RMSE and lower PCC values. Conversely, employing normalization techniques consistently improved the model's performance, effectively scaling the data and enhancing its learning capabilities.

Among the normalization techniques, z-score normalization consistently demonstrated the best performance, reducing RMSE and enhancing PCC values. When combined with SG filtering, a technique specifically designed for time series data, the model achieved the lowest RMSE and highest PCC values, showcasing the synergistic effect of normalization and filtering. This dual approach effectively standardized the data and simultaneously reduced noise, leading to more accurate and consistent RUL predictions.

Beyond z-score normalization and SG filtering, the study also explored the effects of other filtering techniques, including wavelet transform and EMA. Both techniques demonstrated positive impacts on the LSTM model, further improving its ability to handle noisy data and produce reliable RUL predictions. Wavelet transform decomposed the data into different frequency bands, allowing the model to focus on the most relevant features, while EMA smoothed out short-term fluctuations and emphasized long-term trends.

The findings of this study underscore the significance on combination of data pre-processing in enhancing the performance of LSTM models for RUL prediction. By carefully selecting and combining appropriate normalization and filtering methods, researchers can significantly improve the accuracy and robustness of their models. Furthermore, applying these methods to other time series datasets and conducting comparative analyses can provide further insights into the optimal data pre-processing combinations for RUL prediction.

Author contributions

Second author contribution statement: Conceptualization, Methodology, Supervision, Validation, Review

References

1. Khaled, A., A Hybrid Deep Learning Based Approach for Remaining Useful Life Estimation, IEEE International Conference on Prognostics and Health Management (ICPHM), **2019**
2. Manuel, A.C., Fusing physics-based and deep learning models for prognostics, Reliability Engineering & System Safety, **2022**, 217, 107961
3. Zhu, K., Zhang, C., Data-driven RUL Prediction of High-speed Railway Traction System Based on Similarity of Degradation Feature, 9 CAA Symposium on Fault Detection, Supervision and Safety for Technical Processes (SAFEPROCESS), July 05-07, **2019**
4. Dong, D., Li, X.Y., Life Prediction of Jet Engines Based on LSTM-Recurrent Neural Networks, Prognostics and System Health Management Conference (PHM-Harbin), **2017**
5. Zhang, Y.Z., Xiong, R., A LSTM-RNN method for the lithuim-ion battery remaining useful life prediction, Prognostics and System Health Management Conference (PHM-Harbin), **2017**
6. Cui, J., Wang, Y., Prediction of Aeroengine Remaining Useful Life Based on SE-BiLSTM, 34th Chinese Control and Decision Conference (CCDC), **2022**
7. Xiaoxiong, W., Mingyang, P., and Chunxiao, X., Water Level Data Preprocessing Method Based on Savitzky-Golay Filter, International Conference on Modeling, Simulation and Big Data Analysis (MSBDA), **2019**
8. Lulu, W., Xiaoming, W., Hongbin, W., Data-driven SOH Estimation of Lithium-ion Batteries Based on Savitzky-Golay Filtering and SSA-SVR Model, IEEE 4th International Conference on Smart Power & Internet Energy Systems, **2022**

9. Lingyun, S., Ningyun, L., Xianfeng, M., Equipment Health State Assessment Based on MIC-XGBoost, The 13th Asian Control Conference (ASCC), **2022**
10. Honglin, L., and Wang, J., Based on Wavelet Threshold Denoising-LDA and Bilstm Aircraft Engine Life Prediction, Journal of Phys. Conf. Ser., **2022**
11. Rai, A., Upadhyay, S.H., The use of MD-CUMSUM and NARX neural network for anticipating the remaining useful life of bearings, Measurement 111, **2017**, 397–410
12. Harender, Dr. R. K. Sharma, EEG Signal Denoising based on Wavelet Transform, International Conference on Electronics, Communication and Aerospace Technology ICECA
13. Daubechies, I., Ten Lectures on Wavelets, SIAM **1992**
14. Kopuru, M.S.K., Rahimi, S., Recent Approaches in Prognostics: State of the Art, CSCE, **2019**
15. Nie, L., Xu, S., Remaining Useful Life Prediction of Aeroengines Based on Multi-Head Attention Mechanism, Machines, **2022,** 10(7):552
16. Yan, H., Zuo, H., Two-Stage Degradation Assessment and Prediction Method for Aircraft Engine Based on Data Fusion, Hindawi International Journal of Aerospace Engineering, **2021**:1-16
17. Ye, Z., Yu, J., Health condition monitoring of machines based on long short-term memory convolutional autoencoder, Applied Soft Computing, **2021**, 107:107379
18. Costa, N., Sánchez, L., Variational encoding approach for interpretable assessment of remaining useful life estimation, Reliability Engineering and System Safety 222, **2022**:108353
19. Han, J., & Kamber, M., Data Mining: Concepts and Techniques. Morgan Kaufmann, **2011**
20. Li, J., Jia, Y., Remaining Useful Life Prediction of Turbofan Engines Using CNN-LSTM-SAM Approach, IEEE Sensors Journal, **2023**, 23(9)
21. Olariu, E.M., Portase, R., Predictive Maintenance-Exploring strategies for Remaining Useful Life (RUL) prediction, IEEE 18th International Conference on Intelligent Computer Communication and Processing (ICCP), **2022**
22. De Pater, I., Mitici, M., Developing health indicators and RUL prognostics for systems with few failure instances and varying operating conditions using a LSTM autoencoder, Engineering Applications of Artificial Intelligence, **2023**, 117:105582
23. Ruan, D., Wu, Y., Remaining Useful Life Prediction for Aero-Engine Based on LSTM and CNN, 33rd Chinese Control and Decision Conference (CCDC), **2021**
24. Zhu, Y., Liu, Z., Aircraft engine remaining life prediction method with deep learning, International Conference on Artificial Intelligence and Computer Information Technology (AICIT), **2022**
25. Kumari, S., Kumar N., and Rana, P.S., Comparative Performance Study of Different Filtering Techniques with LSTM for the Prediction of Power Consumption in Smart Grid, IETE Journal of Research, **2023**
26. Jongwoo, B., Filtering Correction Method and Performance Comparison for Time Series Data, Journal of information and communication convergence engineering **2022**, 20(2):125-130
27. Singh, N., Singh, P., Exploring the effect of normalization on medical data classification, International Conference on Artificial Intelligence and Machine Vision (AIMV), **2021**
28. Lima, F.T., A Large Comparison of Normalization Methods on Time Series, Big Data Research **2023,** 34:100407
29. Saxena, A., Goebel, K., Simon D., Eklund, N., Damage propagation modeling for aircraft engine run-to-failure simulation, International Journal of Prognostics and Health Management, **2008**, 1(1):9
30. Savitzky, A.G., M.J.E., Smoothing and differentiation of data by simplified least squares procedures, Analytical Chemistry, **1964**, 36(8):1627-1639
31. Hu, W., and Zhao, S., Remaining useful life prediction of lithium-ion batteries based on wavelet denoising and transformer neural network, Front. Energy Res., **2022**, 10:969168
32. de Miranda, A. R., de Andrade Barbosa, T.M., Conceiçao, A.G.S., Alcalá, S.G.S., Recurrent Neural Network Based on Statistical Recurrent Unit for Remaining Useful Life Estimation, 8th Brazilian Conference on Intelligent Systems (BRACIS), **2019**
33. Chevalier, G., LARNN: Linear Attention Recurrent Neural Network, **2018**
34. Hochreiter, S., Schmidhuber, J., Long Short-Term Memory, Neural Computation, **1997**, 9(8)
35. Berghout, T., Benbouzid, M., A systematic guide for predicting remaining useful life with machine learning, Electronics, **2022**, 11(7):1125

The International Journal of Materials and Engineering Technology (TIJMET) (2023) 6(2)
http://dergipark.gov.tr/tijmet
ISSN: 2667-4033

RESEARCH ARTICLE

Investigation of compatibility of AL5182 series sheets with DP800 series sheets by CMT method

Cihan Yakupoğlu[*1], Ufuk Öztürk[1], İbrahim Acar[2] and Faruk Varol[2]

[1]*Akpres Metal Yedek Parça Mak. San. Ve Tic. A.Ş, Centre of Research & Development, Sakarya, Türkiye*
[2]*Sakarya University of Applied Sciences University, Vocational School of Karasu, Sakarya, Türkiye*

Article Info

Article history:
Received 09.12.2023
Revised: 21.12.2023
Accepted: 26.12.2023
Published Online: 31.12.2023

Keywords:
DP800 steel
Al5182
Cold metal transfer
ER4043

Abstract

In this study, 1 mm thick DP800 (Double Phase) galvanized coated steel sheets used in the production of automotive body and chassis parts were combined with 1.5 mm thick Al 5182 series sheets. These connections were made using the cold metal transfer (CMT) method of gas arc welding. The applied welding position is determined as the overlap. This application was carried out in a fully automatic robotic system using 1 mm diameter aluminum-based ER4043 (AlSi5) filling wire. After joining processes with the cold metal transfer (CMT) method, tensile strength (MPa), bending test, hardness values (HV), macro and micro tests in the joining areas were examined. In conclusion, the maximum breaking strength was reached at 90 amps (Fm: 4.28 kN). It was observed that heat input affected the intermetallic (IMC) phase formation and thickness. In bending tests, the highest breaking force (295 N) was reached at 85 amperes. Negative effects of evaporative galvanization (incomplete melting, pore formation) were observed in Al-DP steel joints. It was observed that the melting of aluminum positively affected the wetting angle in galvanization.

1. Introduction

Weight reduction in the automotive sector is of great importance for the goals of reducing fuel consumption and CO2 emissions. Therefore, the use of unalloyed and ultra-high strength steels for durability has greatly increased. Non-ferrous light metal alloys and Al alloys are used in vehicle production due to their strength-to-weight ratio. Different materials such as steel and Al alloys are present in vehicle body structures, but the welded joining process of these different materials is of great importance. CMT (cold metal transfer), waveform controlled cold arc, pulsed double electrode gas arc and AC pulsed gas arc welding methods have been developed for the welding of thin sheet metal parts. These developed methods have been investigated in the application of joining different metals such as aluminum and steel. in many cases, galvanized steel has been used as steel base material [1-4]. The steel sheet has a Zn coating layer to prevent oxidation. In the case of hard-seam welding, the Zn in the Zn-coated material used may remain outside the joint. In recent studies, uncoated steel or aluminized steel [5-8] has been preferred over Zn-coated steel for joining dissimilar metals. In uncoated steels, the joining process is not suitable due to insufficient wetting due to oxidation. Babu et al. (2018) studied the feasibility of joining aluminum alloy (AA 2219) with austenitic stainless steel (AISI 321) in an overlap configuration was investigated using a hybrid fabrication route consisting of friction surfacing and cold metal transfer (CMT) welding. Friction surfacing of aluminum on stainless steel followed by CMT welding was found to be a promising approach for joining aluminum with stainless steel in overlap configuration [9]. Madhavan et al. (2016) studied the to join A6061-T6 aluminum alloy to Dual Phase 800 steel using AlSiMn filler by cold metal transfer (CMT) processes. Revealed the presence of elongated plate shape (Al5FeSi) and fragmented particles in the IM layer, found that welding currents and arc length correction factor have significant effects on joint strength and that tensile rupture occurs in the heat affected zone [10]. Singh et al. (2020) studied the new CMT+P brazing process was used to join aluminum (AA5052) and steel (DP780) in the lap position with increasing Al sheet thickness and found that the wettability and strength of CMT brazed joints decreased due to the gradual decrease in interfacial area with increasing Al thickness due to faster heat dissipation from molten filler [11].

In this study, the mechanical strength values and bending forces of the joints were determined by CMT joining method using a 1 mm diameter weld zone in the lap joint of 1 mm thick DP800 (Dual Phase) steel sheet and 1.5 mm thick Al 5182 sheet. ER4043 (AlSi5) filler wire was used. Hardness values in the weld zone were observed with varying welding current, the thickness of the formation of intermetallic structures of alloying elements (Al-FE-Si etc.) with heat and the effect of this formation and thickness on strength, the effect of zinc layer on wettability in the weld pool and structural properties in the joint with different amperage values (75A, 80A, 85A, 90A, 95A, 100A, 105A) were observed.

2. Materials and methods

2.1. Materials used in the experiments

DP800 galvanized steel and Al 5182 sheet were used as test materials in the experiments. The steel sheet is 1 mm thick and 12-14 micron (45-60 g/m2) galvanized on both surfaces. Al 5182 (AL5- HDI-TZ-U) sheet metal was chosen with a

Corresponding Author: Cihan Yakupoğlu
E-mail: cihan.yakupoglu@akpres.com.tr

How to cite this article:
Yakupoğlu, C., Öztürk, U., Acar, İ.,Varol, F., Investigation of Compatibility of Al5182 Series Sheets with DP800 Series Sheets by CMT Method, The International Journal of Materials and Engineering Technology (TIJMET), **2023**, 6(2):59-65

thickness of 1.5 mm. ER4043 (AlSi5) was used as filler wire. Chemical properties of the materials used are shown in Table 1, and mechanical properties are shown in Table 2.

Table 1. Chemical properties of the materials used (%)

Material	Fe	C	Si	Mn	Zn	Ti	Al
DP800	97	0,15	0,46	1,65	0,02	0,01	0,03
AL5182	0,19	-	0,10	0,37	0,01	0,02	99
ER4043	0,5	-	5	0,03	-	0,01	94

Table 2. Mechanical properties of test specimens and filler wire

Material	Yield stresses (σAk)	Tensile strength (σmax)	Elongation (%)	Hardness (Hv)
DP800	620 MPa	830 MPa	15	220
AL5182	160 MPa	282 MPa	23	-
ER4043	115 MPa	145 MPa	15	-

2.2. Method applied

The joints were made by CMT-joining method with ER4043 (AlSi5) filler wire with a diameter of 1 mm. Test specimens were cut and prepared 250x200 mm. 100% Argon shielding gas was used in the joints. Fully automatic mode was used in ABB IRB1600 robotic system for the applications. A special apparatus suitable for the lap joint position was made and integrated into the robotic system. Al-Steel plates joined at different current (75A, 80A, 85A, 90A, 95A, 100A, 105A, 110A) were prepared using laser cutting and tensile tests were performed on a ZwickRoell Z100 device according to the ISO 6892-1:2001 standard, tensile test specimen example is shown in figure 2. Bending tests were carried out by 3-axis bending method with Instron UTM-HYD 300DX device with 300 kN capacity according to TSE EN ISO 5173:2010/A1 standard. The hardness values of the specimens were taken by using the Vickers method according to EN ISO 6507 standard with a 100 g load vr pyramid pricking tip. For each method, 3 specimens were tested. For macro and micro imaging, the samples were sanded, polished and etched using 3% Nital (3 mL HNO3 and 97 mL H2O) reagents for 8 seconds. A 500x optical microscope and a JOEL JSM-6060LV scanning electron microscope (SEM) were used for imaging. Table 3 shows the applied welding parameters. Figure 2 shows the welding machine and test fixture.

2.3. Combining method with CMT

Joints were made using the cold metal transfer (CMT) MIG/MAG process with the new generation TPSi400 welding machine developed by Fronius international gmbh. Figure 3. shows the application logic of the cold metal transfer method and the formation of the arc according to Ampere/Voltage.

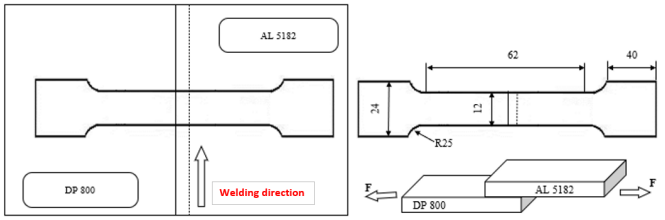

Figure 1. Tensile test specimen example

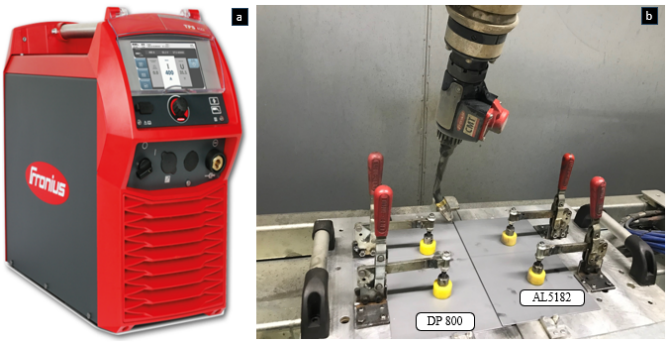

Figure 2. CMT welding machine (a), fixture, specimen and position (b)

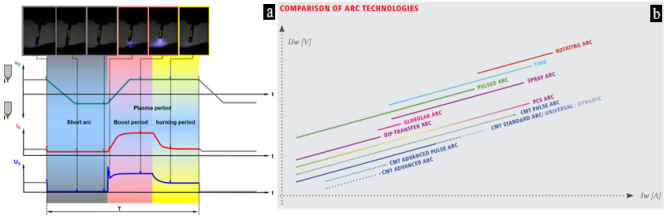

Figure 3. CMT application logic (a), Ampere/Voltage effect table of welding arcs (b) [12]

3. Results and discussion

3.1. Heat inputs and tensile test results

As a result of joining 1 mm DP800 galvanized steel plates and AL5182 plates in the overlap position using ER4043 (AlSi5) filler wire, the maximum strength values measured for each connection are shown in Figure 4(b). The maximum strength value of 4.28 kN was measured in the specimen joined with 90 amperes. The failure zones of the specimens welded at different amperages after tensile test are shown in Figure 4 (a).

Table 3. CMT- Joining parameters.

Material (Sample)	Welding Current(A)	Voltage (V)	Processing speed(cm/min)	Wire feed rate (m/min)	Protective gas flow rate(L/min)	Torch angle (^{0})
N-1	75	11,3	70	6,1	15	75
N-2	80	11,6	70	6,3	15	75
N-3	85	11,9	70	6,4	15	75
N-4	90	12,1	70	7	15	75
N-5	95	12,4	70	7,5	15	75
N-6	100	12,6	70	7,7	15	75
N-7	105	12,8	70	8	15	75
N-8	110	13,1	70	8,2	15	75

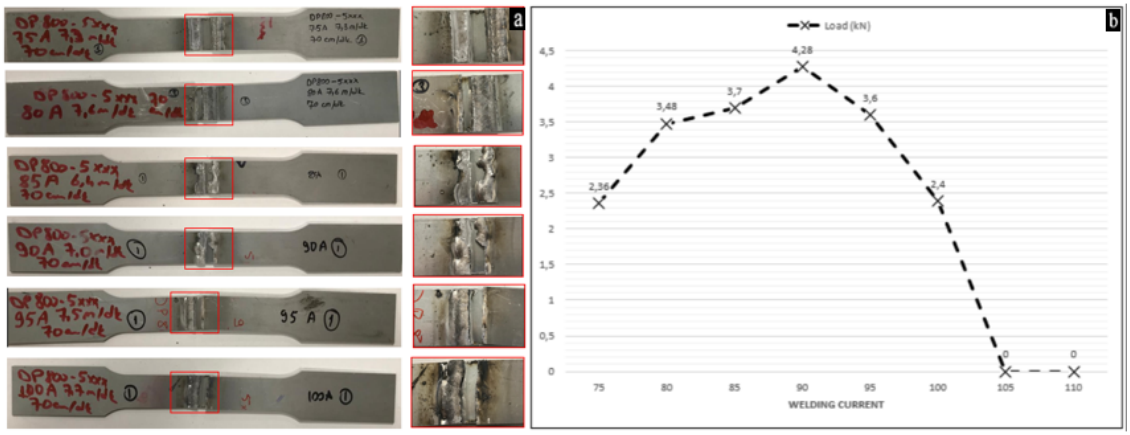

Figure 4. Tensile specimens and failure zones (a), graph of failure strength values (b)

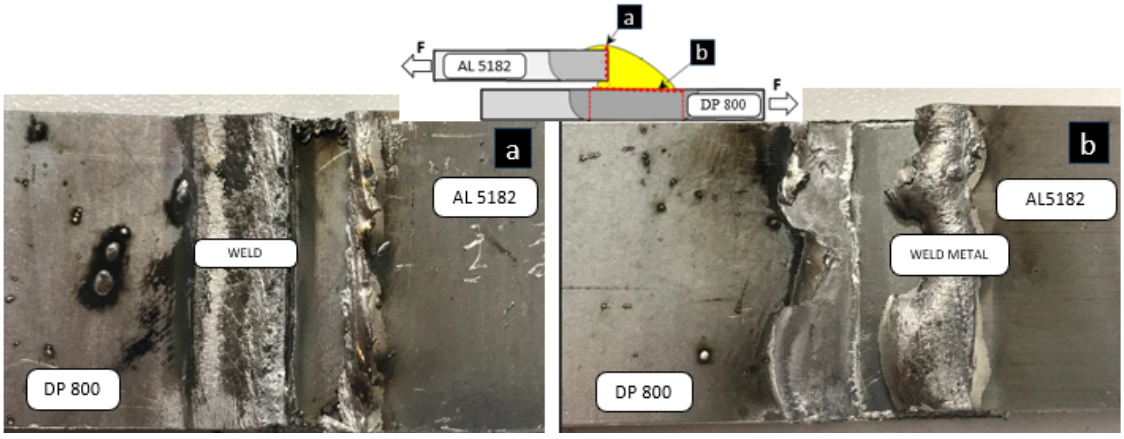

Figure 5. Failure near the heat affected zone (a), failure near the IMC layer (b)

In this research, the fracture location of the tensile test specimens was investigated in two different ways: (a) aluminum fracture is a type of fracture that occurs from the root of the weld seam towards the HAZ (Heat Affected Zone) due to incomplete melting or porosity in the weld root zone, as shown in Figure 5. coarsening grains and dissolution of different precipitates due to thermal cycling make this region weaker. (b) brazed interfaces inter metallic compound (IMC) fracture is the fracture stress occurring at the interface of steel and aluminum. These results can be explained by the thickness of the IMC layer. In another saying, the fracture varies with the variation of amperage and heat input.

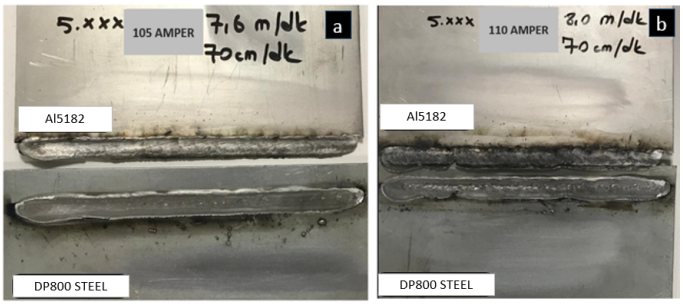

Figure 6. N-7(a) and N-8(b) failed joint test specimens

In Figure 6, the connections with N-7 (105 A) and N-8 (110 A) could not be obtained and therefore test values could not be obtained. It is observed that the thickness of the intermetallic structure increases with increasing heat input, which is known to negatively affect the bonding. In line with this information, it is thought that increasing heat input increases the thickness of the intermetallic structure above the threshold value and fusion cannot be achieved.

The variation of the welding current shown in Figure 7 is a factor in determining its effect on the tensile strength. Differences in tensile strength test results of connections made with different amperage values may be reflected by different levels of thickness of the IMC layer. It can be said that the increase in IMC layer thickness varies with the change of welding current. It is seen that this increase negatively affects the fracturing strength.

The heat inputs for the joints were calculated with the following formula (1), it was observed that the heat input increased in the joints at constant speed with the welding current and voltage increases.

Heat input formula;

$$Q\left(\frac{j}{mm}\right) = \frac{I(A)xU(V)x60}{V\left(\frac{mm}{dk}\right)} \quad (1)$$

Q = Heat input (J/mm), U = Voltage (V), v = Processing speed(cm/min), I = Welding Current (A),

Based on the results outlined in Figure 8 and Figure 7, heat input, amperage, IMC layer was found to be significant factors in determining the strength and fracture of joints. As the heat input increases, the tensile strength decreases as the grain sizes in the region where the HAZ is located change in the direction of increase. In short, an optimal amperage value was formed to achieve the highest tensile strength, the high heat input caused the tensile strength to decrease, resulting in a thicker, brittle IMC layer.

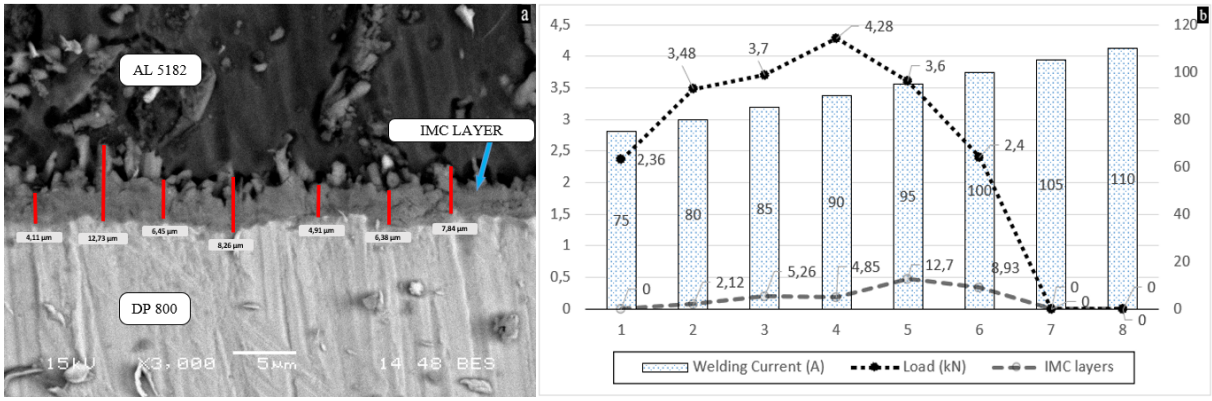

Figure 7. Variable values of IMC thicknesses of N-4 (a), amperage, IMC, load (kN) graph of joints (b)

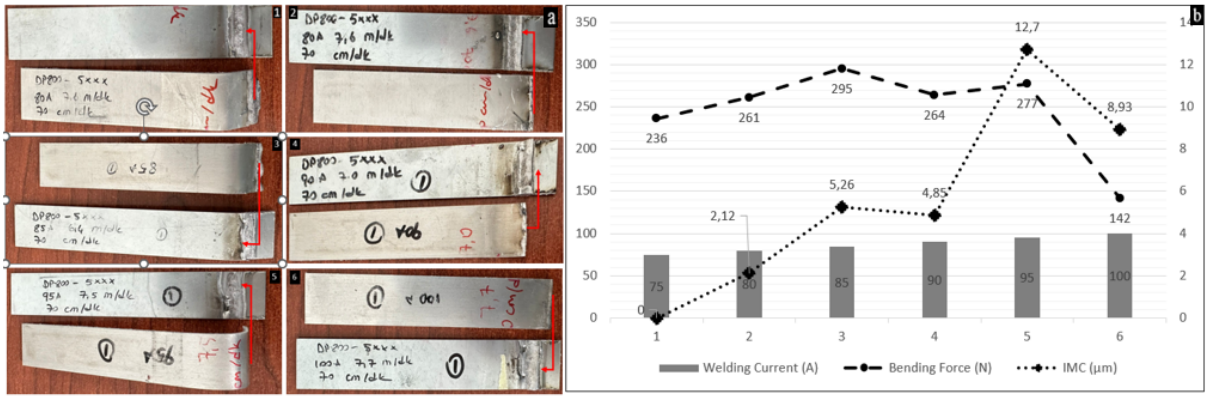

Figure 9. Images of flexure test results (a), welding current, bending force, IMC layer comparison graph (b)

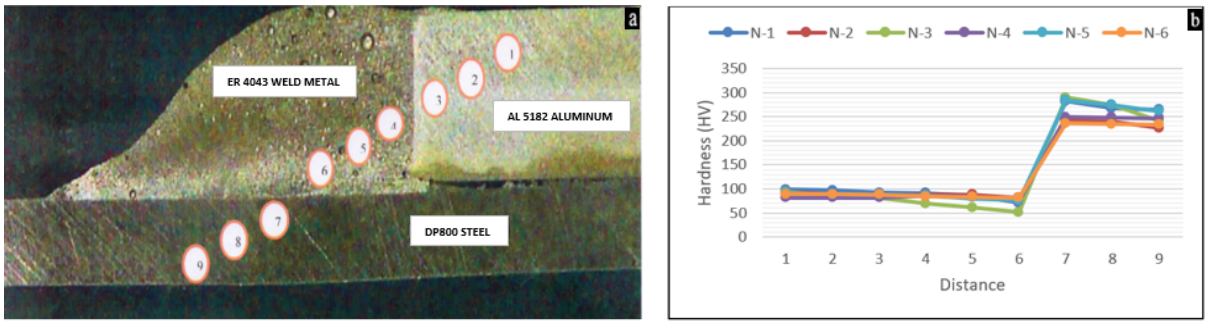

Figure 10. Hardness (Hv) points of lap joint (a), comparison graph of hardness (Hv) values (b)

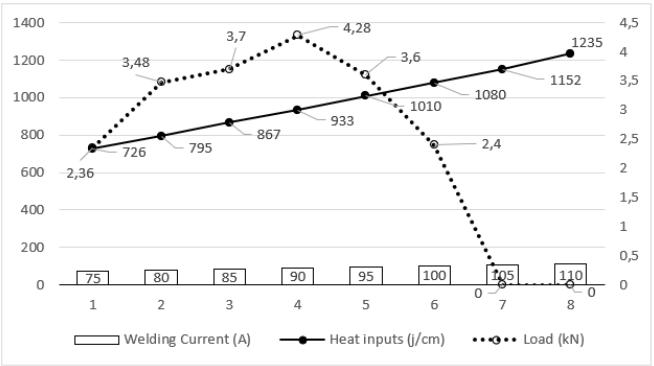

Figure 8. Welding current (A), load (kN), heat input graph of the joints

3.2. Bending test results

The results of the flexure test of the joined specimens are given in Table 4 and Figure 9.

Figure 9. shows that the highest fracture force (295 N) was reached at 85 (A) at N-3 and the lowest fracture force (142 N) was reached at 100 (A) at N-6. IMC thicknesses varied in these tests, supporting that this variation affects the mechanical properties. In addition, the amount of porosity formed in the weld seam is high and these porosities are a factor in the formation of important crack initiation zones.

Table 4. Bending test data of assembled samples

Definition (Sample)	Welding current (A)	Heat input (j/mm)	F_m(kN)	IMC (µm)	Bending Force (N)
N-1	75	726	2,36	1,11	236
N-2	80	795	3,48	2,12	261
N-3	85	867	3,7	5,26	295
N-4	90	933	4,28	4,85	264
N-5	95	1010	3,6	12,7	277
N-6	100	1080	2,4	8,93	142

3.3. Hardness test results

Hardness values taken from the samples are given in Table 5. A total of 9 measurements were taken on the weld metal and the hardness distribution curve in the transition zones was created.

Table 5. Hardness (Hv) values at reference points

Definition	1	2	3	4	5	6	7	8	9
N-1	98,6	97,3	92	91,4	85,9	71,3	282	268	264
N-2	94,7	89,1	85,4	89,3	88,3	81,4	243	240	226
N-3	94,1	84,2	81,5	68,9	62,1	51,1	290	274	242
N-4	81,4	81,1	80,8	86,4	84,8	74,1	250	248	247
N-5	91,2	88,8	88,5	85,9	80,2	76,6	284	274	261
N-6	89	88,9	88,4	84,6	82,6	80,9	236	235	233

The hardness points of the lap joint specimens and the comparison of the specimens with each other at these points are shown in Figure 10. With the formation of intermetallic layers of different thicknesses, it was found that the layer, which was soft in the region close to aluminum, was harder in the regions closer to steel.

It is known that as the pores formed in the chemical composition and the weld metal of the IMC structure differ, the hardness values will also change.

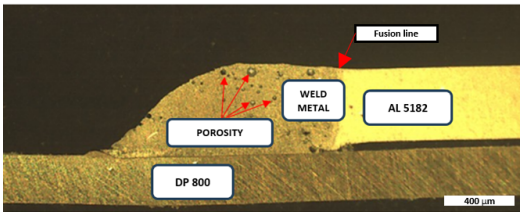

Figure 11. Joining zone failures

Figure 11 shows that porosities are formed in the weld joint as you move towards aluminum. It is estimated that the formation of porosity may be caused by shielding gas or zinc vapor that may be trapped in the weld pool. Zhang et al. concluded that zinc from the steel coating dissolves in the filler metal at the steel-aluminum interface after the joint and some of it evaporates and causes porosity in the weld seam [13].

3.4. Investigation of macro structures

During CMT welding of aluminum to steel, it is known that the zinc vapor remaining in the weld zone and the silicon content in the filler metal affect the wetting capacity of the filler metal [15]. The molten zinc and molten aluminum not only affected and reduced the surface tension of the molten aluminum, but also released the mixing energy in the fusion zone, causing the filler wire to spread [14]. As shown in Figure 12, the weld seam width was measured as 4.48 mm in specimen 4 and the highest breaking strength was determined as 4.28 kN. As the weld width changes, the breaking strength also changes.

3.5. Investigation of micro structures

Examining the microstructures and intermetallic layers shows that the effect of heat input during the MIG welding-fusion process affects the average thickness of the IMC layer formed between the steel and the fusion zone. It has been observed that the thickness of the IMC layer changes with the change in welding current. For example, in Figure 13, the average thickness of the IMC layer for the 95 (A) welded specimen was about 12.7 µm, while for the 75 (A) welded specimen it was about 1.1 µm.

Since the cooling rate during MIG welding-hard brazing varied in different regions, it formed an IMC layer of different thickness. Depending on the chemical composition and amperage of the filler wire, IMC layer thickness is different, and according to the results mentioned above, the thickness of the IMC layer varies not only with the filler wire but also with changing the heat input. This affected the mechanical properties of the welds between the welded specimens. Alloy ratios (%) of the joint areas shows in Table 6.

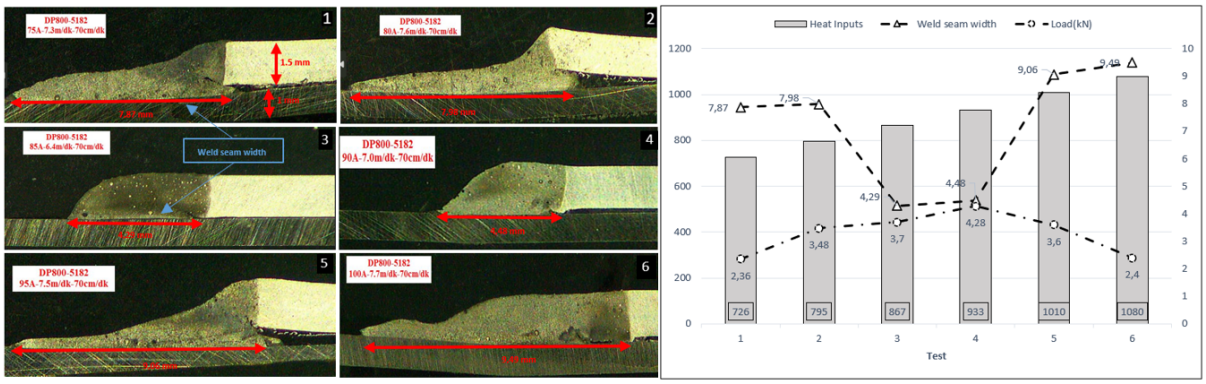

Figure 12. Sample-1-2-3-4-5-6 macro images and head inputs, load, weld seam width comparison

The alloy values determined in Figure 15 are taken from the reference points in Figure 14. Considering the wt.% ratio, it is seen from the phase diagram according to the wt.% ratio of metals that the IMC type is the intermetallic phase for all samples. Differences were observed in the wt% ratios of aluminum and iron obtained in the EDS results, and the brittle phases Fe3Al, FeAl2, FeAl3 and Fe2Al5, brittle phases predicted to form at the interface appear in the IMC layer. It should be noted that at low welding currents (85 A) where the amount of heat input is very low, the variation in thickness of the IMC layer does not follow a certain rule. The reason for this behavior may be due to the low heat input generated at low welding currents. That is, at low heat input, Si could not affect and control the thickness of the IMC layer. Maybe this is because Si cannot increase the solubility of Fe in molten aluminum and therefore cannot control the thickness of the IMC layer, the fluctuations in the IMC thickness are too high and the indentations are too large. Zhang and others. It has been reported that the intermetallic layer formed between the weld metal and the steel extends into the weld metal in sawtooth shape at low heat input, this layer penetrates the weld metal (tongue-like) and is thicker at higher heat input. values [17-19].

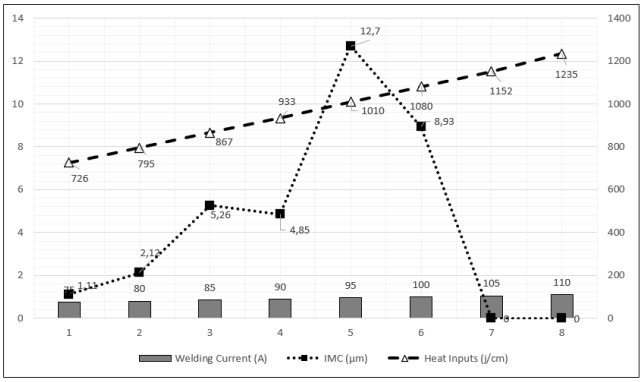

Figure 13. Comparison graph of heat inputs, welding current, IMC of the joints

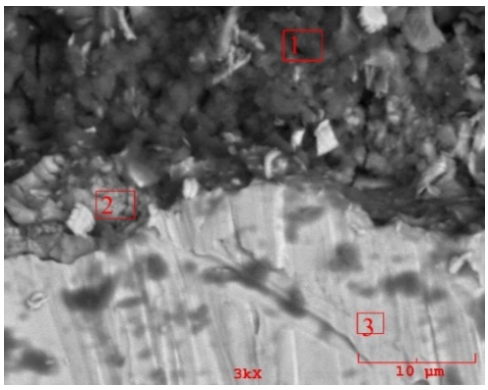

Figure 14. SEM-EDS analysis points of the sample

Table 6. Alloy ratios (%) of the joint areas.

W. Current	Definition	C	Mg	Al	Si	Ti	Mn	Fe	Zn
75	N-1.1	8,649	4,430	36,783	3,720	0,545	2,004	36,059	7,809
	N-1.2	0,617	0,854	23,314	2,493	0,678	1,616	62,220	8,207
	N-1.3	0,193	0,694	1,419	1,586	0,012	1,518	93,337	1,242
80	N-2.1	0.000	0,690	96,935	0,732	0,037	0,334	0,302	0,971
	N-2.2	0,655	1,114	45,571	2,897	0,359	0,310	46,009	3,085
	N-2.3	0,011	0,105	0,908	1,286	0,218	1,893	94,050	1,539
85	N-3.1	0,481	0,558	65,374	29,092	0,105	0,294	2,177	1,918
	N-3.2	0.000	0,300	53,264	3,542	0,019	0,785	41,147	0,943
	N-3.3	0,123	0,097	1,285	2,008	0,180	1,752	93,235	1,443
90	N-4.1	0.000	0,525	92,624	3,034	0,177	0,762	2,616	0,264
	N-4.2	0.000	0,126	61,843	5,670	0,124	0,736	29,647	1,855
	N-4.3	0,118	0,374	0,861	1,380	0,090	2,219	93,938	1,138
95	N-5.1	0,545	1,140	45,010	3,655	0,193	0,592	44,907	3,959
	N-5.2	0.000	0,188	50,370	2,535	0,142	0,889	44,325	1,552
	N-5.3	0,131	0,270	1,850	1,542	0,172	1,427	93,007	1,731
100	N-6.1	0.000	1,190	86,880	2,854	0,481	0,596	3,378	4,622
	N-6.2	0.000	0,230	45,349	5,874	0,244	0,526	43,156	4,621
	N-6.3	0,120	0,126	0,294	0,910	0,155	1,366	96,548	0,600

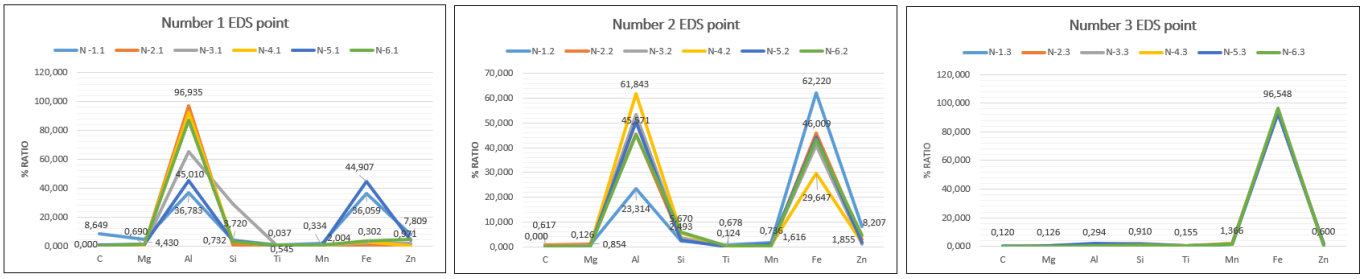

Figure 15. Alloy ratio chart for points 1/2/3 (%)

4. Conclusions

The maximum breaking strength value in the joints was 4.28 kN in the sample joined with 90 A. Fm: 4.28 kN and the breaking strength of the joints at different amperage values varies.

It was determined that intermetallic (IMC) phase formation was observed between the joined aluminum and steel samples and the thickness of this phase changed with the heat input.

After joining, it was determined that the highest fracture force (295 N) value in bending tests was reached at the lowest IMC thickness, and the fracture force was negatively affected as the IMC thickness increased.

The negative effects of evaporating galvanizing were observed in the Al-DP steel joints (incomplete melting, porosity formation). It was also observed that melting aluminum positively affects the wetting angle on galvanizing and directly affects the weld seam of the joints.

Acknowledgments

Ak-Pres Automotive A.Ş. and Sakarya University of Applied Sciences University Prof. Dr. Salim Aslanlar thank you for your support.

Author contributions

Cihan Yakupoğlu: Supervision, resources, roles/writing - original draft, writing - review & editing

Ufuk Öztürk: Data curation, formal analysis, conceptualization

İbrahim Acar: Investigation, methodology, resources

Faruk Varol: project administration, validation

References

1. Schierl, A., The CMT process a revolution in welding technology, Weld. World. **2005**
2. Shi, Y., Zhang, G., Huang, Y., Lu, L., Huang, J., Shao, Y., Pulsed double electrode GMAW brazing for joining of aluminum to steel, Weld. J. **2014**
3. Shao, L., Shi, Y., Huang, J., Wu, S., Effect of joining parameters on microstructure of dissimilar metal joints between aluminum and galvanized steel, Mater. Des. **2015**, 66, 453–458
4. Peyre, P., Sierra, G., Deschaux-Beaume, F., Stuart, D., Fras, G., Generation of aluminium–steel joints with laser-induced reactive wetting, Mater. Sci. Eng. **2007**, 444(1-2): 327–338
5. Park, H.J., Rhee, S., Kang, M.J., Kim, D.C., Joining of steel to aluminum alloy by AC pulse MIG welding, Mater. Trans. **2009**, 50(9):2314–2317
6. Boumerzoug Z., et al. Fabrication and welding of aluminum composite, The International Journal of Materials and Engineering Technology, **2022**, 5(2):71-74
7. Iwase, T., et al., Dissimilar metal joining between aluminum alloy and hot-dip aluminized steel sheet, Kobelco Technol. Rev. **2008**:29–34
8. Türkoğlu, R., Aydın, L., & Gültürk, E., Modelıng and Optımum Parameters of CO_2 Laser Mıg Hybrıd Weldıng Proces. The International Journal of Materials and Engineering Technology, **2021**, 4(2), 91-100
9. Babu, S., Panigrahi, S.K., Ram, G.J., Venkitakrishnan, P.V., Kumar, R.S., Cold metal transfer welding of aluminium alloy AA 2219 to austenitic stainless steel AISI 321. Journal of Materials Processing Technology, **2019**, 266:155-164
10. Madhavan, S., Kamaraj M., Vijayaraghavan, L., Microstructure and mechanical properties of cold metal transfer welded aluminium/dual phase steel, Science and Technology of Welding and Joining, **2016**, 21(3):194-200
11. Singh, J., Arora, K. S., & Shukla, D. K., Lap weld-brazing of aluminium to steel using novel cold metal transfer process, Journal of Materials Processing Technology, **2020**, 283, 116728
12. <https://www.fronius.com/tr-tr/turkey > Dated 11.06.2023
13. Zhang, H., T., Feng, J., C., He, P., Zhang, B.B., Chen, J.M., Wang, L., The Arc Characteristics and Metal Transfer Behaviour of Cold Metal Transfer and Its Use in Joining Aluminium to Zinc-Coated Steel, Materials Science and Engineering. **2009**, 499, 111-113
14. Yagati, K.P., Bathe, R.N., Rajulapati, K.V., Rao, K.B.S., Padmanabham, G., Fluxless arc weld-brazing of aluminium alloy to steel. Journal of Materials Processing Technology, **2014**, 214(12):2949-2959
15. Medgyesi, T., Popescu, M., Opris, C., Difficulties Encountered in Performing Dissimilar Joints On Sheets, Proceedings of The 22nd International DAAAM Symposium, Vienna, Austria, **2011**
16. Gullino, A, Matteis, P, D'Aiuto, F., Review of Aluminum-To-Steel Welding Technologies for Car-Body Applications. Metals; **2019**, 9(3): 315.
17. Dong, H., Hu, W., Duan, Y., Wang, X., Dong, C., Dissimilar metal joining of aluminum alloy to galvanized steel with Al–Si, Al–Cu, Al–Si–Cu and Zn–Al filler wires. J. Mater. Process. Technol. **2012**, 212, 458–464
18. Su, Y., Hua, X., Wu, Y., Influence of alloy elements on microstructure and mechanical property of aluminum–steel lap joint made by gas metal arc welding, J. Mater. Process. Technol, **2014**, 214, 750–755
19. Kobayashi, S., Yakou, T., Control of intermetallic compound layers at interface between steel and aluminum by diffusion-treatment [J]. Materials Science & Engineering A, **2002**, 338(1-2):44-53

The International Journal of Materials and Engineering Technology (TIJMET) (2023) 6(2)
http://dergipark.gov.tr/tijmet
ISSN: 2667-4033

RESEARCH ARTICLE

Electrodeposition of hard chromium on the interior surface of infantry rifle barrels: an experimental investigation

Uğur Temel Yildiz[1,2], Temel Varol[2], Serhatcan Berk Akçay[2], Gençağa Pürçek[3]

[1]Trabzon Silah Sanayi A.Ş., Research and Development Department, Trabzon, Türkiye
[2]Karadeniz Technical University, Metallurgical and Materials Engineering Department, Trabzon, Türkiye
[3]Karadeniz Technical University, Mechanical Engineering Department, Trabzon, Türkiye

Article Info

Article history:
Received 11.12.2023
Revised: 25.12.2023
Accepted: 26.12.2023
Published Online: 31.12.2023

Keywords:
Barrel
Electroplating
Hard chromium
Surface coating
Steel

Abstract

The objective of this study was to enhance the properties of the inner surface of a rifle barrel. The substrate utilized in this investigation was produced through the cold forging technique using 42CrMo4 material, measuring 260 mm in length and 5.56 mm in diameter. Electrolytic hard chromium plating was employed to create a durable metal layer on the inner surface of the substrate. A peristaltic pump was utilized to eliminate gases, such as hydrogen and oxygen, which evolved at the cathode and anode during the process. An anode material comprising a steel rod coated with a 93% Pb-7% Sn alloy, possessing a diameter of 2.35 mm, was employed in the coating experiments. Vickers hardness testing was performed to measure the hardness of both the substrate and the coating layer. The coating thickness ranged approximately between 23 µm to 30 µm. Hardness analysis conducted at various points indicated a proportional decline in coating microhardness with increasing coating thickness. Following the electrolytic hard chrome plating process, the inner surface hardness of the barrel reached approximately 1143 HV0.025.

1. Introduction

Infantry rifles are engineering products with a large global commercial market. These products, which are used by the security and law enforcement forces of various countries, have a certain lifespan as with all engineering products. One of the critical components of infantry rifles that determine their lifespan is the barrel 1. The inner parts of the barrels, in other words the rifling surfaces, are under thermal, chemical and mechanical effects due to their role in infantry rifle systems 2. Due to corrosion and abrasion caused by the aforementioned effects, material loss occurs on the rifling surfaces of the barrels and the accuracy performance and lifetime of the barrels decrease 3. In order to increase the service life of barrels, two methods come to the forefront as the use of materials that are more resistant to the thermal, chemical and mechanical effects that occur during the use of these products in the production of the weapon system or the application of coating applications 4.

Some examples of different materials used to increase the service life of barrels are ceramic matrix/metal matrix composite 5, cobalt-based alloy 6, and Si_3N_4 7. Among these materials, composites are not widely used in the production of barrels due to the problems that may arise from the differences in properties such as elasticity and thermal expansion coefficient between the matrix and reinforcement, cobalt-based alloy cost and Si_3N_4 cost and poor production capability. Due to these limitations, low alloy steel is widely used in barrel production.

On the other hand, some of the surface treatments that can be used to increase the life of barrels made of low alloy steel can be listed as follows: physical vapor deposition, chemical vapor deposition explosive bonding, thermal spray, electrolytic hard chrome plating 8. Among these methods, chemical vapor deposition, thermal spray, explosive bonding, and physical vapor deposition have not gained widespread use due to the undesirable metallurgical changes in low-alloy steel material due to the relatively high temperatures at which they are carried out, and due to the problems encountered in the application of these methods to the inner parts of barrels with an inner diameter of 5.56 mm and 7.62 mm. Therefore, electrolytic hard chrome plating is widely used in the tribological improvement of the rifling surfaces of infantry rifle barrels due to its hardness above 1000 HV, chemical inertness and ease of application 14.

In this study, it was aimed to improve the rifling surface of a 5.56 mm inner diameter infantry rifle barrel produced by cold forging method from 42CrMo4 low alloy steel material by electrolytic hard chrome plating method. In this context, the inner surface of the barrel was electrolytically hard chromium plated by forced circulation method, and the thickness and microhardness distribution of the obtained coating along the length of the barrel was characterized.

2. Materials and Methods

The chemical composition of 42CrMo4 low alloy steel material supplied from ABS- Acciaierie Bertoli Safau S.p.A. (Italy) was verified by optical emission spectrography (Arun Technology, Artus 8, UK). The data obtained as a result of the test are compiled in Table 2. For the determination of the initial microhardness of the test material, a square specimen with a cross section of 10 mm x 10 mm and a height of 10 mm was cut and mounted. Sanding was carried out using 320, 600 and 1200 sandpapers. Polishing was carried out in two stages using 6 µm and 1 µm sized diamond abrasive particle suspension. The sample was etched with 2% nital solution. Vickers microhardness measurement (EMCOTEST DuraScan G5,

Corresponding Author: Temel Varol
E-mail: tvarol@ktu.edu.tr

How to cite this article:

Yildiz, U.T., Varol T., Akçay S.B., Pürçek G., Electrodeposition of hard chromium on the interior surface of infantry rifle barrels: an experimental investigation, The International Journal of Materials and Engineering Technology (TIJMET), 2023, 6(2): 66-69

Austria) was performed with a load of 0.025 kg using Vickers indenter tip. A barrel of 260 mm in length and 5.56 mm in diameter, produced by the cold forging method from the validated material.

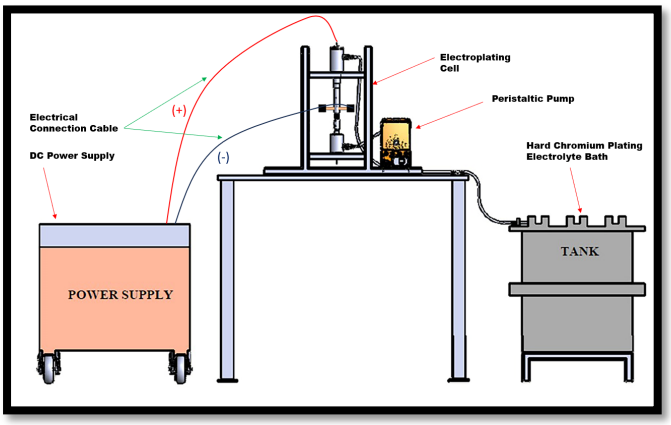

Figure 1. Electrolytic hard chromium plating setup

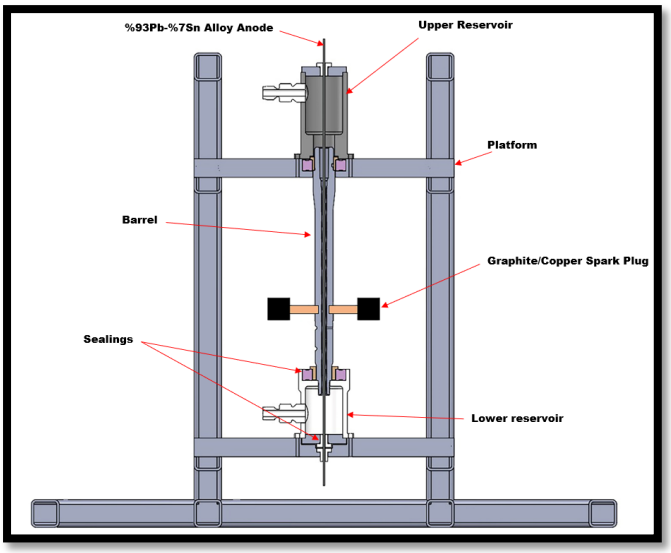

Figure 2. Electroplating cell

The inner surface of the barrel was electrolytically hard chrome plated after hot alkaline degreasing and electrolytic chromic acid etching. The electrolytic chromic acid etching and electrolytic hard chrome plating processes were carried out using chromic acid, sulfuric acid and proprietary additives in the plating setup shown in Figure 1 and Figure 2. The process parameters used in electrolytic chromic acid etching and electrolytic hard chrome plating processes are shown in

Table ***1***.

In the hard chrome plating process, a 93% Pb-7% Sn alloy coated steel wire with a final diameter of 2.35 mm was positioned at the center of the barrel as the anode. In the plating setup, a peristaltic pump (Bimetron, PSA-M-600, Turkey) was used to circulate the electrolyte to remove the oxygen and hydrogen gases formed on the anode and cathode surfaces during plating. Electrical connection to the barrel was carried out with graphite reinforced copper spark plugs. After coating, the barrel was rinsed with pure water and dried. The barrel was immersed in an oil bath to create a protective film layer to protect it until the characterization process.

In order to examine the coating thickness and coating hardness along the length of the barrel, samples were taken from five different areas of the barrel as shown in Figure 3. The samples were mounted for sanding and polishing. Coating thickness measurements of the samples were performed with an Olympus GX-53 metallurgical microscope using Stream Essentials program. Microhardness measurements were performed by applying a 0.025 kg load with a Vickers indenter tip.

Table 1. Process parameters of electroplating.

Parameter	Value
Chromic acid concentration	300 gr/L
Sulfuric acid concentration	3 gr/L
Catalyst concentration	55 mL/L
Temperatıre	55°C
Etching current density	15 A/dm^2
Etching time	5 min
Plating current density	35 A/dm^2
Plating time	30 min
Electrolyte flow rate	700 mL/min

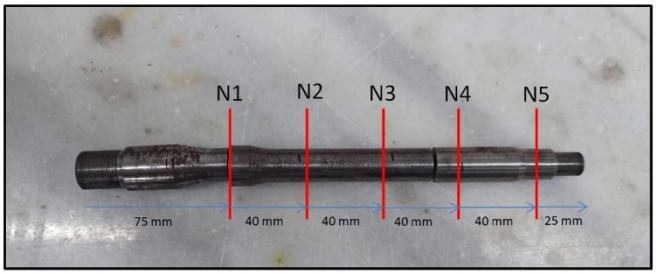

Figure 3. Cross-sectional sampling areas along the barrel length and sample codes

3. Results and Discussion

Initial microhardness of barrel material is shown in Figure 4. As can be seen in Figure 4 barrel materials initial hardness is 299,5±10 $HV_{0,025}$. Micrographs of Vickers microhardness measurements of the hard chromium coating along the length of the barrel rifling surface are shown in Figure 5. The coating thicknesses and coating microhardness variation along the barrel length can be seen in Figure 6 and Figure 7, respectively.

Figure 6 shows that the highest coating microhardness was determined as 1143±18 $HV_{0.025}$ in the sample N5 and the lowest coating microhardness was determined as 986±9 $HV_{0.025}$ in the sample N4. As shown in Figure 7, the lowest coating thickness was 23.38±0,7 µm for sample N5 and the highest coating thickness was 30.10±1,3 µm for sample N4.

Table 2. Chemical composition of supplied low alloy 42CrMo4 steel (in wt%) 15.

Element	C	Si	Mn	P	S	Cr	Mo	Fe
DIN EN 10083-3 – 42CrMo4	0,38-0,45	Max. 0,40	0,60-0,90	Max. 0,025	Max. 0,035	0,90-1,20	0,15-0,30	Balance
Measured Values	0,45	0,14	0,57	0,003	0,005	1,12	0,17	Balance

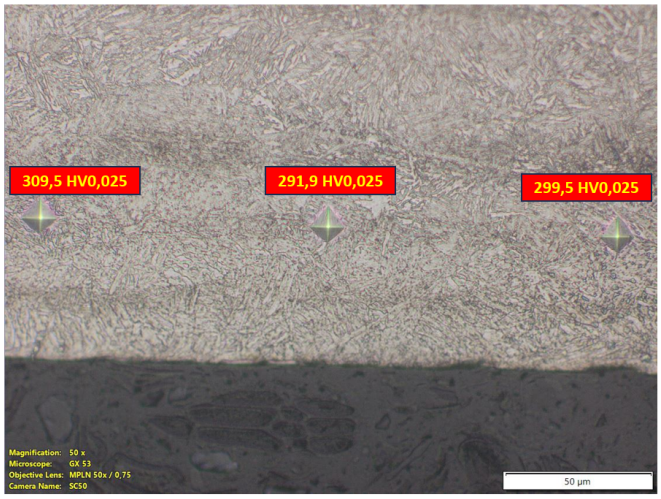

Figure 4. Initial microhardness of low alloy 42CrMo4 steel barrel material

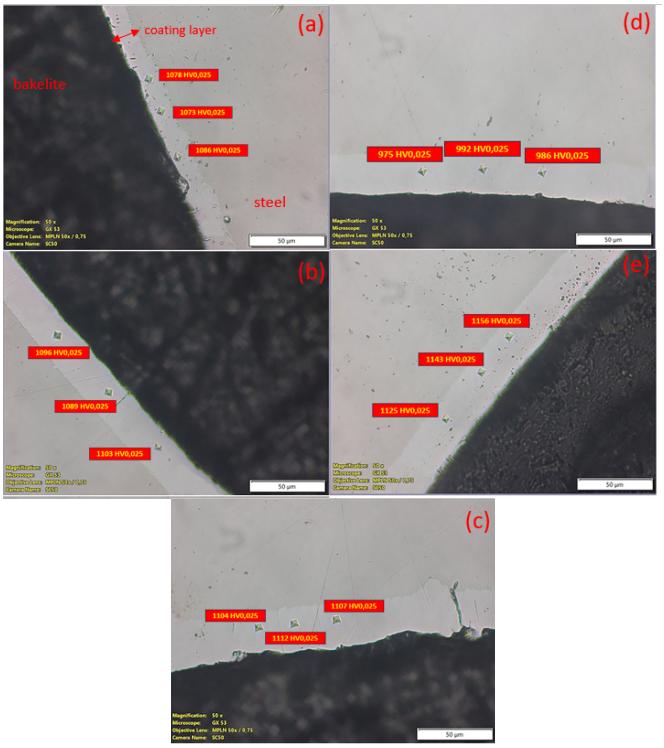

Figure 5. Microhardness measurements along the barrel length; (a) N1, (b) N2, (c) N3, (d) N4, (e) N5 sample

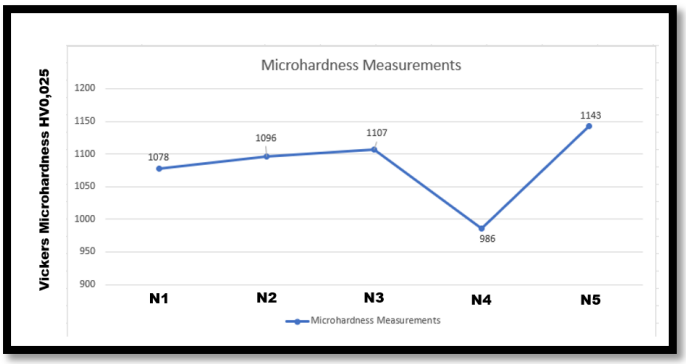

Figure 6. Coating microhardness distribution along the barrel length

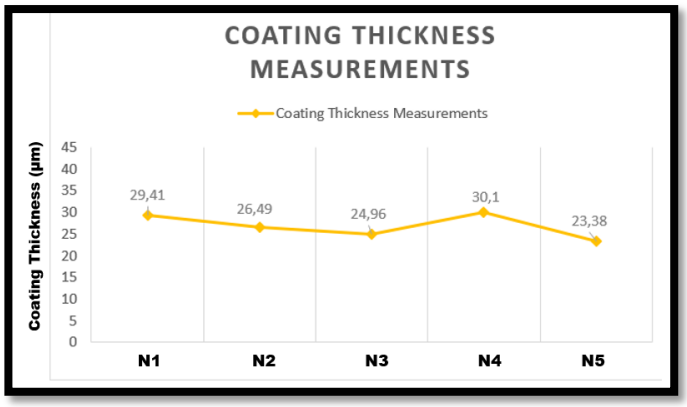

Figure 7. Coating thickness variation along the barrel length

As can be seen in Figure 6 and Figure 7, the coating microhardness value decreases with the increase in coating thickness. As stated by Schlesinger and Paunovic, in electrolytic hard chromium plating, the coating rate increases by keeping the current density constant and decreasing the temperature 16. With the increase in the coating speed, the coating thickness also increases. As the electrolyte enters the inner surface of the barrel from the N5 region, the temperature decreases as it moves towards the N1 region. Therefore, there is an increase in the coating thickness from the N5 region to the N1 region.

As a result of their study, Wahl and Gebauer revealed that at constant current density, the coating microhardness reaches a peak value in a certain temperature range and a decrease in hardness occurs below or above this range 17. Therefore, a decrease in the microhardness values observed due to the cooling that occurred in the movement of the electrolyte from the N5 region to the N1 region.

In the microhardness and coating thickness measurements, the N4 region acts contrary to the general behavior. The reason for this can be interpreted as the electrical connection to the barrel was made from this region. Regional overheating that may occur due to electrical contact is among the factors affecting coating microhardness and thickness.

4. Conclusions

The barrel inner surface hardness, which was initially 299.5±10 $HV_{0.025}$, was increased to between 986±9 $HV_{0.025}$ and 1143±18 $HV_{0.025}$ by electrolytic hard chromium plating method by forming a hard chromium layer between 23.38±0,7 µm and 30.10±1,3 µm along the length of the barrel. The coating layer increased the resistance of the inner surface of the barrel against thermal, chemical and mechanical effects. A decrease in the coating microhardness and an increase in the coating thickness were observed due to the cooling of the electrolyte in the direction along the barrel length. The N4 region is contrary to the general trend of the results. This is due to the fact that the cathode electrical connection was carried out from this region.

Acknowledgments

This study has been completed with the support provided by the Scientific and Technological Research Council of Turkey (TÜBİTAK) within the scope of the 2244 Industry-Academy cooperation program numbered 119C073, by the Karadeniz Technical University Scientific Research Coordination Unit within the scope of FSI-2022-10089 research project and Trabzon Arms Industry (TİSAŞ). The authors would like to thank TÜBİTAK, Karadeniz Technical University Scientific

Research Coordination Unit and Trabzon Arms Industry for their support.

References

1. Dimitrov, M., Analysis on the Next Generation Assault Rifles and Ammunition Designed for the US Army, Problems of Mechatronics, Armament, Aviation, Safety Engineering, **2021**
2. Kalev, K., Analytical determination of pressure in the gun barrel taking into account the wear, Presented at Greener and Safer Energetic and Ballistic Systems - GSEBS 2015, Romania, Bucharest, Military Technical Academy 22-23 May, **2015**
3. Lawton, B., Thermo-chemical erosion in gun barrels, Wear, **2001**, 251(1–12):827-838
4. Burton, L., Carter, R., Champagne, V., Emerson, R., Audino M., Troiano, E., "Army Targets Age Old Problems with New Gun Barrel Materials", AMPTIAC, **2004, 8(**4)
5. Katz, R.N., Bracamonte, L.A., Withers, J.C., Chaudhury, S., Hybrid Ceramic Matrix/Metal Matrix Composite Gun Barrels, Materials and Manufacturing Processes, **2006**, 21(6), 579-583
6. de Rosset, W.S., Montgomery, J.S., Cobalt-base alloy gun barrel study, Wear, **2014**, 316(1–2):119-123
7. Storm, R., Withers, J.C., Ramos, R., Loutfy. R.O., Fabrication of Si3N4 Gun Barrel Liners for Very High Temperature Erosion Resistant Gun Barrels, Materials and Manufacturing Processes, **2012**, 27(8): 875-877
8. Sheward, J.A., The coating of internal surfaces by PVD techniques, Surface & Coatings Technology, **1992**, 297-302
9. Levy, R.A., Investigation of Chemically Vapor Deposited Tantalum for Medium Caliber Gun Barrel Protection, New Jersey Institue of Technology, **2008**
10. Miller, M.D., Campo, F., Troiano, E., Smith, S., de Rosset, W.S., Explosive Bonding of Refractory Metal Liners, Materials and Manufacturing Processes, **2012**, 27(8):882-887
11. Trexler, M.D., Carter, R., de Rosset, W.S., Gray, D., Helfritch, D.J., Champagne, V.K., Cold Spray Fabrication of Refractory Materials for Gun Barrel Liner Applications, Materials and Manufacturing Processes, **2012**, 27(8):820-824
12. Jiang, X., Wang, Y., Lu, X., Research on the Mechanism of Extending Artillery Barrel Life by Electrical Explosion Spraying Technology. Advanced Materials Research, **2012**, 429, 19-24
13. Audino, M.J., Use of Electroplated Chromium in Gun Barrels, DoD Metal Finishing Wrokshop, Washington, DC., **2006**
14. Newby, K.R., Industrial (Hard) Chromium Plating, Surface Engineering, ASM Handbook, Edited By Cotell, C.M., Sprague, J.A., Smidt, F.A. Jr., ASM International, **1994**, 5, 177–191
15. DIN EN 10083-3 Steels for quenching and tempering- Part 3: Technical delivery conditions for alloy steels English Version of DIN EN 10083-3:2007-01, DIN Deutsches Institut für Normung e.V., Berlin Germany, **2007**
16. Schlesinger, M., and Paunovic M., Modern Electroplating., Hoboken N.J: Wiley. **2010**, 5
17. Dennis, J.K, Such, T.E., Nickel and Chromium Plating 3rd Edition, Woodhead Publishing Limited, **1993**

The International Journal of Materials and Engineering Technology (TIJMET) (2023) 6(2)
http://dergipark.gov.tr/tijmet
ISSN: 2667-4033

REVIEW ARTICLE

Intercalation reaction in lithium-ion battery: effect on cell characteristics

Theodore Azemtsop Manfo[1] and Mustafa Ergin Şahin[1]

[1]*Recep Tayyip Erdogan University, Faculty of Engineering of Architecture, Department of Electrical and Electronics Engineering, Rize, Türkiye*

Article Info

Article history:
Received 08.12.2023
Revised: 27.12.2023
Accepted: 30.12.2023
Published Online: 31.12.2023

Keywords:
Lithium-ion battery
Electrolyte
Intercalation
Graphite
Voltage
Energy efficiency

Abstract

Lithium-ion batteries (LIBs) are vital components in mobile devices and electric vehicles (EVs) due to their high energy density and long lifespan. However, to meet the rising demand for electrical devices, LIB energy density must be improved further. Anode materials, as a key component of lithium batteries, significantly improve overall energy density. LIBs are a widely utilized electrochemical power source in EVs and energy storage. LIBs have proven to be consistent because of their superior power density, which is directly related to the type of cathode, and extended lifespan in comparison to other types of rechargeable batteries. LIBs are developed with suitable electrolytes through a complex pathway that almost parallels advances in electrode chemistry. This work concentrates on the intercalation of alkali metal ions (Li^+) into graphite, summarizing the important advances from experiments and theoretical calculations that underlie the close host-guest relationships and their underlying mechanics. This study elucidates the effect of the intercalation mechanism on the electrode surface to achieve high-performance LIBs. Lithium metal ions in graphite are intercalated into monovalent and multivalent ions in layered electrode materials. This will result in a better understanding of intercalation chemistry in host materials for storage and conversion applications. This review emphasizes the impact of lithium intercalation chemistry on the battery cell using different types of electrode materials to improve its performance. It also studies the influence of the electrode properties on the LIB technology.

1. Introduction

Energy is a key component of any society's progress. It is also needed in industrial settings. As a result, the key concern is to increase the efficiency with which this energy is produced, stored, and delivered [1]. The rapid growth of Li-ion battery technology has piqued the interest of academics [2]. LIBs are currently the market's principal energy source and are widely used in a range of industries, namely gadgets, car batteries, and renewable energy systems [3]. LIB energy density can usually be increased by using high-voltage active cathode materials, anode materials, and electrodes [4,5].

In 1976, Whittingham conducted a significant study published in science [6-8], demonstrating that TiS_2 is an effective host for Li^+ intercalation for energy storage. Recent publications have provided insights into the fundamental characteristics of Li, TiS, and other intercalation compounds. The limitations of traditional energy storage systems such as batteries are their slow charging and short life span limitations [9]. Due to the aggressive reaction of alkali metals with water, LIBs used flammable organic Li^+ electrolytes [10]. Current LIB designs typically feature a carbon (graphite) anode and a transition metal oxide intercalation host as a cathode [11]. Many countries have simultaneously studied the reversible incorporation of Li^+ into graphitic carbon. This work demonstrated that Li^+ is reversibly incorporated into graphitic carbon to form LiC_6 [12]. The wireless revolution started with the introduction of battery-powered mobile phones, made possible by advancements in technology [13]. LIBs are found in hybrid and electric automobiles, but they have shortcomings and efforts are underway to replace them [14]. Goodenough recently released a perspective article called "Outlook on Lithium-ion Battery" in Science China Chemical [15], which discusses the past, and present challenges, and potential research paths for the widely used energy storage technology.

The LIB has undergone continuous improvements in intercalation materials over its nearly twenty-year lifespan, and $LiCoO_2$ replacements like $LiNi_{1-y-z}Mn_yCo_zO_2$, $LiFePO_2$, and $Li_4Ti_5O_{12}$ have been introduced at different rates, leading to gradual performance enhancements. However, all of these materials have inherent capacity constraints due to their redox operation and structural characteristics. Many years have elapsed since the discovery of high-capacity electrode materials that can be formed by electrochemistry with lithium in metals and semi-metals. These alloying reactions yield exceptionally large capacities in both weight and volume (examples include silicon with 8365 mAh cm^{-3} and 3590 mAh g^{-1}, graphite with 975 mAh cm^{-3} and 372 mAh g^{-1}). " However, the dealloying process introduces enormous volume changes that cause substantial stresses in the active material particles and generally also in a composite electrode, which complicates their practical application. When cycling these modifications occur, de-cohesion increases, particle displacement occurs and capacity is lost [16,17]. New approaches to avoid such problems have been studied [18], but ones that limit the effects of volume changes include the change in the active material composition, conductive additive, and polymeric binder in the formulation of electrodes; this, however, reduces the overall capacities of all components used in any electrode assembly. However, efforts in this direction were quite successful, and batteries with

Corresponding Author: Theodore Azemtsop Manfo
E-mail: azemsouleymane@yahoo.fr

How to cite this article:
Manfo, T. A., and Şahin, M. E., Intercalation reaction in lithium-ion battery: effect on cell characteristics, The International Journal of Materials and Engineering Technology (TIJMET), 2023, 6(2): 70-78

composite negative electrodes made from tin (Sn) became commercially viable [19].

The entry of the twenty-first century started attracted by a modern reactivity concept: the reversible electrochemical response of lithium with moving metal oxides [20], which can be generalized as follows equation (1):

$$M_aX_b + (n.b)Li \leftrightarrow aM + bLi_nX \quad (1)$$

Where, M is a transition metal, X is an anion, and n is the formal oxidation state of X.

Conversion processes for various oxides and sulfurs had previously been documented [21,22], with varying degrees of reversibility discovered. Because of the difficulty in intercalating lithium, numerous transition metal complexes with no vacant sites in the structure were ignored. The nanometric nature of the metal particles has been demonstrated to be preserved even after numerous reduction-oxidation cycles [23].

As the largest and fastest-growing battery chemistry on the market [24], higher voltage and capacity materials, as well as a more efficient cell structure, increase energy density. The use of mechanically, thermally, and electrochemically durable components, in conjunction with a battery management system, assures a long service life. It is a challenging task for the battery community to optimize all variables at the same time without compromising safety [25]. This review tends to provide a deep explanation of the influence of the intercalation and correlation between the electrode materials and electrolytes in rechargeable LIBs.

Despite enormous effort and money in boosting Research and Development [26], the majority of battery advancement has occurred at the production level rather than owing to material breakthroughs. There is a deep experimental understanding of how to increase performance and economics, but there are numerous fundamental mysteries about what happens in batteries.

Rechargeable batteries, as the oldest technology for electrical energy storage (EES), are widely employed in everyday life and industrial applications [27]. LIBs are also increasingly being used in applications such as EVs and hybrid electric cars (HEVs), the military, and the aerospace industry [28, 29, 30]. LIBs are the most widely used electrical energy storage technology for a wide range of commercial applications today [31]. This work aims to emphasize the comparison of the properties of some suitable electrode materials used for rechargeable LIBs based on intercalation reactions and their effect on battery performance.

2. Background

Whittingham [32]created the first Li-intercalation cathode in 1972 using titanium disulfide (TiS_2) to increase its voltage potential. This was within the stable potential range of ether below 3.0 V. However, the ester is unstable above 4.0V. Whittingham built a high-energy battery with a titanium disulfide positive electrode and a lithium metal negative electrode in 1976. Figure 1 shows a LIB created by M. Stanley Whittingham [9].

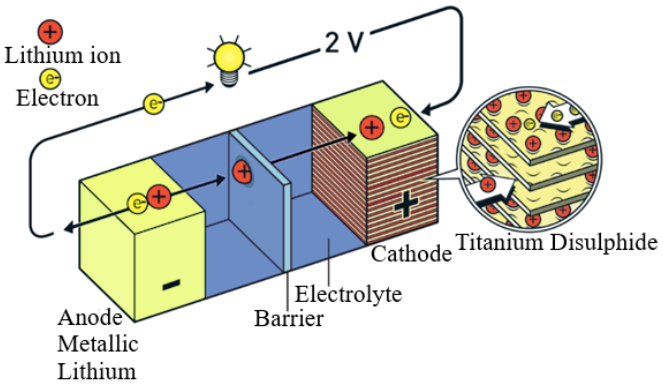

Figure 1. The first lithium-based rechargeable [9]

Whittingham's strategy, on the other hand, was insecure. After Goodenough found metal oxides (such as lithium cobalt oxide., $LiCoO_2$) as high-potential cathode materials, replacing esters with ethers was unavoidable [33]. John Goodenough and Akira Yoshino refined the technology by substituting the cathode and anode with lithium cobalt oxide and graphite, respectively. Stanley Whittingham invented the first functioning lithium battery in the early 1970s, taking advantage of lithium's immense driving energy to release external electrons [9]. Yoshino of Asahi Kasei Corporation invented the first $Li_{1-x}CoO_2$/C cell, which Sony Corporation marketed as a mobile phone and a camcorder [26]. Since then, the amount of energy stored in a handheld LIB has been effectively increased to more than 3.0 Ah in the 18 650 cells that are already accessible [34].

In the early 1950s [35], ethylene carbonate (EC) and propylene carbonate (PC) were the two most prominent members of the well-known nonaqueous solvent, caustic carboxylic ester, or carbonate-containing ester family. Akira Yoshino was able to broaden the concept of intercalation by studying diverse carbonaceous materials. Secondary batteries constructed from this unique mix provide consistent charging and discharging over a large number of cycles over a lengthy period [36].

$LiCoO_2$ has been improved by adding components that stabilize the crystal shape and enhance capacity. A comparative analysis of Figure 2 shows the significant contribution of Goodenough and others who made to the chemical tinkering of various cathode components. These include $LiCo_{1-x}NixO_2$, $LiMnO_2$, and olivine-based $LiFePO_4$.

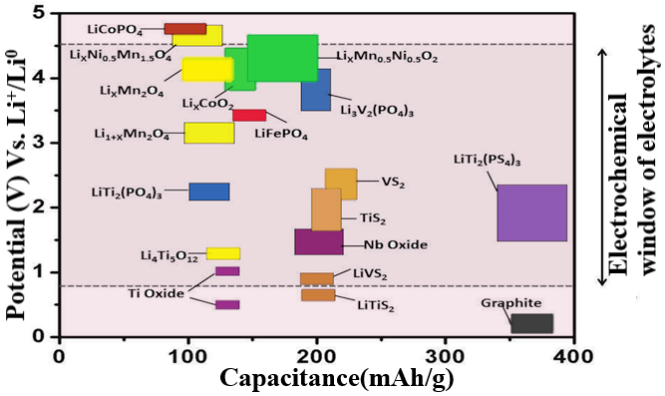

Figure 2. Voltage vs. capacity of various cathode materials about the organic electrolyte window (e.g. 1M $LiPF_6$ in organic carbonate).

The non-aqueous electrolyte propylene carbonate allows for high voltage operation (3.6V), graphite solves the safety concerns linked with lithium steel anodes, and $LiCoO_2$ makes the material robust and strong enough for manufacturing and long-term cycling became. The secondary LIB typically operates at 3.7 V and has a capacity of 150 mAh g^{-1}. Intercalation and de-intercalation of lithium electrochemically in graphite were successfully shown in the first experiment ever carried out by Rachid Yazami in 1982 [37,38]. Figure 3 shows the intercalation process of Li^+. Lithium ions will enter the graphite layer and mix with carbon atoms during the charging process. This necessitates that the anode material generates an exceptionally high voltage.

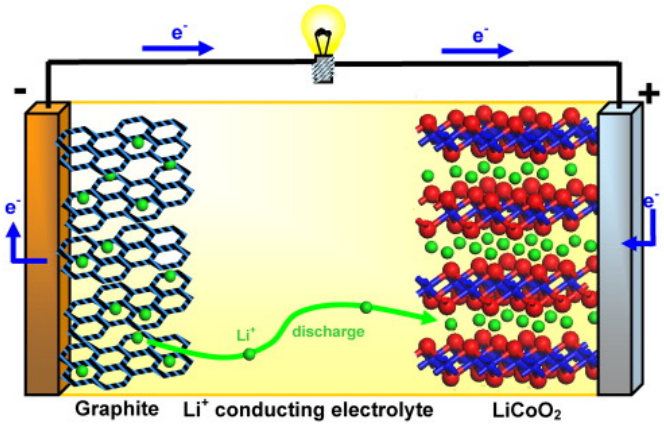

Figure 3. A lithium-ion battery diagram, with the non-aqueous liquid electrolyte $LiPF_6$ ethylene carbonate/dimethyl carbonate as the electrolyte that separates the negative electrode and graphite, from the positive electrode, $LiCoO_2$ [39]

As a result, several electrode materials have been investigated to prevent the negative effect of volume expansion while supporting a sufficient number of active sites. Hollow nanofibers are ideal anode materials for LIBs. The hollow structure not only has a large specific surface area, but it acts as a buffer during the lithiation process. The hollow structure can combine numerous components to improve the LIB's performance.

3. Fundamentals of Metal-Ion Batteries

The energy stored in the battery is released when the cathode and anode are connected through an external circuit. The electrolyte, which is a substance that does not conduct electricity but allows the movement of ions, carries the reactant between the two electrodes to prevent the battery from short-circuiting. These three building components can be joined in several ways.

During manufacturing, a polymer membrane separator is used to insulate the electrodes from each other [40]. The reduction of electroactive species in the cathode material and the Li^+-ion intercalation into accessible locations in the host lattice is involved in the discharge mechanism.

During the discharge process, spontaneous redox reactions cause intercalation at the electrode surface. Electrons are transported from the negatively charged anode to the positively charged cathode via an external circuit to maintain electrical neutrality. When a battery is charged, the cathode releases electrons to the external circuit by desorption of lithium. Common cathode materials include lithium cobalt oxide ($LiCoO_2$, LCO), lithium iron phosphate ($LiFePO_4$, LFP), and lithium manganese oxide ($LiMnO_4$, LMO). In a typical LIB, the positive and negative electrodes undergo the following chemical reaction as shown in the equations (2) and (3):

$$\text{Cathode: } MS_2 + Li^+ + e^+ \rightarrow LiMS_2 \text{ (discharge)} \quad (2)$$

$$\text{Anode: } Li \rightarrow Li^+ + e^+ \text{ (discharge)} \quad (3)$$

Equation (4) depicts the chemical reaction that takes place in a fuel cell during discharge:

$$MS_2 + Li^+ + e^+ \rightarrow LiMS_2 \text{ (discharge)} \quad (4)$$

Where M=Ti, or Mo

Electrons move from the negatively charged anode to the positively charged cathode via the external circuit to maintain electrical balance. During the recharging process, the flow of ions and electrons is reversed by an external load, returning them to the negative electrode. It is worth noting that in this reversed reaction mode, the electrode that was previously positively charged becomes the anode, while the electrode that was negatively charged becomes the cathode. However, battery researchers commonly refer to the functioning electrode as the cathode, regardless of the operational mode. The charging and discharging processes of an intercalation-based rechargeable battery through the electrodes are summarized in Table 1.

Table 1. The charging and discharging processes of an intercalation-based complete battery involve the flow of ions and electrons through the electrodes.

	Charging	Discharging	Process
Cathode	Intercalation Reduction	De-intercalation Oxidation	Ionic process Electronic process
Anode	De-intercalation Oxidation	Intercalation Reduction	Ionic process Electronic process

Without a significant breakthrough, it is unlikely for Li-ion technology to surpass 300 Wh/kg [41]. As progress in Li-ion material development slows down, alternative chemistries involving alkali intercalation have become more interesting [42-44]. Aquion Energy's sodium-ion batteries [45] are the most advanced among Na-, Mg-, K-, and Ca- batteries. The key advantages of Na-ion batteries over Li-ion batteries are that they have similar (but not identical) electrochemistry and are less expensive. Although the energy density is typically on par with or lower than Li-ion, the increased Na^+ concentration tends to harm the host lattice more during prolonged cycling [46].

4. Lithium-Intercalation on Battery Characteristics

A successful intercalation battery must meet several requirements simultaneously, regardless of the ion drive. Commercialization, manufacturing, and disposal are all made possible by low-cost, ecologically acceptable raw materials. A high-capacity, high-voltage cathode with outstanding long-term cyclability does not yet exist. While $LiFePO_4$ exhibits favorable characteristics such as good rate capability, chemical stability, and thermal stability, it has a lower electrochemical potential of 3.5 V and a specific capacity of 170 mAh/g [47,48].

4.1 Capacity

Understanding high-voltage or high-performance materials requires studying both their crystalline and electrical structures. The upper limit of the specific capacity of an intercalating electrode is dictated by the number of electrons that are either gained or lost throughout the cycling process, including the molecular weight of the intercalating substance. Increasing the electrode thickness by minimizing the contribution of all inactive components is a significant technical difficulty [49] that increases the energy density, but leads to reduced power output [50].

4.2 Crystal structure

The fundamental structure of intercalation cathodes consists of a crystal structure containing transition metal centers capable of undergoing redox reactions. This is also generally true for anode materials, except for graphite and other carbon compounds. The majority of effective intercalation materials have a layered structure. Lithiated transition metal oxides such as $LiMO_2$ (where M might be a mix of Co, Ni, or Mn) [51-53] and graphite-based materials [54] are examples of cathode materials. Other materials including alternate oxides such as MoO_3 [55] or V_2O_5 [56], dichalcogenides such as TiS_2 [57], and developing 2D materials such as MXenes, have also gained significant attention. Spinels have a similar structure to layered oxides but with a different arrangement of metal octahedra. $LiFePO_4$(LFP) is a controversial material [58], as its performance sometimes exceeds our current understanding. LFP exhibits a significant miscibility gap at equilibrium and $Li_{0.9}FePO_4$ and $Li_{0.1}FePO_4$ are produced (the precise composition depends on the particle size) [59]. Positively charged cations stabilize the layered oxide structure by opposing the attraction of oxygens in adjacent layers and causing larger interlayer separation. Optimizing many orthogonal aspects of interleaving is a fascinating and challenging part of battery science.

4.3 Voltage

Understanding the chemical potential and interactions between active ions and electrons [60] is crucial for understanding the voltage, making it unnecessary to separate the electronic and ionic components. Conversely, the differentiation of these effects enhances the comprehension of quality. Voltage is mostly affected by the difference in Fermi level between the anode and cathode. Both the chemical potential of interstitial ions in different or crystalline sites and defects that disrupt the local electronic structure affect it. This means that the energy level of the redox pair of this transition metal (or anion, by inference) has a large influence on electrode voltage. By using the ionic radius and Slater's rule, one can determine the amount of oxidizing capacity in a given state of matter for reactive oxygen species. The effective kernel [61] increases electronic binding energy (higher voltage) by adding protons to 3D transition metals.

The first real-world example of an intercalation battery was Whittingham's $LiTiS_2$, which was a rechargeable one [62]. The S-3P band has a relatively low voltage (2.6V vs. Li / Li^+) [63], this is one of the main limitations of chalcogenides in general. Because anionic redox has only been documented for oxides, voltage constraints are usually not overcome by increasing capacity. They instead focused on oxides with lower energy bands (the O-2p band), which led to the development of $LiCoO_2$ (4V) and other cathodes [63,64].

To sum up, capacity and voltage determine the amount of stored energy in a battery. These two characteristics are inextricably linked to the crystal structure and electrical structure of your host material.

4.4 Electronic Conductivity

One of two mechanisms governs electron conduction in electrode materials. At certain Li concentrations, materials such as Li_xCoO_2 and Li_xTiS_2 are metallic conductors [65,66], which contributes to their appealing rate performance. $LiFePO_4$ (LFP) is characterized by its lack of significant conduction and valence bands, which would enable conduction to be delocalized. The main method of electron transport is the polaron hopping process, which involves the localization of electrons and their subsequent lattice disruption.

Carbon coating is a popular approach for enhancing electronic conductivity that is both scalable and cost-effective [67]. Defect chemistry has also been utilized to anticipate changes in electron and ion conductivity [68,69].

4.5 Ionic Conductivity

The crystal structures of the three types of Li-insertion compounds are shown in Figure 4. Their classification is based on the ion diffusion paths and activation energies that control Li-ion transport in electrode materials [70]. In layered oxides ($LiCoO_2$), Li^+ migrates through an intermediate tetrahedral location with a minor diffusion barrier (0.3 eV) (see Fig. 4a), and in spinel ($LiMn_2O_4$), Li moves between tetrahedral sites (x < 1) via the Octahedral site (0.4 eV) (See Fig. 4b) [71]. The operating voltage of LFP is lower than that of other positive electrodes (3.45 V vs. Li+/Li) [72]. Although significant power capabilities of olivine $LiFePO_4$ were not predicted, Li-ion transport occurs with a low barrier of 0.2 eV along a curved oct-tet-oct trajectory along its b-axis (Fig. 4c) [73].

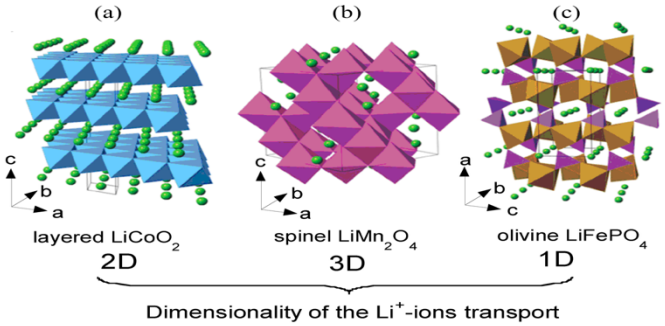

Figure 4. The diffusion pathways for lithium ions include (a) $LiCoO_2$, (b) $LiMn_2O_4$, and (c) $LiFePO_4$ [74]

The first-rate performance of $LiFePO_4$ and the large reported diffusivity raised some questions. $LiFePO_4$ is an interesting case study in ionic transport [75]. The detection of particle size dependency [76] was one discovery that aided in addressing some of the differences. By lowering particle size, nanoscale [77] (50 nm) $LiFePO_4$ outperformed bulk. These initiatives are noticeable in two places: enhanced Li-intercalation in xerogel V_2O_5 [78] and improved Mg-insertion in MoS_2 [79]. Another well-known method for increasing power density is to use nanostructures with short diffusion lengths and large surface areas [80,81]. In one recent example, we used electrospun liquid oxygen (LTO) and liquid propylene oxide (LVP) as anode and cathode in a high power density (HPD) battery [82]. Because

the LTO anode has a high voltage of 1.5 V and the cathode has a low capacity of 110 mAh/g, the energy density is low.

4.6 Mechanical tenacity

The dominance of intercalation electrodes in the current market can be attributed to their mechanical stability. Intercalation materials, which undergo volume changes of less than 10% during the cycle, offer advantages over the conversion and alloying reactions in terms of avoiding difficulties [82]. The strain caused by ion insertion and extraction can be accommodated by porous electrodes and other nanostructures [74]. However, selecting an endpoint in cycling reduces strain but also reduces usable capacity and energy density [83].

4.7 Electrochemistry Stability

The electrodes, electrolyte, current collectors, and container of a successful battery must all be compatible. In an ideal scenario, the occurrence of corrosion or chemical degradation would be nonexistent. However, to safeguard a component from further side reactions, it is necessary for chemical, self-limiting passivation layers to form. An exemplary instance of this passivation tendency can be observed in graphite anodes. Batteries with a cathode frequently operate outside of the thermodynamic stability window to generate the greatest voltage feasible [84]. Despite its kinematic limits, oxidation will eventually deplete energy and power density by irreversibly consuming lithium and building a thicker and more resistant interphase layer. Batteries commonly operate outside the thermodynamic stability window to achieve the maximum feasible voltage on the cathode side.

5. The latest improvement in LIB performance

The revolutionary discoveries resulted in the replacement of the previous era of batteries with a new technology that utilized a CoO_2-cathode and a gasoline coke anode. Notably, John Goodenough, the 2019 Chemistry Laureate, made a critical contribution to quadrupling the capacity of LIBs to 4 volts. This achievement established the groundwork for future growth of considerably more efficient and practical battery systems. Akira Yoshino succeeded in getting rid of natural lithium from the battery and replacing it with lithium ions, which might be more secure than natural lithium. This allowed the battery to be used in practice. Their discovery no longer best enables commercial-scale manufacturing of LIBs but additionally increases studies into a huge variety of the latest technologies, which include wind and solar power. Figure 5 illustrates the layout of the current LIB era advanced via way means of the three scientists.

Table 2. Intercalation electrode materials for rechargeable LIBs.

Type	Cycle life	Working temperature (°C)	Specific Energy (Wh/Kg)	Efficiency (%)	Depth of discharge(%)	Self-discharge rate(% per Month)	Reference
Lead acid	500–5000	−40 –60	35–55	50–75	<70	4–50	[93]
Lithium-ion	1000–20000	−30–55	90–260	~ 95	100	<2	[94]
Na-S	4000–5000	300–350	130–150	75–90	>90	N/A	[95]
Redox flow battery	20,000	10–40	25–40	65–82	100	3-9	[96,97]

Table 3. Various battery systems are compared

	Material	Structure	Average Voltage (V vs. Li)	Practical Capacity (mAh/g)	Date First Reported	Reference
Cathodes	$LiCoO_2$	Layered	~3.9	~140	1980	[86]
	$LiMn_2O_4$	Spinel	~4.1	~120	1983	[87]
	$LiFePO_4$	Olivine	~3.45	~160	1997	[88]
	$LiNi_{1/3}Mn_{1/3}Co_{1/3}O_2$	Layered	~3.8	~200	2001	[89]
	$LiNi_{0.8}Co_{0.15}Al_{0.05}O_2$	Layered	~3.8	~200	2003	[90]
Anodes	Graphite (LiC_6)	Layered	~0.1	~360	1983	[91]
	$Li_4Ti_5O_{12}$	Spinel	~1.5	~175	1994	[92]

Despite incredibly good efforts and funding on the R&D lever [85], maximum battery progress has occurred at the manufacturing level, presently no longer owing to substance breakthroughs. For LIBs, the most effective five realistic cathode and anode substances have been commercialized to date (Table 2).

The hit elimination of natural lithium from $LiCoO_2$ in this generation induced a double within the operating voltage and the electrode's overall performance compared to Whittingham's technology. Petroleum coke as anode cloth well-known shows a wide-place section that is heterogeneous, in the main unbiased, and has some related micro areas. The capability of the negative

electrode and cycle performance is enhanced while the cloth's inner shape is more ordered and less complicated to graphitize. Table 3 compares the cycle life, energy density, efficiency, depth of discharge, and self-discharge rate for different types of batteries. The global market for LIBs has grown rapidly due to the surge in demand for electric vehicles in recent years.

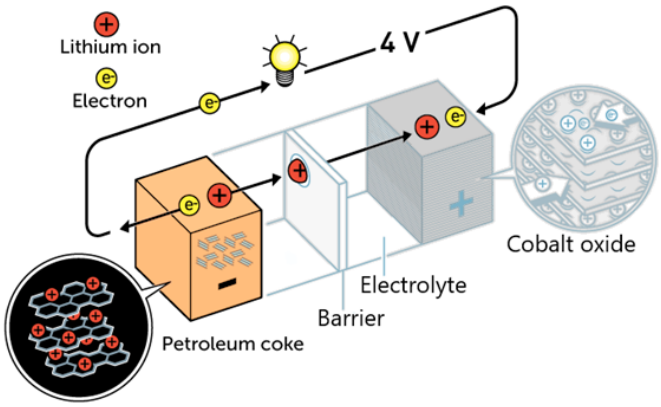

Figure 5. John B. Goodenough's battery with increased cathode potential based on metal oxide [9]

To elaborate on the distinctions between the battery technologies stated above, we have detailed the five significant differences between the four above. The primary differences between flow batteries and LIBs are cost, longevity, power density, safety, and space efficiency. Sodium-ion batteries are a promising replacement for LIBs, which are currently the most used type of rechargeable battery. LIBs offer better efficiency and faster response time than lead-acid and flow batteries. Although LIBs survive longer (they have more charge-discharge cycles than lead-acid batteries), they are typically avoided in low-budget off-grid systems due to their higher cost per kWh of storage capacity [98].

The overall performance parameters of LIBs are largely determined by the electrochemical reactions and the aspect substances utilized in fabricating the batteries, in addition to the mobile engineering and gadget integration involved. The properties of the substances used are determined by the underlying chemistry of the substances. Because of its increased gravimetric power densities of over 250 Wh kg^{-1} and volumetric power densities of less than 650 Wh L^{-1}, Li^{+}-ion production is the most prominent current battery technology, which exceeds any competing generation by employing the element of a minimum 2.5V. However, the adoption of LIBs for powering electric-powered motors faces sizeable challenges.

Modern LIBs are restrained to a specific energy density of less than 250 Wh kg^{-1} and a volumetric energy density of <650 Wh L^{-1}; a boom in those is predicted of up to ~500 Wh kg^{-1} and over a thousand Wh L^{-1}, respectively. In contrast, these lithium-insertion compounds must have specific characteristics such as chemical stability, capacity, rate capability, toxicity, cost, and safety [99]. Such overall performance parameters in large part depend upon the residences of the anode, cathode, and electrolyte substances employed within the battery system, the given surroundings, and the meaningful use. The strength density of a battery is created from its potential, which is particularly governed by the potential of the high-quality electrode. Simple calculations demonstrate that doubling the potential of the high-quality electrode results in a 57% increase in strength density while increasing the potential of the negative electrode by a factor of ten results in a 47% increase in strength density. Although intercalation reactions (structure retention) are used in all rechargeable LIBs nowadays, conversion mechanisms should not be disregarded [100]. Conversion reactions are far more powerful than intercalation reactions. Transition metals are another good choice for the construction of anode electrodes for LIBs due to their high theoretical capabilities, low cost, and ease of supply. The development of new compositions and the improvement of electrical conductivity are the primary goals for these materials. Atomic force microscopy (AFM) is another powerful and multipurpose technology that may be utilized to analyze and characterize LIBs with nanometric resolution [101-103]. Increasing surface quality demands and the development of production technologies necessitate a significant investment in both money and effort [104]. This technique also allows for high-resolution examinations of electrochemical processes, current distribution, surface potential, Li-ion transfer, and other surface properties of LIBs [105-108]. Several commercially available electrode materials are compared in various works based on their performance, power, weight, energy storage capabilities, volume, lifetime, and cost [109]. The selection of suitable materials is a difficult issue for researchers. Materials are assessed for two reasons: creating a new product or improving an existing one.

6. Conclusions

Intercalation has enabled LIBs to power our increasingly mobile civilization. LIBs are a well-known group of devices that vary in price, performance, and safety. However, achieving low cost, extended lifespan, excellent performance, and high safety all at the same time is not always possible. The development of low-voltage anodes and high-specific capacity cathodes with high-voltage is a significant barrier to the development of safe, high-energy-density batteries. The performance of materials, particularly the operating voltage, is influenced by the electronegativity and electrical arrangement of the constituent elements. The host lattice's binding strength ensures mechanical, thermal, and cycle stability. The transition metal binary phases that react with lithium via conversion processes have the potential to improve energy density. Although some electrode engineering-based solutions can avoid this problem, the road to long-term cyclability remains long and convoluted. The remarkable voltage hysteresis observed between discharge and charge considerably lowers the round-trip efficiency of the electrode, which is a very significant and generally underestimated obstacle to application. The selection of proper organic solvents is key because they play an important role in increasing Li-ion mobility, which improves the overall performance of the battery cell and is also critical to the device's safety. As a result, manipulating the microstructures, integrating defects, or changing the matter state of a certain material has a direct influence on lithium intercalation into cathode or anode materials that impacts the performance of the entire rechargeable battery. The results of our study emphasize the importance of enhanced energy quality in the development of high-capacity electrode materials, demonstrating how different transition metal ions and appropriate treatment processes can be used to increase the operating voltage of cathode materials. These findings and tactics apply not only to LIBs but can also serve as design principles to stimulate the development of other electrochemical energy storage systems.

Acknowledgements

The authors are thankful to RTE University for the provided facilities.

References

1. Theodore, A.M., Konwar, S., Singh, P.K., Mehra, R.M., Kumar, Y. Gupta, M. PEO+NaSCN and ionic liquid-based polymer electrolyte for supercapacitor. Mater Today Proc **2020**, 34(3): 802–812
2. Theodore, A.M., Promising Cathode Materials for Rechargeable Lithium-Ion Batteries: A Review. Int. J. Sustain. Energy **2023**, 14(1):51-58
3. Badi, N., Theodore, A.M., Roy, A., Alghamdi, S.A., Alzahrani, A.O. M., and Ignatiev, A. Int J Electrochem Sci **2022**, 17, 22064
4. Badi, N., Theodore, A.M., Alghamdi, S.A., Al-Aoh, H.A., Lakhouit, A., Singh, P.K., Norrrahim, M.N.F., Nath, G. The Impact of Polymer Electrolyte Properties on Lithium-Ion Batteries. Polymers **2022**, 14, 3101
5. Theodore, A.M., Badi, N., Alghamdi, S.A., The Impact of Polymer Electrolyte Properties on Lithium-Ion Batteries. Eliva Press. Global Ltd, **2022**
6. Dines, M. B., Lithium intercalation via butyllithium of the layered transition metal dichalcogenides Mater. Res. Bull. **1975**, 10(4): 287–291
7. Aronson, S., Salzano, F., and Bellafiore, D., Thermodynamic Properties of Potassium-Graphite Lamellar Compounds from Solid-State Emf Measurements. J. Chem. Phys. **1968**, 49(1):434–439
8. Cairns, E.J., and Shimotake, H., High-Temperature Batteries, Science **1969**, 164(3886):1347–1355
9. Theodore, A. M., Progress into lithium-ion battery research. J. Chem. Res. **2023**, 47, 1–9
10. Goodenough, J.B., and Park, K.S., The Li-Ion Rechargeable Battery: A Perspective. J Am Chem Soc **2013**, 135, 1167–1176
11. Van Der Ven, A., Bhattacharya, J., and Anna A. Belak, A.A., Understanding Li diffusion İn Li-Intercalation compounds. Acc. Chem. Res. **2013**, 46(5):1216-1225
12. Yazami, R., Touzain, Ph., A reversible graphite-lithium negative electrode for electrochemical generators. J Power Sources **1983**, 9(3):365–371
13. Whittingham, M.S., Lithium Batteries and Cathode Materials. Chem Rev **2004**, 104(10):4271–4302
14. Choi, J.W., and Aurbach, D., Promise and reality of post-lithium-ion batteries with high energy densities). Nat Rev Mater **2016**, 1(4):16013
15. Goodenough, J.B., and Gao, H., A perspective on the Li-ion battery. Sci. China Chem **2019**, 62, 1555–1556
16. Thackeray, M. M., Vaughey, J. T., Johnson, C. S., Kropf, A.J., Benedek, R., Fransson, L. M. L., and Edstrom, K., Structural considerations of intermetallic electrodes for lithium batteries J. Power Sources **2003**, 113, 124–130
17. Timmons, A., and Dahn, J. R. In Situ Optical Observations of Particle Motion in Alloy Negative Electrodes for Li-Ion Batteries J. Electrochem. Soc. **2006**, 153(6):1206–1210
18. Larcher, D., Beattie, S., Morcrette, M., Edstroem, K., Jumas, J. C., Tarascon, J.M., Recent findings and prospects in the field of pure metals as negative electrodes for Li-ion batteries. J. Mater. Chem. **2007**, 17(36):3759-3759
19. Inoue, H., Mizutani, S., Ishihara, H., Hatake, S., PRiME **2008**, 214th Meeting of the Electrochemical Society, Honolulu, Hawaii (USA)
20. Poizot, P., Laruelle, S., Grugeon, S., Dupont, L., and Tarascon, J. M., Nano-sized transition-metal oxides as negative-electrode materials for lithium-ion batteries. Nature **2000**, 407(6803):496-499
21. Godshall, N. A., Raistrick, I. D., Huggins, and R. A., Mater. Res. Bull. **1980**, 15(5):561–570
22. Henriksen, G. L., and Jansen, A. N., Handbook of Batteries (Eds. D. Linden and T. B. Reddy), McGraw-Hill, New York, **2002**
23. Grugeon, S., Laruelle, S., Dupont, L., and Tarascon, J. M., An update on the reactivity of nanoparticle Co-based compounds towards Li. Solid State Sci. **2003**, 5(6): 895–904
24. Zhao, Y., Pohl, O., Bhatt, AI., Collis, G.E., Mahon, P.J., Rüther T., Hollenkamp AF., A Review of Battery Market Trends, Second-Life Reuse, and Recycling Sustainable Chemistry, **2021**, 2(1):167–205
25. Srinivasan, V., The three laws of batteries (and a Bonus Zeroth Law) Gigaom, **2011**
26. Crabtree, G., The joint center for energy storage research: a new paradigm for battery research and Development AIP Conf Proc **2014**, 1652, 112–28
27. Linden, D., Handbook of Batteries and Fuel Cells; McGraw-Hill Book Co.: New York, NY, USA, **1984**, 1075
28. Yuan, T., Tan, Z., Ma, C., Yang, J., Ma, Z., Zheng, S., Challenges of Spinel Li4Ti5O12for Lithium-Ion Battery Industrial Applications. Adv. Energy Mater. **2017**, 7, 1601625
29. Ren, W.F., Zhou, Y., Li, J.T., Huang, L., Sun, S.G., Si anode for next-generation lithium-ion battery, Curr. Opin. Electrochem, **2019**, 18, 46–54
30. Pistoia, G., Lithium-Ion Batteries: Advances and Applications; Elsevier: Amsterdam, The Netherlands, **2013**, 664
31. Abbas, Q., Mirzaeian, M., Hunt, M.R.C., Hall, P., Raza, R., Current State and Future Prospects for Electrochemical Energy Storage and Conversion Systems. Energies, **2020**, 13, 5847
32. Whittingham. M. S., Chalcogenide battery, US patent 4,009,052, **1973**
33. Goodenough, J. B., and Mizushima, K., Electrochemical cell with new fast ion conductors US patent 4,302,518. **1981**
34. Goodenough, J. B., and Park, K. S., The Li-ion rechargeable battery: a perspective. J. Am. Chem. Soc. **2013**, 135(4):1167–1176
35. Harris, W. S., Electrochemical studies in cyclic esters Thesis, University of California, Berkeley, **1958**
36. Ramanan, A., Nobel Prize in Chemistry, Resonance **2019**, 24, 1381–1395
37. Yazami, R., and Touzain, P. J., Power Sources **1983**, 9,365–371
38. Garche, J., Dyer, C., Moseley, P.T., Ogumi, Z., Rand, D., and Scrosati, B., Encyclopedia of Electrochemical Power Sources Ulm: Elsevier B.V., **2009**
39. Bruce, P. G., Energy storage beyond the horizon: rechargeable lithium batteries Solid State Ionics **2008**, 179, 752–760
40. Arora, P., and Zhang, Z., Battery separators, Chem Rev **2004**, 104(10):4419–4462
41. Thackeray, M.M., Wolverton, C., and Isaacs, E.D., Electrical energy storage for transportation: approaching the limits of, and going beyond, lithium-ion batteries. Energy Environ, **2012**, 5(7):785

42. Muldoon, J., Bucur, C.B., Gregory, T., and Johnson, C.S., Quest for nonaqueous multivalent secondary batteries: magnesium and beyond. Chem Rev **2014**, 114(23):11683–11720
43. Slater, M.D., Kim, D., and Lee E., et al., Sodium-ion batteries Adv Funct Mater **2013**, 23(8):947–958
44. Wang, Y., et al., Emerging non-lithium-ion batteries Energy Storage Mater **2016**, 4, 103–129
45. Whitacre, J.F., Wiley, T., Shanbhag, S., Wenzhuo, Y., Mohamed, A., Chun, S.E., Weber, E., Blackwood, D., Lynch-Bell, E., Gulakowski, J., Smith, C., Humphreys, D., An aqueous electrolyte, sodium-ion functional, large-format energy storage device for stationary applications J Power Sources **2012**, 213, 255–264
46. Masse, R.C., Uchaker, E., and Cao, G. Beyond Li-ion: electrode materials for sodium- and magnesium-ion batteries. Sci China Mater **2015**, 58(9):715–766
47. Yuan, L-X., Wang, Z.-H., Zhang, Hu, X.-L., Chen, J.-T., Huang, Y.-H., and Goodenough, J.B., Development and challenges of LiFePO4 cathode material for lithium-ion batteries. Energy Environ Sci **2011**, 4(2):269–284
48. Wang, J., and Sun, X., Olivine LiFePO4: The remaining challenges for future energy storage Energy Environ Sci **2015**, 8(4): 1110–1138
49. Wood, D.L., Li, J., and Daniel, C., Prospects for reducing the processing cost of lithium-ion batteries. J Power Sources **2015**, 275, 234–242
50. Ogihara, N., Itou, Y., Sasaki, T., Takeuchi, Y., Impedance spectroscopy characterization of porous electrodes under different electrode thicknesses using a symmetric cell for high-performance lithium-ion batteries. J Phys Chem C, **2015**, 119, 4612–4619
51. Massé, R.C., Liu, C., Li, Y., Mai, L., and Cao, G., Energy storage through intercalation reactions: electrodes for rechargeable batteries, Natl. Sci. Rev, **2017**, 4(1):26–53
52. Julien, C.M., Mauger, A., Zaghib, K., and Groult, H., Comparative issues of cathode materials for Li-ion batteries. Inorganics, **2014**, 2(1):132–154
53. Manthiram, A., Knight, J.C., Myung, S.T., Oh, S.M., Sun, Y.K., Nickel-rich and lithium-rich layered oxide cathodes: progress and perspectives. Adv Energy Mater, **2016**, 6, 1501010
54. Kaskhedikar, N.A., and Maier, J., Lithium storage in carbon nanostructures, Adv Mater, **2009**, 21, 2664–2680
55. Hu, X., Zhang, W., Liu, X., Meia, Y., and Huang, Y. Nanostructured Mo-based electrode materials for electrochemical energy storage. Chem Soc Rev, **2015**, 44(8):2376–240
56. Liu, Y., Liu, D., Zhang, Q., and Cao, G., Engineering nanostructured electrodes away from equilibrium for lithium-ion batteries. J Mater Chem, **2011**, 21, 9969
57. Whittingham, M.S., Electrical energy storage and intercalation chemistry. Science, **1976**, 192, 1126–1127
58. Fletcher, S., Bottled Lightning: Superbatteries, Electric Cars, and the New Lithium Economy New York: Hill and Wang, **2011**
59. Meethong, N., Huang, H.Y.S., and Carter W.C. et al., Size-dependent lithium miscibility gap in nanoscale Li1−xFePO4. Electrochem Solid-State Lett, **2007**, 10, A134
60. Maier, J., Review—Battery materials: why defect chemistry? J Electrochem Soc, **2015**, 162(14):2380–2386
61. Slater, J.C., Atomic shielding constants. Phys Rev, **1930**, 36, 57–64
62. Bock, D.C., Marschilok, A.C., Takeuchi, K.J., and Takeuchi, E.S., Batteries used to power implantable biomedical devices Electrochim Acta, **2012**, 84, 155–164
63. Scrosati, B., Power sources for portable electronics and hybrid cars: lithium batteries and fuel cells Chem Rec, **2005**, 5(5):286–297
64. Park, O.K., Cho, Y., Lee, S., Yoo, H.-C., Song, H.-K., and Cho, J., Who will drive electric vehicles, olivine or spinel? Energy Environ, **2011**, 4,1621
65. Menetrier, M., Saadoune, I., and Levasseur, S., Demas, C., The insulator-metal transition upon lithium deintercalation from LiCoO2: electronic properties and a 7Li NMR study. J Mater Chem, **1999**, 9(5):1135–1140
66. Dijkstra, J., Bruggen, C.F.V., Van, and Haas, C., The electronic structure of some monovalent-metal intercalates of TiS2. J Phys Condens Matter, **1989**, 1, 4297–4309
67. Li, H., and Zhou, H., Enhancing the performances of Li-ion batteries by carbon coating: present and future. Chem Commun, **2012**, 48, 1201
68. Shin, J.Y., Samuelis, D., and Maier, J., Defect chemistry of lithium storage in TiO2 as a function of oxygen stoichiometry, Solid State Ion, **2012**, 225, 590–593
69. Shin, J., Joo, J.H., Samuelis, D., and Maier, J., Oxygen-deficient TiO2−δ nanoparticles via hydrogen reduction for high-rate capability lithium batteries, Chem Mater, **2012**, 24, 543–551
70. Goodenough, J.B., Design considerations. Solid State Ion., **1994**, 69, 184–198
71. Zhang, T., Li, D., Tao, Z., and Chen, J., Understanding electrode materials of rechargeable lithium batteries via DFT calculations. Prog Nat Sci Mater Int,, **2013**, 23, 256–272
72. Mayer, S.F., Cristina de la Calle, Fernandez-Diaz, M.T., Amarilla, J. M., and Alonso, J. A., Nitridation effect on lithium iron phosphate cathode for rechargeable batteries. RSC Adv., **2022**, 12, 3696
73. Morgan, D., Van der Ven, A., and Ceder, G., Li conductivity in LixMPO4 (M = Mn, Fe, Co, Ni) olivine materials. Electrochem Solid-State Lett, **2004**, 7, 30
74. Liu, Y., Liu, D., Zhang, Q., and Cao, G., Engineering nanostructured electrodes away from equilibrium for lithium-ion batteries. J Mater Chem, **2011**, 21, 9969
75. Malik, R., Abdellahi, A., and Ceder, G., A Critical Review of the Li Insertion Mechanisms in LiFePO4 Electrodes. J Electrochem Soc, **2013**, 160, 3179–3197
76. Malik, R., Burch, D., Martin Bazant, M., and Ceder G., Particle size dependence of the ionic diffusivity Nano Lett, **2010**, 10, 4123–412
77. Kang, B., and Ceder, G., Battery materials for ultrafast charging and discharging Nature, **2009**, 458, 190–193
78. Wang Y, Shang H, Chou T., et al., Effects of thermal annealing on the Li+ intercalation properties of V2O5 nH2O xerogel films. J Phys Chem B, **2005**, 109, 11361–11366
79. Liang, Y., Yoo, H.D., Li, Y., Shuai, J. Calderon, H.A., Hernandez, F.C.R., Grabow, L.C., and Yao, Y., Interlayer-expanded molybdenum disulfide nanocomposites for electrochemical magnesium storage. Nano Lett, **2015**, 15(3):2194–2202

80. Liu, D., and Cao, G., Engineering nanostructured electrodes and fabrication of film electrodes for efficient lithium-ion intercalation Energy Environ, **2010**, 3, 1218
81. Wang, Y.W.Y., and Cao, G., Nanostructured materials for advanced Li-Ion rechargeable batteries. IEEE Nanotechnol Mag, **2009**, 3, 14–20
82. Liu, C., Wang, S., Zhang, C. Fu, H. Xihui Nan, X., Yang, Y., Cao, G., High-power safety battery with electrospun Li3V2(PO4)3 cathode and Li4Ti5O12 anode with 95% energy efficiency Energy Storage Mater, **2016**, 5, 93–102
83. Mukhopadhyay, A., and Sheldon, B.W., Deformation and stress in electrode materials for Li-ion batteries. Prog Mater, **2014**, 63, 58–116
84. Winter, M., Besenhard, J.O., Spahr, M.E., Novak, P., Insertion electrode materials for rechargeable lithium batteries. Adv Mater, **1998**, 10, 725–63
85. Crabtree G., The joint center for energy storage research: a new paradigm for battery research and development AIP Conf Proc, **2014**, 1652, 112–28
86. Mizushima, K., Jones, P.C., Wiseman, P., and J.B., Goodenough LixCoO2 (0<x<1): a new cathode material for batteries of high energy density, Mater Res Bull, **1980**, 15, 783–789
87. Thackeray, M.M., David, W.I.F., Bruce, P.G., and Goodenough J.B., Lithium insertion into manganese spinels Mater Res Bull, **1983**, 18, 461–72
88. Padhi, A.K., Nanjundaswamy, K.S., and Goodenough, J.B., Phospho-olivines as positive-electrode materials for rechargeable lithium batteries J Electrochem Soc, **1997**, 144, 1188
89. Ohzuku, T., Makimura, Y., Layered lithium insertion material of LiCo1/3Ni1/3Mn1/3O2 for lithium-ion batteries. Chem Lett, **2001**, 30, 642–643
90. Albrecht, S., Kumper, J., Kruft, M., Malcus, S., Vogler, C., Wahl M., and Wohlfahrt-Mehrens, M., Electrochemical and thermal behaviour of aluminum- and magnesium-doped spherical lithium nickel cobalt mixed oxides Li1−x (Ni1−y−zCoyMz)O2 (M = Al, Mg). J. Power Sources, **2003**, 119, 178–83
91. Yazami, R., Touzain, P., A reversible graphite-lithium negative electrode for electrochemical generators. J. Power Sources, **1983**, 9, 365–37
92. Ferg, E., Gummow, R.J., Dekock, A., and Thackeray, M.M., Spinel anodes for lithium-ion batteries J Electrochem Soc, **1994**, 141, L147–L150
93. Koontz, D.E., Feder, D.O., Babusci, L.D., and Luer, H.J., Lead-acid battery: reserve batteries for bell system use; design of the new cell Bell System Technical J., **1970**, 49, 1253–1278
94. Huang, B., Pan, Z., Su, X., and An, L., Recycling of lithium-ion batteries: recent advances and perspectives. J Power Sources, **2018**, 399, 274–286
95. Jamesh M.-I., Recent advances on flexible electrodes for Na-ion batteries and Li-S batteries J Energy Chem, **2019**, 32, 15–44
96. Ghimire, P.C., Bhattarai, A., Schweiss, R. Scherer, G.G., Wai N., and Yan, Q., A comprehensive study of electrode compression effects in all vanadium redox flow batteries, including locally resolved measurements Appl Energy, **2018**, 230, 974–982
97. Baumann, L., and Boggasch, E., Experimental assessment of hydrogen systems and vanadium-redox-flow batteries for increasing the self-consumption of photovoltaic energy in buildings. Int J Hydrogen Energy, **2016**, 41, 740–751
98. Keshan, H., Thornburg, J., Ustun, T.S., Comparison of lead-acid and lithium-ion batteries for stationary storage in off-grid energy systems. Conference: 4th IET Clean Energy and Technology Conference (CEAT 2016) **2016**, 1-7
99. Theodore, A. M., Abdullahi, A.A., Pawan, S. D., Effect of Layered, Spinel, and Olivine-Based Positive Electrode Materials on Rechargeable Lithium-Ion Batteries: A Review. JCMPS, **2023**, 6, 38-57
100. Wang, F., Robert, R., Chernova, N.A., Omenya, F., Badway, F., Hua, X., Ruotolo, M., Zhang, R., Wu, L., Volkov, V., Su, D., Key, B., Whittingham, M.S., Grey, C.P. Amatucci, G.G., Zhu, Y., and Graetz, J., Conversion reaction mechanisms in lithium-ion batteries: study of the binary metal fluoride electrodes. J Am Chem Soc, **2011**, 133, 18828–36
101. Danis, L., Gateman, S.M., Kuss, C., Schougaard, S.B., Mauzeroll, J., Nanoscale measurements of Lithium-ion-battery materials using scanning probe techniques, ChemElectroChem, **2017**, 4, 6–19
102. Tennyson, E.M., Gong, C., Leite, M.S., Imaging energy harvesting and storage systems at the Nanoscale, ACS Energy Lett, **2017**, 2, 2761–2777
103. Huang, S.Q., Wang, S.W., Jin, Y. Wang, D., Shen, C., Application of Atomic Force Microscopy for the study of lithium-ion batteries. J. NanoScience, NanoEngineering Appl., **2015**, 5, 35–47
104. Eyercioglu, O., Gov, K., and Aksoy, A., Validation of material model and mechanism of material removal in abrasive flow machining, The International Journal of Materials and Engineering Technology (TIJMET), **2023**, 6(1):7-11
105. Liu, X., Wang, D., Wan, L., Progress of electrode/electrolyte interfacial investigation of Li-ion batteries via in situ scanning probe microscopy, Sci. Bulletin, **2015**, 60, 839–849
106. Zhiqiang, Z., Yuxin, T., Zhisheng, L., Jiaqi, W., Yanyan, Z., Renheng, W., Wei, Z., Huarong, X., Mingzheng, G., Xiaodong, C., Fluoroethylene Carbonate enabling a robust LiF-rich solid electrolyte interphase to enhance the stability of the MoS2 Anode for Lithium-ion storage, Angewandte Chemie International Edition, **2018**, 57, 3656–3660
107. Lu, W., Xiao, J., Wong, L.-M., Wang, S., Zeng, K., Probing the ionic and electrochemical phenomena during resistive switching of NiO Thin Films, ACS Appl. Mater. Interfaces, **2018**, 10, 8092–8101
108. Zhu, K., Luo, Y., Zhao, F., Hou, J., Wang, X., Ma, H., Wu, H., Zhang, Y., Jiang, K., Fan, S., Wang, J., Liu, K., Free-standing, binder-free Titania/super-aligned carbon nanotube anodes for flexible and fast-charging Li-ion batteries. ACS Sustainable Chem. Eng., **2018**, 6, 3426–3433
109. Aktürk, A., Seda Türk, S., Comparıson of An Interval Type-2 Fuzzy Sets and AHP Methods For Materıal Selectıon Problem on Lithium-Ion Batterıes, The International Journal of Materials and Engineering Technology (TIJMET), **2020**, 3(1):30-46

The International Journal of Materials and Engineering Technology (TIJMET) (2023) 6(2)
http://dergipark.gov.tr/tijmet
ISSN: 2667-4033

RESEARCH ARTICLE

Effect of carbon fiber additive on tensile properties of large scale additive manufactured (LSAM) ABS single wall parts

Omer Eyercioglu[1], Engin Tek[2], Mehmet Ali Akeloglu[1] and Mehmet Aladag[3]

[1]*Gaziantep University, Engineering Faculty, Mechanical Engineering Department, Gaziantep, Türkiye*
[2]*Istanbul Gedik University, Gedik Vocational School, Mechatronics Department, Istanbul, Türkiye*
[3]*Bialystok University of Technology, Faculty of Mechanical Engineering, Mechanical Department, Bialystok, Poland*

Article Info

Article history:
Received 07.12.2023
Revised: 27.12.2023
Accepted: 31.12.2023
Published Online: 31.12.2023

Keywords:
Additive manufacturing
Large scale additive manufacturing (LSAM)
ABS
Carbon fiber
Tensile strength

Abstract

Additive Manufacturing (AM) is one of the most studied technologies to produce different parts today. Large-scale additive manufacturing (LSAM) is used to produce complex parts without further technological processes and for the production of large-sized polymer parts. In order for the parts produced from polymer materials to show better mechanical properties, a range of different materials is required. In this study, the tensile properties of 3D-printed ABS single-wall parts using LSAM were investigated experimentally. The effect of carbon fiber (0, 5%, and 10%) additive on the main mechanical properties of ABS was investigated. The tests were carried out according to ASTM D638 standards as the spatial printing direction (0º and 90º). According to the results of the tensile test, ABS material reinforced with 5% carbon fiber showed higher load resistance than other mixture ratios. In all groups, it was observed that the samples with a horizontal (0º) orientation compared to the printing direction showed better performance.

1. Introduction

The technology of printing objects layer by layer through additive manufacturing (AM) has increased tremendously in recent decades [1,2]. Combining computer-aided design (CAD) and computer-aided manufacturing (CAM) technologies, 3D printing technology produces parts without requiring any traditional cutting techniques, and the raw material waste that occurs in this process is very low. Considering these advantages, AM technology is always used to produce complex structures and thin-walled structures [3,4]. Nowadays, 3D printing technology is widely applied in manufacturing, civil engineering, automotive engineering, biomedical engineering, food, and clothing [5,6].

Fused Deposition Modeling (FDM) is one of the most popular AM technologies in the production of polymer and composite components. FDM requires a 3D model in stereolithography (STL) format to print a part [7]. After the model is created, it is made into layers with slicing software. During the printing process, the raw material filament is injected into a pre-heated nozzle, making it semi-liquid, and laid out layer by layer along a predetermined path, creating the final part. Although FDM has advantages over traditional methods, it has some limitations. These are limited printing areas, printing speeds, and raw material limitations. Large-scale additive manufacturing (LSAM) fills the gap created by these disadvantages [8].

Compared to traditional FDM printers, LSAM provides a wide range of usage opportunities in terms of printing speed, printing area, and raw material. LSAM uses a direct extruder system and uses granules as raw materials, thus offering a wide variety of raw materials [9]. LSAM can achieve print speeds of up to 50 kg/h. Thus, it is capable of printing large-scale parts quickly and easily [10].

A shortcoming of the LSAM wide range of materials is that for a new material class, the mechanical properties are still unclear. Therefore, real LSAM 3D printing structures cannot be accurately modeled and analyzed, and the use of new materials is difficult. Due to this lack of information, studies on the material have increased recently [11,12].

In research conducted in this context, Lee et al. [13] investigated the effects of several process variables on the compressive strength of 3D printed components, including raster direction, air spacing, bead size, color, and the thermal condition of the model. Their findings demonstrated that these components' compressive characteristics are anisotropic. In a different work, Weng et al. [14] found that adding organically modified montmorillonite to ABS nanocomposites improved both tensile strength and flexural resilience when the materials were 3D printed. In their analysis of the mechanical properties of FDM-produced ABS materials, Rodriguez et al. [15] found that the strength decreased between 22% and 57% while switching from ABS monofilament to FDM ABS components. Roschli et al. examined large-area additive manufacturing systems, focusing on enhancing inter-laminar strength and process regulation. They also investigated the impact of adding carbon fiber to ABS on its tensile strength [9].

The materials used in production with additive manufacturing are relatively limited. In order to improve the physical and mechanical properties of materials, composite additive manufacturing parts have been produced by using different materials in different compositions and it is aimed to improve the mechanical and physical properties. Kartal et al. [16] have investigated the Salvadora Persica (Miswak) additives effect on reinforced polylactic acid (PLA) matrix composites' mechanical performance. This study investigates the use of natural fibers as reinforcement for composites that are 3D

Corresponding Author: Engin Tek
E-mail: engin.tek@gedik.edu.tr

How to cite this article:
Eyercioglu O., Tek E., Akeloglu M.A., Aladag M., Effect of Carbon Fiber Additive on Tensile Properties of Large Scale Additive Manufactured (LSAM) Abs Single Wall Parts, The International Journal of Materials and Engineering Technology (TIJMET), 2023, 6(2): 79-82

printed, providing information about substitute materials that may be contrasted with other additives. Moreover, the effect of production parameters on the mechanical properties of the final product in the additive manufacturing process has been found to be undeniably important. Another study by Kartal et al. [17] showed how crucial manufacturing parameters are to achieving the required mechanical properties in 3D-printed parts. This study also provided valuable insights into how nozzle diameter affects tensile strength and could offer a comparative viewpoint on how various manufacturing parameters impact the characteristics of materials. In addition, Kaptan et al. [18] are examined how various fill rates affect the mechanical characteristics of PLA samples made with 3D printers, this research provides a wider framework for comprehending how different printing parameters affect the final result by examining fill rate, another important component of 3D printing, and its effect on mechanical properties.

In this study, the mechanical properties of a new material mixture for use in LSAM were examined. A single-skinned wall was produced by adding different amounts of carbon fiber to the ABS material (0%, 5%, and 10%). It was produced by cutting samples horizontally and vertically according to the printing direction in accordance with ASTM 650 standards from the single-walled wall. In the samples taken, it was seen that 5% carbon fiber-reinforced ABS material was the most usable. Compared to the printing direction, horizontal (0^0) samples gave better results.

2. Materials and methods

2.1 Materials

A thermoplastic polymer called ABS (Acrylonitrile Butadiene Styrene) was employed in the experimental work, and Table 1 lists the ABS's characteristics. The ABS granules were dried at 80 ºC for four hours before to use. On a heated construction plate that is heated to 80 ºC, the melted material is deposited at 240 ºC.

In this work, an ABS polymer-based multilayer wall was created using varied quantities of carbon fiber additive, and form variations of these samples were noted with carbon fiber additive ratio. The carbon fiber was 7 µm in diameter and 1±0.3 mm in length.

Table 1. The mechanical properties of ABS.

Properties	Unit	Value
Density	kg/m3	1060
Thermal Conductivity	K (W/mK)	0.177
Specific Heat	C (J/KgK)	2080
Emissivity	ε	0.87
Glass Transition Temperature	Tg (ºC)	105
Thermal Contraction Coefficient	$°C^{-1}$	0.0001

2.2 Printing System

LSAM is a printer that uses the direct extrusion system. Figure 1. The direct extrusion system has been replaced by a 3D CNC spindle. The technical specifications of the LSAM are given in Table 1. The single-screw extruder is powered by a motor with a variable speed. An automated feeder feeds ABS granules through the extruder. To melt and deposit molten polymer at a rate commensurate with the movement of the axis (building speed) and desired bead profile, the rate of granule feed and the speed of the screw may be regulated. To maintain the chamber and nozzle temperatures within the specified limits, the barrel is equipped with band heaters and a control device.

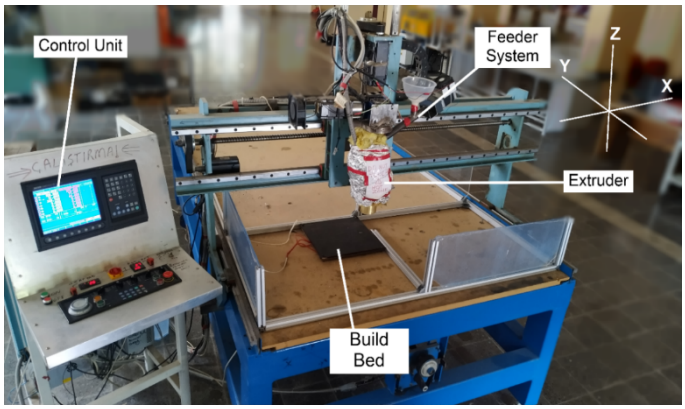

Figure 1. View of Large Scale Additive Manufacturing System.

Table 2. Parameters of LSAM

Parameter	Unit	Value
X-Axis	mm	1800
Y-Axis	mm	2500
Z-Axis	mm	400
Nozzle Diameter	mm	6
Deposition Temperature	oC	240
Layer Height	mm	6
Printing Speed	mm/min	400

2.3 Experimental Study

In the experimental investigation, single-walled structures were produced in LSAM utilizing ABS thermoplastic material, augmented with incremental concentrations of carbon fiber additives by weight (0%, 5%, and 10%). To ensure these structures adhered to the specified dimensional parameters, a milling procedure was executed via a CNC milling machine in figure 2. Regarding the tensile testing, specimens were prepared in accordance with the ASTM D638 standards. They were produced using a router, oriented both in a parallel (0 degrees) and perpendicular (90 degrees) manner relative to the printing direction, as delineated in Figure 3.

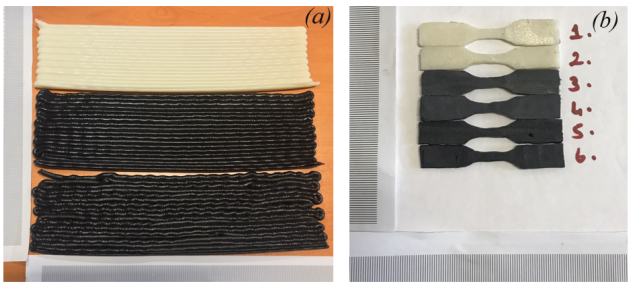

Figure 2. The tensile test samples a) before and b) after the CNC milling machine process

The SCHIMATZU AGS-X 30KN apparatus was employed for the tensile testing. Prior to the test, the setup was configured in compliance with ASTM D638 standards. The specimen's dimensions are given in Figure 3. In the course of the

experimental investigation, five samples from each group were prepared and subjected to testing. Following the tensile test, distinct load and displacement graphs were generated for each sample using auxiliary software provided by the device.

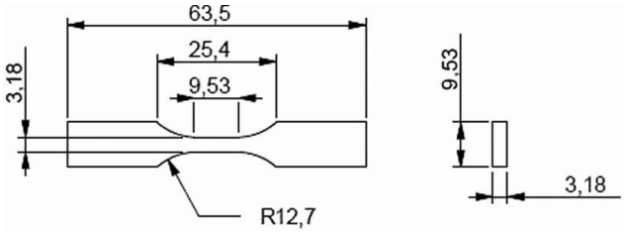

Figure 3. Dimension of tensile specimens

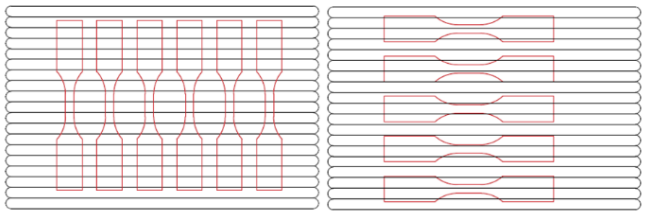

Figure 4. Orientation of tensile specimens

3. Results and discussion

In this section, tensile test results of samples produced from single-walls are given. First of all, the image of a sample during the test is given in Figure 5. Experimental results are given in two graphs for the printing direction horizontally (0º) and vertically (90°).

In the first graph, stress and strain results are given from samples prepared horizontally (0) to the printing direction. As seen in Figure 6, ABS reinforced with 5% carbon fiber gave the highest load resistance. Pure ABS material showed ductile behavior by providing the highest elongation. 10% carbon Fiber reinforced ABS has been found to be brittle and has less load resistance than others.

In the second graph, the experimental results of samples prepared perpendicular to the printing direction are given. Figure 7. Similar result curves were observed as in the previous graph. However, there is not as much difference between ABS reinforced with 5% carbon fiber and pure ABS material as in other graphics.

Figure 5. During tensile test

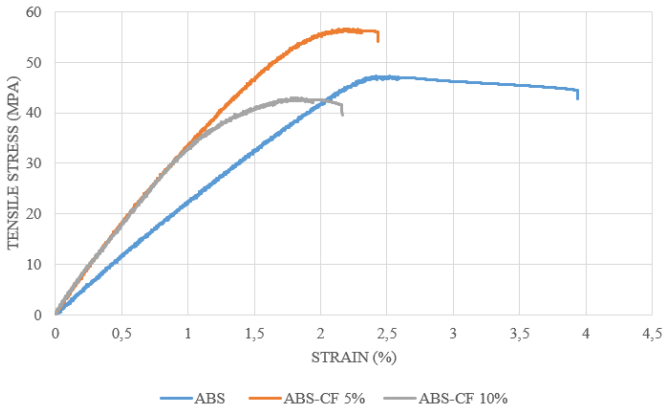

Figure 6. Tensile test result; horizontal (0º) in the printing direction

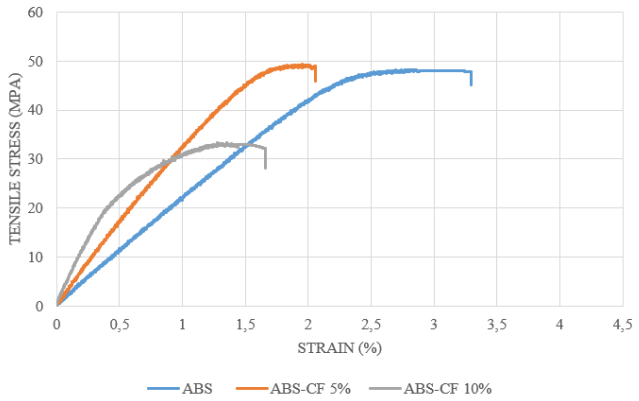

Figure 7. Tensile test result; horizontal (90º) in the printing direction

4. Conclusions

In this study, tensile tests were carried out to see the effects of carbon fiber additives on the mechanical behavior of ABS composites. Using the direct extrusion LSAM system, 5 samples were produced for each sample group from a single wall. Each sample group has a different amount of carbon fiber. The samples were subjected to tensile testing according to the ASTM D638 standard. It is possible to draw the following conclusions from the results of the research:

- With the addition of increasing amounts of carbon fiber, the ductility of the extruded cord decreases. Pure ABS has maximum ductility.
- Among all samples containing various amounts (0%–10%) of carbon fiber, the maximum tensile stress was obtained for the 5% carbon fiber-reinforced sample.
- Samples that were horizontal (0º) in the printing direction gave better results than samples that were vertical (90º) in the printing direction. Anisotropy is a common problem in additive manufacturing due to bonding characteristics of the layers.

Author contributions

Omer Eyercioglu: Supervision, review & editing.

Engin Tek: Preparing samples, Testing, Writing - original draft

Mehmet Ali Akeloglu: Preparing samples, Testing, Writing - original draft

Mehmet Aladag: Writing - original draft

References

1. Zhao, Y., Chen, Y., and Zhou, Y., Novel mechanical models of tensile strength and elastic property of FDM AM PLA materials: Experimental and theoretical analyses. Materials and Design, **2019**, 181, 108089
2. Wang, X., Zhao, L., Fuh, J.Y.H., and Lee, H.P., Effect of porosity on mechanical properties of 3D printed polymers: Experiments and micromechanical modeling based on X-ray computed tomography analysis. Polymers, **2019**, 11:(7)
3. Rodríguez-Panes, A., Claver, J., and Camacho, A.M., The influence of manufacturing parameters on the mechanical behaviour of PLA and ABS pieces manufactured by FDM: A comparative analysis. Materials, **2018**, 11(8)
4. Sehhat, M.H., Mahdianikhotbesara, A., and Yadegari, F., Verification of stress transformation in anisotropic material additively manufactured by fused deposition modeling (FDM). International Journal of Advanced Manufacturing Technology, **2022**, 123(5–6):1777–1783
5. Movahedi, N., and Linul, E., Quasi-static compressive behavior of the ex-situ aluminum-alloy foam-filled tubes under elevated temperature conditions. Materials Letters, **2017**, 206, 182–184
6. Rajak, D.K., Pagar, D.D., Menezes, P.L., and Linul, E., Fiber-reinforced polymer composites: Manufacturing, properties, and applications. Polymers, **2019**, 11(10)
7. Bhalodi, D., Zalavadiya, K., and Gurrala, P.K., Influence of temperature on polymer parts manufactured by fused deposition modeling process. Journal of the Brazilian Society of Mechanical Sciences and Engineering, **2019**, 41 (3):1–11
8. Kurfess, R., A thermally-driven design methodology for large-scale polymer additive manufacturing systems. **2017**
9. Roschli, A., Duty, C., Lindahl, J., Post, B.K., Chesser, P.C., Love, L.J., and Gaul, K.T., Increasing interlaminar strength in large scale additive manufacturing. Solid Freeform Fabrication 2018: Proceedings of the 29th Annual International Solid Freeform Fabrication Symposium - An Additive Manufacturing Conference, SFF 2018, **2020**, 543–555.
10. Eyercioğlu, Ö., Aladağ, M., and Sever, S. Temperature Evaluation and Bonding Quality of Large Scale Additive Manufacturing Thin Wall Parts. Sigma J Eng & Nat Sci, **2018**, 36(3):645–654
11. Eyercioğlu, Ö., Tek, E., aladağ, M., and Taş, G., Effect of different amounts of carbon fiber additive ABS on thermal distortion and cooling time. The International Journal of Materials and Engineering Technology, **2022**, 5(1):13–17
12. Eyercioglu, O., Tek, E., Aladag, M., and Tas, G., 4-Effect of Different Amounts of Carbon Fiber Additive Abs on Thermal Distortion and Cooling Time., **2022**, 5, 13–17
13. Lee, C.S., Kim, S.G., Kim, H.J., and Ahn, S.-H., Measurement of anisotropic compressive strength of rapid prototyping parts. Journal of materials processing technology, **2007**, 187, 627–630
14. Weng, Z., Wang, J., Senthil, T., and Wu, L., Mechanical and thermal properties of ABS/montmorillonite nanocomposites for fused deposition modeling 3D printing, Materials & Design, **2016**, 102, 276–283
15. Thomas, J.P., and Renaud, J.E., Mechanical behavior of acrylonitrile butadiene styrene (ABS) fused deposition materials, Experimental investigation Âguez, **2006**, 7(3):148–158
16. Kartal, F., Kaptan A., Mechanical performance of salvadora persical (Miswak) reinforced polylactic acid matrix composites for three-dimensional printing, BSJ Eng Sci, **2023**, 6(4):458-468
17. Kartal, F., Kaptan, A., Investigating the effect of nozzle diameter on tensile strength in 3D-printed polylactic acid parts, BSJ Eng Sci., **2023**, 6(3):276- 282
18. Kaptan, A., Kartal, F., The effect of fill rate on mechanical properties of PLA printed samples, Igdır University Journal of the Institute of Science and Technology, **2020**, 10(3): 1919-1927